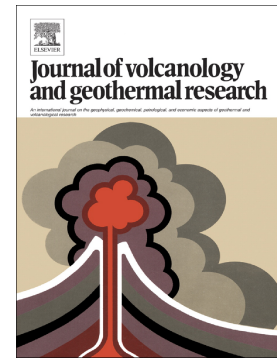


Journal Pre-proof

Sintering dynamics of fine-grained rhyolitic obsidian particles from Hrafninnuhryggur (Krafla, Iceland) with implications for silicic volcanic eruptions

Annabelle Foster, Fabian B. Wadsworth, Jérémie Vasseur, Madeleine C.S. Humphreys, Hugh Tuffen, Donald B. Dingwell, Katherine J. Dobson



PII: S0377-0273(25)00066-6

DOI: <https://doi.org/10.1016/j.jvolgeores.2025.108330>

Reference: VOLGEO 108330

To appear in: *Journal of Volcanology and Geothermal Research*

Received date: 26 July 2024

Revised date: 28 March 2025

Accepted date: 31 March 2025

Please cite this article as: A. Foster, F.B. Wadsworth, J. Vasseur, et al., Sintering dynamics of fine-grained rhyolitic obsidian particles from Hrafninnuhryggur (Krafla, Iceland) with implications for silicic volcanic eruptions, *Journal of Volcanology and Geothermal Research* (2024), <https://doi.org/10.1016/j.jvolgeores.2025.108330>

This is a PDF file of an article that has undergone enhancements after acceptance, such as the addition of a cover page and metadata, and formatting for readability, but it is not yet the definitive version of record. This version will undergo additional copyediting, typesetting and review before it is published in its final form, but we are providing this version to give early visibility of the article. Please note that, during the production process, errors may be discovered which could affect the content, and all legal disclaimers that apply to the journal pertain.

Sintering dynamics of fine-grained rhyolitic obsidian particles from Hrafninnuhryggur (Krafla, Iceland) with implications for silicic volcanic eruptions

Annabelle Foster¹, Fabian B. Wadsworth¹, Jérémie Vasseur², Madeleine C. S. Humphreys¹, Hugh Tuffen³, Donald B. Dingwell², Katherine J. Dobson⁴

¹Earth Science, Durham University, Science Labs, Durham, DL1 3LE, U.K.

²Department of Earth and Environmental Sciences, Ludwig-Maximilians-Universität, 80333, Munich, Germany

³Lancaster Environment Centre, Lancaster University, Lancaster, LA1 4YQ, U.K.

⁴Department of Civil and Environmental Engineering, University of Strathclyde, Glasgow, G1 1XQ, U.K.

Annabelle Foster	0000-0002-1578-5328
Fabian B. Wadsworth	0000-0002-5341-208X
Jérémie Vasseur	0000-0002-0783-5065
Madeleine C. S. Humphreys	0000-0001-9343-1237
Hugh Tuffen	0000-0001-8829-1751
Donald B. Dingwell	0000-0002-3332-789X
Katherine J Dobson	0000-0003-2272-626X

Correspondence to: fabian.wadsworth@gmail.com

Abstract

Sintering – or welding – is a key process in volcanic eruptions and controls the formation of welded ignimbrites, obsidian pyroclasts in volcanic conduits, and possibly also silicic lavas. Here, we study the sintering behaviour of packs of fine-grained particles of rhyolitic obsidian subjected to different temperature pathways at atmospheric pressure, with a focus on the evolution of the total porosity of the sintering pack and material microtexture. We collect high-resolution continuous *in situ* data for obsidian sintering and compare our results with the ‘vented bubble model’ – a versatile model for viscous sintering kinetics. This model accounts for syn-sintering degassing and outgassing of dissolved H₂O, which affects the particle viscosity. We also account for polydisperse particle size distributions, and arbitrary thermal history – i.e. any heating or cooling pathway and/or isothermal conditions. We find that the model performs well for fine particles sieved to $\lesssim 63 \mu\text{m}$. For particles $> 63 \mu\text{m}$, sintering changes rate compared with the model and finally occurs more slowly than the model prediction. We explore this deviation by defining a capillary Peclet number P_c which balances the rates of diffusive loss of H₂O from the particles with rates of sintering; particles that are relatively large compared with the diffusive lengthscale (here $> 63 \mu\text{m}$) have large $P_c \gtrsim 10$ and therefore it is likely that deviations from the model are associated with substantial intra-clast gradients in H₂O, which translate to viscosity gradients. However, the efficacy of the model for relatively small particles and across a range of conditions demonstrates its general applicability to natural scenarios in which relatively small obsidian particles ($\leq 63 \mu\text{m}$) are deposited hot, and weld together to form variably dense deposits. After model validation, we apply this model to the case of sintering at Hrafninnuhryggur (Krafla, Iceland) where a ridge of obsidian is interpreted to have formed through sintering of fine hot particles during a rhyolitic fissure eruption. In this application, we discuss the effects of intra-grain vesiculation and nanolite crystal precipitation, and what role those additional process would play in sintering. Using these results, we propose a sintering timescale map for obsidian sintering at rhyolite volcanoes, which will be useful for understanding silicic volcanic eruptions.

Keywords

volcanic welding; explosive-effusive transition; rhyolite; cryptic fragmentation; tuffsite

Journal Pre-proof

Nomenclature Parameter*	Symbolic notation	Units (S.I.)
Gravitational acceleration	g	$\text{m} \cdot \text{s}^{-2}$
Particle radius	R	m
1 st moment of the particle size distribution (mean)	$\langle R \rangle$	m
2 nd moment of the particle size distribution (variance)	$\langle R^2 \rangle$	m^2
3 rd moment of the particle size distribution (skewness)	$\langle R^3 \rangle$	m^3
Critical sample radius when $P_c = 1$	$\langle R \rangle_c$	m
Sample mass	m_i	kg
Sample height	h	m
Sample width	W	m
Sample 2D cross sectional area	$A = hW$	m^2
Initial sample area; final sample area	$A_i; A_f$	m^2
Sample volume	V	m^3
Initial sample volume; final sample volume	$V_i; V_f$	m^3
Sample density	ρ	$\text{kg} \cdot \text{m}^{-3}$
Particle density; glass density	$\rho_p; \rho_g$	$\text{kg} \cdot \text{m}^{-3}$
Particle viscosity	μ	$\text{kg} \cdot \text{m}^{-1} \cdot \text{s}^{-1}$
Average viscosity in the particle	$\langle \mu \rangle$	$\text{kg} \cdot \text{m}^{-1} \cdot \text{s}^{-1}$
Particle viscosity at equilibrium H ₂ O	μ_e	$\text{kg} \cdot \text{m}^{-1} \cdot \text{s}^{-1}$
Surface tension	Γ	$\text{kg} \cdot \text{s}^{-2}$
Confining pressure	P	$\text{kg} \cdot \text{m}^{-1} \cdot \text{s}^{-2}$
Gas pressure	P_g	$\text{kg} \cdot \text{m}^{-1} \cdot \text{s}^{-2}$
Effective pressure	$P_e = P - P_g$	$\text{kg} \cdot \text{m}^{-1} \cdot \text{s}^{-2}$
Laplace pressure	$P_L = 2\Gamma/R$	$\text{kg} \cdot \text{m}^{-1} \cdot \text{s}^{-2}$
Partial pressure of H ₂ O	$P_{\text{H}_2\text{O}}$	$\text{kg} \cdot \text{m}^{-1} \cdot \text{s}^{-2}$
Mol. fraction of H ₂ O in laboratory air	α	
Shear stress (acting on a sintering pack)	σ	$\text{kg} \cdot \text{m}^{-1} \cdot \text{s}^{-2}$
Diffusivity of H ₂ O in rhyolite	D	$\text{m}^2 \cdot \text{s}^{-1}$
Diffusivity of H ₂ O in rhyolite at equilibrium H ₂ O	D_e	$\text{m}^2 \cdot \text{s}^{-1}$
Liquid shell radius	β	m
Initial bubble radius	a_i	m
Time	t	s
Sintering timescale	$\lambda = \mu a_i / \Gamma$	s
Diffusion timescale	$\lambda_d = R^2 / D$	s
Solubility of H ₂ O in rhyolite	w_e	wt. \%
H ₂ O concentration in the sintering particles	w	wt. \%
Temperature	T	K
Porosity of a sintering pack of particles	ϕ	
Initial porosity; final porosity	$\phi_i; \phi_f$	
Crystallinity (non-porous volume)	ϕ_x	
Maximum packing of crystals in melt	ϕ_m	
Crystal-bearing magma viscosity	$\mu_x = \mu(1 - \phi_x / \phi_m)^{-2}$	
Dimensionless groups/parameters		
Eötvös number	$\text{Eo} = \rho_p R^2 g / \Gamma$	
Ohnesorge number	$\text{Oh} = \mu(\Gamma \rho_p R)^{-1/2}$	
Dimensionless pressure	$\bar{P} = P_e P_L$	
Polydispersivity parameter	$S = \langle R \rangle \langle R^2 \rangle / \langle R^3 \rangle$	
Normalized porosity	$\bar{\phi} = \phi / \phi_i$	

Capillary Peclet number
Dimensionless time

$$Pc = \Gamma R^2 / (a_i \mu D)$$

$$\bar{t} = t / \lambda$$

*Empirical constants in Eqs 4, 6, and 7, are not given here.

1. Introduction

Explosive eruptions are characterized by magmatic fragmentation during magma ascent – a process by which ascending magma breaks into fragments, or pyroclasts, including volcanic ash and pumice. As a consequence of its high relative viscosity, silicic magma is especially prone to fragmentation as it ascends through volcanic plumbing system in the crust. The pyroclasts that are formed at fragmentation are accelerated to high velocity ($\sim 100 \text{ m.s}^{-1}$) up the conduit toward the Earth's surface (Mastin, 2002; Degruyter et al., 2012; Gonnermann, 2015; Arzilli et al., 2019; Scheu and Dingwell, 2022). The pyroclastic products of fragmentation can remain hot (relative to the solidus or glass transition) during transport up the volcanic conduit and into the lower volcanic plume or pyroclastic jet (Mastin and Ghiorso, 2001). If the pyroclastic products remain hot on deposition, they can stick, coalesce and weld/sinter together (Branney et al., 1992; Sparks et al., 1999; Wadsworth et al., 2022c). Hot deposition and welding can produce deposits such as (1) welded ignimbrites on the surface of the Earth (Sparks et al., 1973, 1999; Branney et al., 1992; Streck and Grunder, 1995; Grunder et al., 2005; Andrews and Branney, 2011; Lavallée et al., 2015a; Sheikh et al., 2020), (2) obsidian pyroclasts formed on volcanic conduit walls (Gardner et al., 2017, 2019; Monnereau et al., 2021; Wang et al., 2021; Wadsworth et al., 2022a; Ellis et al., 2023), and (3) tuffisites in lava or country rock (Heiken et al., 1988; Stasiuk et al., 1996; Tuffen et al., 2003; Tuffen and Dingwell, 2005; Castro et al., 2012; Kolzenburg et al., 2012; Kendrick et al., 2016; Heap et al., 2019; Unwin et al., 2021, 2023). Cassidy et al. (2018) showed that silicic eruptions are typically characterised by an initial phase of explosive fragmentation. This is then often followed by a second phase of in-conduit capture and sinter-assembly of pyroclasts to form conduit-lining deposits and lava (Gardner et al., 2018, 2019; Wadsworth et al., 2020, 2022a; Farquharson et al., 2022; Trafton and Giachetti, 2022). This is termed the 'cryptic fragmentation' model, which has been invoked to explain simultaneous explosive-effusive eruption behaviour, controlled by ash pyroclast sintering dynamics.

Video footage from Volcán Chaitén (2008-2009) and Cordón Caulle (2011-2012), show hybrid, explosive and effusive behaviour, where intermittent jets of gas and pyroclasts erupt through fractures during sustained lava effusion (Pallister et al., 2013; Schipper et al., 2013; Castro et al., 2014; Wadsworth and Tuffen, 2016; Heap et al., 2019; Wadsworth et al., 2022a). Field observations of these fractures show that many fracture surfaces are coated with oxidized, fine-grained ash, and occasional adhered and sintered larger clasts (Farquharson et al., 2022; Wadsworth et al., 2022a). Additionally, ejected bombs during the hybrid explosive-effusive activity at Cordón Caulle are polymict, containing a heterogenous componentry, i.e., bombs constructed of variably sintered ash, pumice, obsidian, and lithics, thought to capture the complexity of the shallow conduit (Schipper et al., 2021; Wadsworth et al., 2022a; Tuffen et al., 2022; Unwin et al., 2023).

The conception that the shallow conduit is dominated by a polymict sintered rubble is supported by direct field observations from a dissected silicic volcanic vent at Mule Creek (New Mexico, U.S.A.), which shows that similarly complex material comprising mixtures of pumice, lithics, obsidian, and volcanic ash, are sintered to the walls of the exposed conduit. This site additionally reveals that deposition of sintering pyroclasts in the conduit center occurred later than at the margins, evidenced by cross-cutting tuffisites that propagate out laterally from the conduit into the country rock. These are more common in the marginal deposits than in the central deposits (Stasiuk et al., 1996; Unwin et al., 2023). The lateral stratigraphy indicates that the deposits formed through progressive aggradation and sintering from the conduit walls towards the conduit center. Progressive accretion and sintering of

pyroclasts can eventually clog the conduit and decrease the permeability of the deposits, which in turn limits continued outgassing (Heap et al., 2019; Unwin et al., 2023) and may promote overpressure in the conduit. Overpressure could lead to an increase in explosive potential and possibly a return to explosive eruption (Quane et al., 2009; Farquharson et al., 2017; Kolzenburg et al., 2019), tuffisite formation, or potentially the effusion of the sintered deposits as short-range lava (Wadsworth et al., 2020; Trafton and Giachetti, 2022; Unwin et al., 2023; Foster et al., 2024). Therefore, sintering may be a central process in determining silicic eruption behaviour as well as facilitating hybrid activity.

However, our understanding of sintering dynamics in the context of volcanic eruptions is still in its infancy. This is principally because (1) pyroclastic deposits vary widely in their componentry (Quane and Russell, 2006); (2) the grain size distributions from volcanic eruptions can be very broad and these are a first order control on sintering rates (Wadsworth et al., 2019, 2022c); (3) degassing that occurs during transport, deposition, or sintering can lead to heterogeneous volatile concentrations as well as vesiculation within clasts (Wadsworth et al., 2019, 2021; Weaver et al., 2022, 2023); (4) clasts may have variable temperatures and crystallinities, affecting sintering rates directly through the effects on viscosity and surface tension (Kendrick et al., 2016; Wadsworth et al., 2022c; Blandon et al., 2023); and (5) because sintering can be so complete that any textural evidence for the process can be overprinted (Branney et al., 1992; Branney and Kokelaar, 2002; Tuffen and Dingwell, 2005; Giachetti et al., 2021). In the context of the cryptic fragmentation model, this last point effectively erases the evidence for the fragmentation process and any sign that lava was once in a granular state. Here, we aim to address some of these complexities with a focus on the effects of grain size of the sintering particles. To date, sintering experiments have been performed with relatively fine particles that have a mean size $\sim 10 \mu\text{m}$ (Wadsworth et al., 2019). However, we know that hydrous pyroclasts can have more complex behaviours when they are millimetric (Weaver et al., 2022, 2023). To bridge this gap, we aim to perform experiments at a range of particle sizes. In addition, we vary the temperature history of the sintering samples, in order to further test a theoretical sintering model. We use our results, together with natural observations from an exposed silicic conduit (Hrafnatinnuhryggur, Iceland; Tuffen & Castro 2009; Foster et al. 2024), to improve understanding of the eruption dynamics in shallow systems, hybrid eruptive behaviour, and obsidian lava formation.

2. Background

a. Motivating observations from Hrafnatinnuhryggur

We focus our application on Hrafnatinnuhryggur (Krafla, Iceland) because it features an exposed silicic feeder dyke in stratigraphic continuity with lava-like deposits (Tuffen and Castro, 2009), where direct evidence has established that both the feeder dyke and lavas originated through sintering of rhyolitic pyroclasts (Foster et al. 2024). In the feeder dyke outcrops, evidence for a sintering origin includes (1) the direct observation of a continuous welding transition from loose marginal pumice to dense obsidian in the feeder dyke outcrops; (2) cusped relict clast boundaries in thin section in the feeder dyke deposits, i.e., cusped vesicles and phantom clast edges marked by faint, white suture lines within obsidian; and (3) the presence of basaltic country rock and crystalline lithics that can be found in the feeder dyke core (Foster et al. 2024). In the associated subaerial lava, evidence for the same sintering origin includes (1) fractures that host small, $\sim 10 \mu\text{m}$ diameter, sub-rounded particles with a droplet-like morphology, that have developed incipiently sintered necks with one another (**Fig. 1**); and (2) closed/healed fractures that host tuffisite deposits, typically containing matrix-supported sub-angular or sub-rounded obsidian clasts in a dense finer-grained matrix. The good preservation of the lava-like deposits provides constraints of the particle sizes and the degree of sintering, which are essential for applying sintering models to their formation.

In addition to the textures in the feeder dyke deposits and the lava deposits (Tuffen & Castro 2009; Foster et al. 2024), the overall morphology of the Hrafnatinnuhryggur deposits suggests an origin through sintering. Geomorphologically, Hrafnatinnuhryggur is a 2.5 km-long NNE-SSW ridge generated in a fissure eruption parallel to the associated dyke swarm (Hjartardóttir et al., 2012). Discrete and discontinuous dense lava-like bodies crop out just off-axis to either side of the ridge

centerline. Between these lava deposits are loose deposits of pumice. The lava-like deposits have been interpreted as representing areas of sintering localization during the waning phase of an explosive eruption (Foster et al. 2024) such that the conduit is envisaged as being heterogeneous – with some areas being coherent, sintered pyroclastic deposits connected to overlying lava-like deposits, while other portions are loose and incipiently or incompletely sintered pumice-dominated deposits. This picture of the shallow architecture is consistent with interpretations made from the volcanic bomb observations at the 2011-12 Cerdón Caulle deposits (Schipper et al., 2021; Wadsworth et al., 2022a) and observed directly and *in situ* at the dissected, 19Ma Mule Creek deposits (Unwin et al., 2023).

Here, we use the observations from Hrafninnuhryggur as motivation for a campaign of experimentation concerning the sintering dynamics of crystal-poor obsidian particles at high temperature. We choose to use dense obsidian particles and not pumice particles for the experiments, in part because where sintered fragments are found in the field, they are dense, although we acknowledge that particles can densify by diffusive outgassing (Yoshimura and Nakamura, 2008; von Aulock et al., 2017; Weaver et al., 2022, 2023), which is discussed later. Our aim is to capture the general features of the transition from granular to densely welded deposits in terms of the textures, as well as the time-evolution of the process. We use the porosity between grains as a metric for the progress of sintering from granular (high porosity) to dense (very low porosity) (Quane and Russell, 2005a) and record progressive changes in porosity as a function of time spent at high temperature. Results will provide new insights into the dynamics and timescales of fundamental, eruption-governing processes.

b. Sintering dynamics in volcanic environments

Viscous sintering is a process where molten, high-viscosity particles coalesce to form a connected liquid body that evolves to a relatively denser, low porosity melt (Frenkel, 1945; Mackenzie and Shuttleworth, 1949; Prado et al., 2001; Kang, 2004; Vasseur et al., 2013; Wadsworth et al., 2014, 2016, 2017b). We note that under certain circumstances, such as when sintering involves a large proportion of crystalline material, a denser final state may not be achieved (Eberstein et al., 2009; Blandon et al., 2023); however, in the melt-dominated sintering we consider here, a denser relative final state is expected. In the study of sintering processes in volcanic settings, the term ‘sintering’ has been used to describe the first ‘incipient’ stage in this overall densification process (Branney et al., 1992), and ‘welding’ has become the primary field term for the later stages of the densification when the porosity is low (Sparks et al., 1999; Quane and Russell, 2005b, 2005a). By contrast, here we use the term ‘sintering’ to refer to the complete process, which is more consistent with materials science literature, and acknowledges that the densification process is a continuum from particle to pores, such that any separation of early and late stages is arbitrary (Prado et al., 2001; Wadsworth et al., 2016).

It is important to understand the dynamics that underpin sintering because it results in significant changes in the physical properties of the deposits. The drop in bulk porosity that is typical of sintering processes has a concomitant effect on other properties of the sintered material: (1) the bulk material strength goes up (Vasseur et al., 2013; Carbillet et al., 2021, 2022; Wadsworth et al., 2022c); (2) the permeability drops to zero (Colombier et al., 2017; Farquharson et al., 2017; Ryan et al., 2020; Eichheimer et al., 2020; Wadsworth et al., 2021, 2022c, 2023); and (3) the elastic properties such as the shear and bulk moduli increase (Coble and Kingery, 1956; Vasseur et al., 2016). These changes can be substantial and dictate the deformation or hydraulic regimes of the deposits after emplacement.

Traditional models of the viscous sintering process deal with relatively simple systems, and therefore do not account for many of the complexities involved in volcanic eruptions (Frenkel, 1945; Mackenzie and Shuttleworth, 1949). Important complexities in volcanic sintering include:

- Non-isothermal conditions. Volcanic material cools upon fragmentation as it travels through and out of the conduit via adiabatic expansion (Mastin and Ghiorso, 2001). Temperatures can also increase through viscous heating (Cordonnier et al., 2012; Lavallée et al., 2015b), granular friction (Lavallée et al., 2014) and by the injection of new magma and crystallization. These processes ultimately control the particle viscosity, which is a key parameter affecting sintering rates.

- Syn-sintering degassing. Fragmented magma is typically supersaturated in volatiles and so will degas and subsequently outgas during transport, emplacement, and any subsequent sintering. Sintering is sensitive to changes in the dissolved H₂O content of the particles because this directly impacts the viscosity of particles (Hess and Dingwell, 1996) and therefore influences the rate at which sintering occurs (Gardner et al., 2019; Wadsworth et al., 2019).
- Polydisperse pyroclast grain sizes. Volcanic pyroclasts formed at fragmentation are inherently polydisperse, where the polydispersity is controlled by how energetic the fragmentation process is (Kueppers et al., 2006) and the pre-existing bubble size distribution and textures.
- Confining pressures and shear. Compaction is a process that controls sintering within ignimbrites, particularly when pressure from the overlying deposit causes H₂O to be resorbed into glass particles, reducing the particle viscosity (Sparks et al., 1999). Further, compaction processes in ignimbrites result in shorter sintering timescales (minutes to hours) relative to low-pressure sintering, so that the effect of cooling is negligible, and that depositional processes have the dominant effect on sintering (Quane et al., 2009).
- Presence of non-juvenile particles. Lithic particles may coexist with juvenile, melt-rich pyroclasts within sintering deposits, and inhibit the melt-mediated sintering process.

These complexities are captured to some extent by existing sintering models (Wadsworth et al., 2019, 2022c; Weaver et al., 2023). Here, we focus on the effects of grain size and grain size distribution, on the understanding that Weaver et al. (2022) used large particles (millimetric) and Wadsworth et al. (2019) used very small particles around 10 μm . In between these two sizes, there has been little work done. Therefore, we explicitly apply a new experimental dataset using natural obsidian from Hrafninnuhryggur, Iceland, in which we vary grain size, grain size distribution, and the temperatures to which samples are exposed. Our goal is to compare these with theoretical models in order to apply the models to natural conditions. A final point of considerable novelty here is to explore the textures that arise in sintering experiments and to compare these with natural textures in the lava-like deposits at Hrafninnuhryggur.

3. An isotropic theoretical model for volcanic sintering dynamics

Viscous sintering involves the amalgamation of deformable particles that are in the droplet/liquid state. For droplets, it is critical to identify the relative importance of forces that may be driving flow/deformation. First, the balance between gravitational and capillary forces is governed by the Eötvös number Eo (sometimes referred to as the bond number) which is $Eo = \rho_p g R^2 / \Gamma$, where ρ_p is the particle density, g is gravity, R is the radius of the droplets and Γ is surface tension. If $Eo \gg 1$, then gravitational forces on the droplet scale dominate, and the droplet can be expected to deform under its own weight. By contrast, if $Eo \ll 1$, capillary forces dominate, and the droplet will not deform under its own weight. A reasonable assumption is that $Eo \approx 1$ represents the boundary between those two regimes. Volcanic ash (i.e. $R \leq 2$ mm) are deposited at $Eo \ll 1$ (Wadsworth et al., 2019). Second, for droplets at $Eo \ll 1$, the balance between viscous and inertial forces is governed by the Ohnesorge number Oh defined as $Oh = \mu(\Gamma\rho_p R)^{-1/2}$ where μ is particle viscosity. Here, $Oh \gg 1$ represents the viscous regime and $Oh \ll 1$ represents the inertial regime. Dominantly because the viscosity is high, volcanic ash/droplets are at $Oh \gg 1$ such that inertia can be neglected (Wadsworth et al., 2019).

Next, we consider the pressure that acts isotropically on the droplets to squeeze them together, potentially decreasing sintering timescales (Sparks et al., 1999) and shear stress that acts to deform particles against one another (Scherer, 1986). In both cases, these parameters are an additional stress that acts to push droplets together and while isotropic pressure and shear stress should strictly be treated differently, here we propose the same scaling for both of these effects on the basis that it is the same regime difference from capillary sintering. During the sintering process there is gas pressure P_g in the pore phase between the particles, which is isotropic. The effective pressure P_e is then $P_e = P - P_g$ where P is the pressure squeezing or pushing the particles together. In detail, P could be

an isotropic squeezing particle pressure $P = P_p$ (e.g. the particle pressure from the weight of a deposit above a given point), or P could be the shear stress shearing particles together $P = \sigma$. P_e can be compared with the capillary pressure P_L exerted by the surface tension $P_L = 2\Gamma/R$. Therefore, a dimensionless pressure scale \bar{P} is $\bar{P} = P_e/P_L = (P - P_g)R/(2\Gamma)$. If $\bar{P} \gg 1$ then the squeezing pressure dominates, so the system is in pressure sintering regime, if $\bar{P} \ll 1$ then it is in the capillary sintering regime. For magmas, it is reasonable to assume P_g is atmospheric during subaerial eruptions, so $P_g = 10^5$ Pa. Even if P_g is high at and above fragmentation in feeder dykes and conduits (Degruyter et al., 2012), there is not likely to be a high squeezing pressure P above that gas pressure value; therefore, $\bar{P} \approx 0$ (Gardner et al., 2018; Wadsworth et al., 2019). Even if clasts are vesiculating and expanding, the lack of any confinement around the sintering particles means that they are able to expand in all directions and therefore are under no external pressure. This implies that pressurization effects and compaction can be neglected (although we discuss this again later in Section 8).

In context of the conduit at Hrafninnuhryggur, we find that $Eo \ll 1$, $Oh \gg 1$, and $\bar{P} \ll 1$, which leads us to conclude that sintering in this case is in the viscous capillary sintering regime. This is the basis of the model summarized below.

a. The vented bubble model

The most versatile sintering model for volcanic applications is the ‘vented bubble model’ (VBM; Wadsworth et al., 2016) because it has been validated against a wide range of data including using natural and synthetic particles and accounts for a range of conditions including arbitrary non-isothermal temperature pathways (Wadsworth et al., 2016, 2019). The VBM translates the convolute and interconnected pore spaces that exist between packed deposited particles, into spherical pores of the same initial radii a_i surrounded by a spherical liquid shell with a radius β (Fig. 2). β is measured from the pore centre and so is a function of time as the bubble expands or shrinks, even when the melt shell volume is constant. The pores are hypothetically connected to the outside of the system of pores by a ‘vent’. We note that this vent is not modelled explicitly, but is a conceptual feature of the model that accounts for the assumption that the pore pressure P_g between the particles remains in equilibrium with the particle pressure P (i.e. $\bar{P} = 0$). The VBM takes the form of a differential equation for the time dependence of the sintering porosity ϕ

$$\frac{d\phi}{dt} = -\frac{3\Gamma}{2\mu a_i} \left(\frac{\phi_i}{1 - \phi_i} \right)^{1/3} \phi^{2/3} (1 - \phi)^{1/3} \quad \text{Eq. 1}$$

where ϕ_i is the initial porosity and t is time. In the context of the VBM, which takes shrinking pores as its starting geometry (such that the bubble radius a_i is the lengthscale of relevance), the sintering timescale can be defined as a capillary timescale $\lambda = \mu a_i / \Gamma$. Therefore, we can define a normalized time $\bar{t} = t / \lambda$. Similarly, we can note that the model is simply scaled by the initial porosity, so that the porosity can be normalized using $\bar{\phi} = \phi / \phi_i$. Injecting these normalizations into Eq. 1 yields a dimensionless model as

$$\frac{d\bar{\phi}}{d\bar{t}} = -\frac{3}{2} \left(\frac{1 - \bar{\phi}\phi_i}{1 - \phi_i} \right)^{1/3} \bar{\phi}^{2/3}. \quad \text{Eq. 2}$$

which is clearly universal for a given ϕ_i . In non-isothermal conditions we take Γ and a_i to be constants during sintering and although they can be affected by temperature, their temperature dependence is negligible compared with the dependence of μ on T , termed $\mu(T)$. The dimensionless sintering time \bar{t} for non-isothermal conditions (Wadsworth et al., 2016, 2017b) is

$$\bar{t} = \frac{t}{\lambda} = \int_{t_i}^t \frac{1}{\lambda} dt = \frac{\Gamma}{a_i} \int_{t_i}^t \frac{1}{\mu(T)} dt \quad \text{Eq. 3}$$

where the integration can be solved numerically using the trapezoidal rule when $\mu(T)$ and $T(t)$ are known. Eq. 2 with Eq. 3 represents a universal sintering model that can be used in a range of conditions and materials when capillary stresses drive sintering. To make this model specific to

rhyolite temperature-dependent viscosity $\mu(T)$ needs to be known. This can be calculated using a model for rhyolites containing a dissolved weight percentage of H₂O (Hess and Dingwell, 1996)

$$\log_{10} \mu(T) = A + \frac{B}{T - C} \quad \text{Eq. 4}$$

where $A = a_1 + a_2 \ln(w)$, $B = b_1 + b_2 \ln(w)$, and $C = c_1 + c_2 \ln(w)$, and $a_1 = -3.545$, $a_2 = 0.833$, $b_1 = 9601$, $b_2 = -2368$, $c_1 = 195.7$, $c_2 = 32.25$, and w is the dissolved H₂O concentration in the melt particles in wt.% and T is in kelvin (after Hess & Dingwell, 1996).

In order to use the VBM, we use built-in ODE solvers in Python™ to find a continuous solution to Eq. 2 with Eqs 3 & 4 for a given $T(t)$ pathway and for specified sample parameters a_i , ϕ_i , and Γ . Details of this numerical method are given in Wadsworth et al., (2016).

b. Particles vs pores and polydisperse distributions of sintering particles

In natural scenarios, viscous particles that sinter together are typically polydisperse (Saubin et al., 2016; Unwin et al., 2023). The vented bubble model is especially well-posed for such polydisperse distributions of particles where a range of particle sizes fill space and make the bubble geometry more realistic (Wadsworth et al., 2017b). Eqs 1-3 take the bubble radius a_i as the relevant lengthscale controlling the sintering rate $d\phi/dt$. However, the notion of a bubble radius in what is initially a pack of angular particles may not be immediately clear (see Fig. 2 for the abstraction step from a pack of particles to a suspension of connected pores in the set-up of the vented bubble model). Wadsworth et al. (2017b) used the statistics of random heterogeneous materials (Torquato, 2013) to find a relationship between the initial particle size distribution $F(R_i)$, where R_i is an initial particle radius, and the initial pore size distribution $F(a_i)$. They used this to find the mean initial pore size $\langle a_i \rangle$ that occurs in the pore interstices of a pack of particles, and proposed that this should be used as the pore size in the vented bubble model – i.e. $\langle a_i \rangle$ replaces a_i in Eqs 1-3. They found that for packs of very polydisperse (i.e. a broad distribution; quantified later) distributions of particles, this conversion from $F(R_i)$ to an output $\langle a_i \rangle$ yields predicted sintering dynamics via Eqs 1-3 that capture experimental sintering rates exceptionally well without any adjustable fitting procedures. By contrast, when packs are monodisperse particles in experiments, Wadsworth et al. (2017) found that the use of the calculated $\langle a_i \rangle$ results in predicted sintering rates that are faster than observations. They hypothesised that this is because of the geometrical assumptions underpinning the vented bubble model, which are only well-posed for polydisperse particle sizes. To accommodate this, they formulated a correction factor that adjusts $\langle a_i \rangle$ in the monodisperse limit of particle size distributions. This correction factor ψ was calibrated against a large dataset of sintering experiments in which $F(R_i)$ was changed systematically from monodisperse to highly polydisperse. The correction to $\langle a_i \rangle$ can be up to a factor of order 100 in the monodisperse limit. In this work, we do not report the details of the model that relates $F(R_i)$ to $F(a_i)$, and which yields the mean $\langle a_i \rangle$, the variance $\langle a_i^2 \rangle$, and the skewness $\langle a_i^3 \rangle$. $\langle a_i^n \rangle$ represents the n th moment of $F(a_i)$; instead the reader is referred to Wadsworth et al. (2017) and the related review work (Wadsworth et al., 2022c).

c. Degassing of particles during sintering: the ‘full’ diffusion-sintering model (Wadsworth et al., 2019)

Fragmented particles within the conduit are likely to contain dissolved H₂O, but upon fragmentation and deposition or emplacement, these particles can degas through ‘diffusive degassing’ (Weaver et al., 2022). Because the concentration of dissolved H₂O exerts a strong control on the particle viscosity (e.g. via Eq. 4), this degassing process can affect sintering in an important way. In a particle, the diffusion timescale is $\lambda_d = R^2/D$, where D is the temperature-dependent diffusivity of H₂O. λ_d can be compared with the sintering timescale λ to give a capillary Peclet number (Gardner et al., 2018; Wadsworth et al., 2019, 2021; Weaver et al., 2022, 2023; Vasseur et al., 2023)

$$\text{Pc} = \frac{\lambda_d}{\lambda} = \frac{\Gamma R^2}{a_i \mu D} \quad \text{Eq. 5}$$

This capillary Peclet number is a measure of whether sintering or diffusive degassing is more efficient, such that if $Pc \gg 1$, diffusion is slow compared with sintering, and if $Pc \ll 1$, diffusion is rapid compared with sintering. The consequence of this is that if $Pc \gg 1$, the H_2O concentration that may be most relevant for computing a particle viscosity, is the initial concentration, termed w_i . If we use w_i , then the associated viscosity can be termed an initial viscosity μ_i (i.e. the viscosity before diffusion has begun to reduce w from w_i ; computed via Eq. 4). Similarly, if $Pc \ll 1$, then the H_2O concentration that is most relevant is an equilibrium H_2O concentration given by the solubility at whatever temperature and water vapor pressure at which sintering is occurring. We term this equilibrium H_2O concentration w_e , which is associated with a viscosity μ_e via Eq. 4. The equilibrium solubility H_2O concentration is given by a constitutive law for the solubility, such as this calibrated for rhyolites (Liu et al., 2005)

$$w_e = \frac{k_1 P_{H_2O}^{1/2} + k_2 P_{H_2O} + k_3 P_{H_2O}^{3/2}}{T} + k_4 P_{H_2O}^{3/2} \quad \text{Eq. 6}$$

where $k_1 = 354.941$, $k_2 = 9.623$, $k_3 = -1.5223$, and $k_4 = 0.0012439$, respectively, and here T is in kelvin and P_{H_2O} is in MPa (Liu et al., 2005).

The diffusivity in Eq. 5 also requires a constitutive law, and here we use the model for rhyolites (Zhang and Ni, 2010)

$$D = w \exp \left[d_1 + d_2 P - \left(\frac{d_3 + d_4 P}{T} \right) \right] \quad \text{Eq. 7}$$

where $d_1 = -18.1$, $d_2 = 1.888 \times 10^{-3}$, $d_3 = 9699$, and $d_4 = 3.626$, and T and P are in kelvin and MPa, respectively. D at $w = w_e$ is then termed D_e .

Pc depends on μ and D , which both depend on w . Therefore, Gardner et al., (2018) chose to compute Pc at equilibrium conditions, rather than at initial conditions (i.e. using w_e in D and μ). Taking this approach, those authors found that up to $Pc = 9.9$, their experimental results were behaving in the low Pc regime, such that the sintering rates were consistent with an initial viscosity where no appreciable diffusion had taken place. Therefore, we take the regime boundary for Pc behaviour to be at least $Pc \leq 10$, rather than unity. We note that while Eq. 5 is strictly true, Gardner et al., (2018) and Wadsworth et al., (2019) proposed that an expedient simplification is to assume that $a_i \approx R$ and then that $Pc = \Gamma R / (\mu_e D_e)$, where here we have acknowledged that μ_e and D_e are appropriate choices (see above). In what follows, we will explore the Pc regime of our experimental results in which the sintering particles are supersaturated in H_2O at experimental conditions.

When $Pc \approx 1$, a ‘full model’ is required and an approximation found by taking either μ_i ($Pc \gg 1$) or μ_e ($Pc \ll 1$) is insufficient (Wadsworth et al., 2019). This full model is termed the ‘volc weld’ version of the VBM and involves numerically solving for the diffusion of H_2O out of the particles using Fick’s second law, and assuming that the particle boundary is immediately at the equilibrium value. This results in a time-dependent solution for the gradient of w in the particle, which can be converted to a gradient of viscosity μ via Eq. 4; this gradient is then used to find an average $\langle \mu \rangle$ in each particle, which is in turn used in Eq. 3 such that $\mu(T)$ becomes $\mu(T, w)$ in the integration to find \bar{t} . This procedure is described in some more detail in Wadsworth et al. (2019) who also provide a downloadable graphical user interface for volc weld. Here, this procedure is used as the ‘full model’ when analysing the data.

The assumption made above is that the particles do not vesiculate internally as a part of the degassing process. Existing results show that this is the case for very small particles, such as those considered here (Weaver et al., 2022), where diffusive loss of volatiles out of the clast edges is sufficiently efficient to reduce supersaturation before nucleation of bubbles inside the clast can occur. This would not be the case for larger particles which would internally vesiculate (this is discussed later).

4. Materials, material characterization, and experimental methods

We use a natural obsidian sample from Hrafninnuhryggur, Krafla (Iceland) collected *in situ* from location 'AO' on the ridge (65°41'33.72"N, 16°43'23.04"W; Tuffen and Castro, 2009). This obsidian is non-porous – i.e. porosity is zero, measured by pycnometry (Weaver et al., 2022) – and featureless with no obvious internal texture visible with scanning electron microscopy (Cáceres et al., 2020). The obsidian was crushed and ground slowly in acetone (to avoid excess heat from crushing) using an automated slow-moving agate pestle and mortar before being dried for four hours under air and in a flat bed <0.5 cm thick, to produce a powder. The obsidian powder was sieved using standard sieve sizes to <32, <63, and >90 μm grainsize fractions. We note that it is clear from the particle size distributions (discussed later) that some particle size fractions passed through these sieve sizes despite being apparently too large or too small for the stated size limits; this implies non-sphericity of the particles, which is clear from **Figs 3a-3c**.

The major element compositions of the particles are given in Table 1 (Tuffen and Castro, 2009). The powder is checked for any evidence of crystallization (see Section 4b), and is stored in vacuum sealed bottles between experiments to avoid adsorbed H_2O . We note that any adsorbed H_2O would be removed during heating before the glass transition interval and therefore would not impact high temperature sintering processes; see discussion in Giachetti et al., (2015) and Giachetti and Gonnermann, (2013). There is further evidence that adsorption of H_2O does not affect the results herein because the same experimental powder was used in Wadsworth et al., (2019) where the viscosity of the powder particles determined by differential scanning calorimetry (cf Gottsmann et al., 2002) matches the pre-crushing values found by other rheometric methods (Wadsworth et al., 2019).

a. Bulk rock X-ray fluorescence spectroscopy

Tuffen and Castro (2009) measured the composition of the glass from Hrafninnuhryggur obsidian samples using electron microprobe techniques. We repeat their major-element geochemical results in **Table 1**. To check that the obsidian we use matches their results, we use bulk rock X-ray fluorescence (XRF) using a Rigaku ZSX PrimusIV WD-XRF device at the Department of Geology, University of Leicester (U.K.). For this analysis major elements were determined on ~ 7 g fused glass beads with a sample-flux ratio of 1:7.5 and are recalculated to include the loss-on-ignition. The device is regularly calibrated on reference samples of basalt, granodiorite, rhyolite, gabbro, granite, and nepheline syenite (internal calibration performance available from the host laboratory on request). All XRF results are given in **Table 1** and cover a range of localities at Hrafninnuhryggur (see Tuffen and Castro (2009) for location codes given in **Table 1**).

b. Pre-experimental particle characterization

We mounted an aliquot of each sieved particle population on an adhesive carbon sticker on top of a metal stub, and carbon coated the particles before examining them using a Hitachi SU-70 high resolution scanning electron microscope (SEM) at the GJ Russell Microscopy Facility at Durham University (U.K.). Images were taken of each size fraction in secondary emission mode and with a 10 kV beam and a 15 mm working distance (**Figs 3a-3c**). Particle size distributions for the sieved particle populations were measured using a Bettersizer laser refraction particle size analyzer at the Ludwig-Maximilians-Universität (Munich, Germany) with a measuring range of 0.01 to 3,500 μm diameter. We repeated these measurements 10 times. The mean particle size $\langle R \rangle$ is reported in **Figs 3d-3f**. We also report the polydispersity S which is computed by taking the ratio $S = \langle R \rangle \langle R^2 \rangle / \langle R^3 \rangle$ where $\langle R^n \rangle$ is the n th moment of the distribution (i.e. $\langle R \rangle$ is the mean, $\langle R^2 \rangle$ is the variance, and $\langle R^3 \rangle$ is the skewness). $S = 1$ is strictly monodisperse whereas $S \rightarrow 0$ is highly polydisperse (i.e. it is for $S = 1$ that the correction factor discussed earlier is applied). The particle size distributions are provided in the Supplementary Information.

c. Continuous sintering experiments using optical dilatometry

The obsidian powders were used in *in situ* sintering experiments using a high temperature optical dilatometer (made by Hesse Instruments and housed at the Ludwig-Maximilians-Universität, Munich,

Germany). Loose powder (~ 10 mg) of each sieved particle size was first loaded into a pressure-gauged push rod and compacted with a force of exactly 3 N. This produced a free-standing cylindrical sample of approximately 3 mm in length held together by electrostatic forces. The application of 3 N of compacting force is insufficient to cause brittle fractures in particles, but is enough to produce small packings close to a maximum for angular particles (Boccaccini and Hamann, 1999; Oberacker, 2011). Applying more or less force may produce packs of different initial porosity ϕ_i but this would not affect the experimental results, except to change that starting value – we note that ϕ_i is accounted for in the model itself (see Eqs 1 & 2) and therefore varying this parameter is not a priority. Where this value has been varied via varying the particle distribution polydispersivity, we note that the vented bubble model for sintering captures that change in initial porosity well (Wadsworth et al., 2017b).

Samples were weighed pre-experiment, using an analytical balance, which has an accuracy of 0.01 mg (Figs 3g-3i). Each cylindrical sample was placed onto an alumina plate (95 wt% Al_2O_3) to then be pushed into the furnace of the optical dilatometer. The optical dilatometer consists of a halogen lamp, furnace, and CCD camera in series, so that the camera images the sample through the tube furnace during experiments (Fig. 4) and the in-furnace thermocouples are calibrated to within ± 2 K (using the melting point of gold wire that can be viewed live by the CCD camera). The camera tracks the geometry/size of the cylinder throughout the experiment. The raw data collected by the instrument include (1) sample height above the baseline base plate h , sample area, A , in 2D (where the area is the rectangular cross section of the cylinder as seen from the side), sample width W (in rectangular cross section), and the furnace and sample temperatures, T (measured using a sample thermocouple that is within 1 mm of the sample base plate). The device additionally outputs binary photographs of the cylinder as seen by the CCD camera (Fig. 4). The conditions of the individual experiments are given in Table 2.

d. X-ray computed tomography and sample volume calibrations

The data output by the optical dilatometer is sufficient to compute volumes of the samples assuming a cylindrical geometry (discussed later). However, in order to convert this to an absolute volume, and then a porosity, we require a reference volume or porosity. To acquire this information, we used X-ray computed tomography (XCT) to characterize the post-experimental samples. Sintered obsidian samples from the optical dilatometry experiments of each grain size fraction that reached equilibrium porosity were selected for XCT. The samples selected were, (1) <32 μm heated to 1200°C and held for 1,200 seconds, (2) $32 < x < 63$ μm heated to 1200°C and held for 10,800 seconds, (3) >90 μm heated to 1200°C and held for 1,200 seconds. The XCT data were obtained with a micro-CT scanner, Nikon XT H 225 LC. Scans were acquired with an accelerating voltage of 70 kV, a current of 90 μA and a 4 second exposure time. 3142 projections were collected over a 360° rotation for each 3D tomographic dataset; the scans have a voxel resolution of 1.98 μm . Reconstructed 3D data were visualised and processed using the AvizoTM (version 2022.1) ThermoFisherTM software. The scans were processed in order to collect isolated, connected and total porosity, as well as 3D images for data visualisation. The total porosity for each scan represents the final porosity ϕ_f for each particle size fraction. Scans were cropped using *Extract subvolume* to a cube with a 792 μm edge length to remove surrounding air and reduce the image size. A *non-local means* filter removed noise in the data before segmentation. *Labelling* performs a connectivity analysis of individual objects in a 3D volume, which are pores in this case. Segmented pores were labelled and measured using the *volume fraction* module, which gives the segmented 3D volume in voxels (rendered in Fig. 5). More detail of the AvizoTM method is given in the Supplementary Information.

e. The initial and final H_2O concentration of the glass

A key input to the models is the viscosity as a function of temperature (Eq. 4). This is highly sensitive to the dissolved H_2O concentration (Hess and Dingwell, 1996). Therefore, the initial value of the dissolved H_2O is required. The block of obsidian from which the powders were created is the same as used previously (Casas et al., 2019; Wadsworth et al., 2019, 2021; Coumans et al., 2020; Seropian et

al., 2022). Previously, thermogravimetry was used to determine that the H₂O concentration was initially 0.11 ± 0.02 wt. % (Wadsworth et al., 2019). This is consistent with infrared measurements (Seropian et al., 2022) and is within the range measured for the Hrafninnuhryggur ridge lavas (Tuffen and Castro, 2009).

The equilibrium H₂O value, termed w_e , that is pertinent to our experiments is given by Eq. 6. Eq. 6 takes as an input the partial pressure of H₂O, P_{H_2O} , which, because the optical dilatometer furnace is not a 100% water-vapour atmosphere, should be computed as $P_{H_2O} = P_g \alpha$ where α is the mole fraction of water in the atmosphere (i.e. in the fluid surrounding the particles). We follow previous work in assuming that the mole fraction is $\alpha = 0.15$ (i.e. approximately 15% humidity at high temperatures on a molar basis). This has been validated for sintering experiments (Wadsworth et al., 2019) and directly for bubble-growth experiments (von Aulock et al., 2017).

5. Raw experimental results and image analysis

The optical dilatometer outputs the temperature of the sample. We applied a constant heating rate of $10 \text{ }^\circ\text{C} \cdot \text{min}^{-1}$ up to a target isothermal hold of $1200 \text{ }^\circ\text{C}$ in all experiments. Some experiments were halted before the isotherm was reached, in order to retrieve a sample part-way through the heating portion. In **Figs 6a-6c** we report the $T(t)$ data output and we note that there are offsets in absolute time between sample runs because the time at which data collection commenced varied from run to run. The principal output is the sample area (i.e. in 2D) that is the approximately rectangular cross-section of the cylinder, termed A . This area (in pixels) is a function of time $A(t)$ and is automatically normalized to the initial area A_i , giving $A(t)/A_i$ (**Figs 6d-6f**). In all cases, the sample areas decrease as sintering begins and progresses. Depending on the experimental duration and temperature pathway, $A(t)/A_i$ can plateau to an apparent final equilibrium value. All raw data is provided as Supplementary Files.

To go beyond the raw area-time data (**Figs 6d-6f**), we undertake a volume calibration calculation using the X-ray computed tomography 3D datasets. For the samples scanned, the final quench porosity ϕ_f was measured using the volume fraction module in Avizo which gave $\phi_f = 0.01 \pm 0.005$ for the two samples that went to equilibrium volume (**Figs 5a & 5b**) and $\phi_f = 0.11 \pm 0.005$ for the sample that did not reach volume equilibrium (**Fig. 5c**). Using these quench porosity values, we can compute porosity continuously from the $A(t)/A_i$ data. We do this by noting that $\phi = 1 - \rho/\rho_g$, where ρ is the bulk sample density and ρ_g is the density of the sintering dense glass. Therefore, the final porosity, ϕ_f , is given by $\phi_f = 1 - \rho_f/\rho_g$, where ρ_f is the value of ρ at the end of the experiment. Given that ϕ_f and ρ_g are known values, this can be rearranged to get $\rho_f = \rho_g(1 - \phi_f)$. For $\rho_g = 2400 \text{ kg} \cdot \text{m}^{-3}$, which is the average density of this rhyolitic liquid (Iacovino and Till, 2019) and $\phi_f = 0.01$, this gives $\rho_f = 2376 \text{ kg} \cdot \text{m}^{-3}$. In turn, by assuming that the mass of the sample is constant (and therefore that the pores are of negligible mass), the final volume is $V_f = m_i/\rho_f$, where m_i is the initial mass (**Figs 3g-3i**). This leads to $V_f = 4.41 \times 10^{-9} \text{ m}^3$. To compute the continuous volume data V as a function of time, a cylindrical shape is assumed. In this case, $V = V_i (A/A_i)^{3/2}$, where V_i and A_i are the initial volume and initial 2D cross sectional areas, respectively, and A is the time-dependent cross sectional area (Wadsworth et al., 2016). The difficulty is in knowing V_i a priori. Instead, we have constrained the final volume, V_f . An equivalent statement for V is $V = V_f (A/A_f)^{3/2}$, where A_f is the final sample cross sectional area. Because A/A_f is a ratio of areas, the measured pixel areas can be used without requiring a scaled calibration for a pixel length. Therefore, we divide all measured area values by the final value to get A/A_f . Then, using the computed V_f , V can be calculated. As a final step, porosity can be computed as $\phi = 1 - m_i/(V\rho_g)$, where $V/m_i = \rho$.

Using the workflow given above, we report the porosity evolution for the two samples that went to equilibrium and which were scanned using X-ray computed tomography (**Figs 6g-6i**). Given that these are for three different particle size distributions, and yet both start at $\phi_i \approx 0.6$, we make the assumption that $\phi_i = 0.6$ is the universal starting porosity for all data for this angular obsidian. Using

this assumption we can calibrate all remaining datasets by using $V_i = m_i/[\rho_g(1 - \phi_i)]$ then $V = V_i (A/A_i)^{3/2}$ and the solution for $\phi(V)$ given above. Here, we explain this procedure for computing in a step-by-step manner. However, the steps can be simplified into a computational step that is for $\phi(t)$ when V_f and ϕ_f (**Figs 6g-6i**) are known or $\phi(t)$ when V_i and ϕ_i are known (**Figs 6j-6l**)

$$\phi(t) = 1 - \frac{1 - \phi_f}{\bar{V}_f}; \quad \bar{V}_f = \frac{V}{V_f} \quad \text{Eq. 8a}$$

$$\phi(t) = 1 - \frac{1 - \phi_i}{\bar{V}_i}; \quad \bar{V}_i = \frac{V}{V_i} \quad \text{Eq. 8b}$$

The final $\phi(t)$ data are all reported in **Figs 6j-6l** grouped by the common values of the mean particle radius $\langle R \rangle$ (therefore **Figs 6i & 6l** are the same because for that grain size there was only a single experiment).

6. Analysis: experiments and models

The raw data in **Fig. 6** show that for all datasets the porosity decreases as a function of time spent at high temperature. This porosity loss is typical of sintering systems as the gas between the coalescing droplets is expelled from the sample. Here we compare the empirical data with the theoretical model described in Section 2.

a. Testing the full VBM degassing-sintering model

In these analysis steps we first recast the experimental time relative to a reference time, giving $t = t_{\text{exp}} - t_{\text{ref}}$ where t_{exp} is the experimental time given in **Fig. 6**. To do this, we take $t_{\text{ref}} = 740$ °C, which is an approximate dry glass transition temperature for this rhyolite (Wadsworth et al., 2022b). By redefining the time in this way, we account for the fact that data collection began at different times for different experiments (discussed in Section 4). The result of this for each grain size is shown in **Fig. 7** where the figure shows the same data as in **Figs 6j-6l**, and the expected result that the data all fall together (due to the common thermal history for every sample) is found (**Fig. 7**). In **Fig. 7** we show that the VBM described in Section 2a with the diffusive degassing computation described in Section 2c captures the data remarkably well, without any adjustment, fine-tuning, or fits or minimization (**Fig. 7**). This ‘full VBM’ solution accounts for the mean particle size, the particle size distribution, the non-isothermal changing temperature, the diffusive degassing of H₂O out of the particles toward a changing equilibrium w_e , and the resultant evolution of average particle viscosity. The goodness of fit and theoretical nature of this model suggests that it could be used to model obsidian particle welding in nature, even at conditions not captured explicitly by these experiments. Despite the general success of the fit, the model does not capture (1) the long time evolution toward equilibrium porosity of the samples that began with a particle size $\langle R \rangle = 17.1$ μm (**Fig. 7b**), and (2) the short time behaviour of the sample that began with a particle size $\langle R \rangle = 64.3$ μm (**Fig. 7c**). Both of these observations are discussed later. The goodness of fit of the VBM implies that the clear non-sphericity and potential anisotropy of the particle shapes (**Figs 3a-3c**) are second-order effects and that the spherical assumption made in the VBM is sufficient (cf Reis et al., 2018).

b. The end-member cases of $\text{Pc} \ll 1$ and $\text{Pc} \gg 1$

Clearly, the data follow the ‘full VBM’ model (**Fig. 7**). However, solving for the time-dependent diffusive losses of H₂O out of the particles *during* sintering is an involved calculation (Wadsworth et al., 2019, 2021) and may not be necessary in all cases. For example, if $\text{Pc} \ll 1$ (termed the $\text{Pc} = 0$ regime), then diffusive losses are so much quicker than the sintering that the equilibrium H₂O solubility and associated ‘dry’ temperature-dependent viscosity can be assumed. Similarly, if $\text{Pc} \gg 1$

(termed the $Pc = \infty$ regime), then the diffusive losses can be assumed to be so slow that the initial H_2O can be assumed to be constant throughout the sintering process, and therefore the initial ‘wet’ temperature-dependent viscosity can be assumed. Either of these end-member cases simplifies the sintering calculation considerably and is worth testing here.

In the case of the two relatively finer grain sizes, $\langle R \rangle = 13.2 \mu\text{m}$ (**Fig. 7a**) and $\langle R \rangle = 17.1 \mu\text{m}$ (**Fig. 7b**), $Pc = 4.6$ and $Pc = 6.0$, respectively, implying that the $Pc = 0$ model should work effectively (Table 3). This is confirmed by the analysis presented in **Figs 7a & 7b**. There we compute the sintering using $\mu(T)$ via Eqs 3 & 4 but by taking either (1) a constant $w_f = 0.04 \text{ wt.}\%$ which is w_e at the target temperature of $1200 \text{ }^\circ\text{C}$, or (2) a changing w_e that varies with temperature computed via Eq. 6. In either case, this $Pc = 0$ calculation is at least as effective as the full VBM, showing that when $Pc \ll 1$, simplified sintering models that do not account for time-dependent diffusion can be used instead. We provide such a simplified model as an Excel™ downloadable tool with this submission.

The larger grainsize sample $\langle R \rangle = 64.3 \mu\text{m}$ clearly behaves differently when compared with the two relatively finer grained samples (**Fig. 7c**). This larger grainsize is at $Pc = 22.1$ (Table 3), such that the sintering and diffusion times are close to being similar and diffusion will still be occurring when the sintering is ongoing. For this case, of intermediate Pc , the full VBM should work effectively. However, instead, the sample begins its sintering by following the prediction made for the $Pc = \infty$ model, before transitioning to the $Pc = 0$ model (and the full VBM). This indicates that there is some physics not captured by the full VBM, such that apparently the w_i and associated μ_i may be important for the initial phase of sintering at $1 \leq Pc \leq 10$. This is discussed further later.

c. Collapse of data for all grainsizes to the dimensionless VBM

The first step of analysis shows that all data appear to match the predictions made by the full VBM and the simplified $Pc = 0$ behaviour (**Fig. 7**; the short and long time behaviour discussed in Section 5b notwithstanding). Therefore, we can test the degree to which this behaviour is universally scaled by the sintering time given by Eq. 3. To do this, we compute \bar{t} using Eq. 3 with Eq. 4. The result is a collapse of all data to a single model prediction regardless of the initial grainsize (**Fig. 8a**). As inferred from the goodness of fit in **Fig. 7**, this collapse is equally good if we use the full VBM to define \bar{t} (**Fig. 8a**) or the VBM using the final water content w_f assuming $Pc = 0$ (**Fig. 8b**). This universality compared across grainsizes also allows us to conclude that the apparent complexity with the short-time behaviour of the largest grain size sample (**Fig. 7c**) appears to be minor compared with the overall trend of standard sintering whereby $\phi \rightarrow 0$.

7. Sample micro-texture evolution

Natural sintered products from Hrafninnuhryggur generally show rounded clasts with evidence for the crystallization of oxide nanolites and clast-clast necks and/or flattening (**Fig. 1**). In **Fig. 9** we give an overview of the micro-structures recorded by our experiments. The micro-structures are organized by grain size of the starting material and in time-order in terms of \bar{t} , spanning $\bar{t} \ll 1$ to $\bar{t} \sim 1$, which covers incipiently sintered through to fully sintered material. In all cases, it is clear that the sintering results in clast rounding (e.g. compare **Fig. 9b** with **Fig. 9a**, or **Fig. 9f** with **Fig. 9e**), the precipitation of surface nanolites (e.g. **Figs 9c & 9f**), and the closure of pore space, eventually ending with isolated rounded pores in a glass matrix (**Figs 9d & 9h**).

We additionally focus in on some specific textures of interest (**Fig. 10**). The balance between neck formation and clast rounding appears to be different in the two smallest grainsize populations (compare **Fig. 10a** with **Fig. 10d**), where the slightly larger grain size material appears to round off while necks form, whereas the fine material forms necks prior to thorough clast rounding. Our experimental textures can capture the tri-cusped pores (**Figs 10b, 10c, & 10e**), which are found in the natural samples **Fig. 1**. If left for longer time at high temperature, then sintering concludes with the rounding of those same tri-cusped pores (**Fig. 10f**). Approximately, it appears that the final pore sizes remnant in the samples is proportional to the initial particle sizes, which has been discussed

previously (Wadsworth et al., 2016) and may represent a way in which particle sizes can be discerned even in thoroughly sintered materials.

8. Discussion

Sintering is a key process in the evolution of explosive silicic eruptions. Here we can summarize the key areas where models for sintering may be especially important: (1) in the deposition of particularly hot clasts from pyroclastic density currents (Branney and Kokelaar, 1992); (2) in the subsurface in-conduit capture, sintering, and shear deformation of clasts that can clog conduits and result in a switch to clastogenic lava extrusion (Wadsworth et al., 2020; Trafton and Giachetti, 2022); and (3) in the pyroclastic injection of tuffisites into country rock (Kolzenburg et al., 2019; Heap et al., 2019; Unwin et al., 2021). We frame our discussion around two broad areas; first, we discuss aspects of the model and model comparison with data that warrant further explication/exploration, and second, we apply these models to place constraints on the inferred dynamics at play during the emplacement of Hrafninnuhryggur - a rhyolite fissure eruption.

a. The effect of particle size

A key novelty in this contribution is the experimental test of the effect of particle size. Previous contributions have explicitly tested the effect of particle size and particle size distribution shape when it comes to inert (non-hydrous) glass sintering (Prado et al., 2001; Lara et al., 2004; Wadsworth et al., 2017b). In that case of non-hydrous glass particle sintering, the effect of particle size is given by the sintering timescale $\lambda \approx \langle R \rangle \mu / \Gamma$, as discussed in **Section 3**. Note then that the effect of particle size, $\langle R \rangle$, is usually a linear one in terms of the controlling timescale. However, when the particles are also hydrous and supersaturated at experimental conditions, then there is an additional effect, which is that as H₂O diffuses out of the particles, the particle viscosity becomes a function of time $\mu = f(t)$ (see **Eq. 4**). The full vented bubble model shows this by accounting for that diffusive loss of H₂O and explicitly solving for the volume average of the H₂O concentration in the particles and then therefore numerically defining the pathway that viscosity takes for each time-step. Given that the concentration of H₂O diffuses approximately proportional to $\lambda_d \approx \langle R \rangle^2 / D$, this implicates the square of the particle size as a controlling factor here; therefore this complexity is worth discussing.

The complexity in question relates to $Pc = \Gamma \langle R \rangle / (\mu_e D_e)$ (**Eq. 5**; see modification in **Section 3c**). If we follow the empirical result from Gardner et al. (2018) that $Pc \approx 10$ represents the boundary between regimes, then we can rearrange Pc for the critical particle size. $\langle R \rangle_c = 10 \mu_e D_e / \Gamma$. If the particle sizes in the sintering are around the value $\langle R \rangle_c$, then diffusion of H₂O will have an impact on the sintering, whereas if the particles are smaller than $\langle R \rangle_c$, then diffusion of H₂O will be rapid and the equilibrium H₂O will simply be attained prior to sintering getting going. We find that $\langle R \rangle < \langle R \rangle_c$ for the experiments that involve the '<32 μm ' sieved particles, and the '<63 μm ' sieved particles (this is equivalent to saying $Pc \ll 1$ behaviour is met). In turn, this explains why all experiments that utilize those two particle populations all collapse almost perfectly to the model when the normalizations by λ are made (see **Figs 7 & 8**). In this regime then the effect of particle size is simply linear and proportional to $\langle R \rangle$.

We find that the particle population sieved to $>90 \mu\text{m}$ occur at $\langle R \rangle \approx \langle R \rangle_c$ (equivalent to saying $Pc \approx 10$; **Table 3**). The expectation for $\langle R \rangle \approx \langle R \rangle_c$ is that gradients of H₂O will impact the sintering. That expectation is borne out by the data which show a kink in the $\phi(t)$ curves (see **Fig. 6i**). When normalized by λ , those same data do start out by collapsing to the full VBM model but then deviate (**Fig. 7**). This shows that the effect of particle size at intermediate Pc is substantial and not well-captured by the VBM.

The final possibility is that $\langle R \rangle \gg \langle R \rangle_c$. The technique we use to examine sintering is one in which this regime cannot be readily reached (see **Fig. 4** for the technique) because the technique relies on electrostatic forces holding the particles in their cylindrical dye-formed shape. Particles that are much larger than those used here do not form easy-to-load samples. However, Weaver et al. (2022) provide experiments using the same obsidian material from Hrafninnuhryggur, but at millimetric particles

$\langle R \rangle \gg \langle R \rangle_c$. Those results demonstrate that when particles are sufficiently large that diffusive gradients in H₂O are large, then vesiculation occurs internal to the particles prior to the onset of sintering (Weaver et al. 2022; 2023). That kind of vesiculated texture is seen at Hrafninnuhryggur, albeit only in flow-related breccia clasts (discussed later). Therefore, we conclude that the VBM is well suited to predicting sintering of hydrous particles that are small relative to the well-defined $\langle R \rangle_c$ and that when particles fall into that category, then the effect of particle size is linear.

b. Comparison with existing sintering datasets and the ‘universal sintering curve’ for relatively small particles

Here we repeat the data from this study for sintering of Hrafninnuhryggur obsidian particles cast as a function of normalized time \bar{t} , which accounts for time-dependent diffusive outgassing losses of H₂O (as in **Fig. 8a** or Section 5c). However, here we additionally apply the normalization $\bar{\phi} = \phi/\phi_i$, meaning that the full VBM curve is solved exactly as given in **Eq. 2 (Fig. 11)**. We present the data collapsed to the full VBM again in **Fig. 11** in order to show that this dimensionless model matches all available published datasets and is therefore a ‘universal sintering curve’ when presented in this transformed manner. The datasets we analyse in this manner include sintering glass beads and synthetic glass fragments (Jagota et al., 1990; Prado et al., 2001; Lara et al., 2004; Vasseur et al., 2013; Wadsworth et al., 2014; Vasseur et al., 2016; Wadsworth et al., 2016, 2017a, 2017b; Reis et al., 2018), as well as sintering obsidian particles from Mono Craters (Gardner et al., 2018, 2019) and from Hrafninnuhryggur (Wadsworth et al., 2019, 2021). The collapse of all these data is particularly remarkable given that these data include particle distributions that range from monodisperse to highly polydisperse, and sample treatments that cover a very wide range of isothermal and non-isothermal temperature histories, and a wide range of initial and final H₂O concentrations. Given this very diverse sample selection and treatment conditions, we propose that the VBM is indeed a universal model for sintering. Clearly from **Fig. 11** we can conclude that the additional effects found for particularly large sintering hydrous particles (e.g. **Fig. 7c**) are among the only exceptions to the universality of the VBM for glassy particles. This comparison between **Fig. 11** and the data in **Fig. 7c** leads us to conclude that the VBM is a universal model for ‘small’ particles (see **Section 8a**), where ‘small’ is relative to the gradients of H₂O that can persist during sintering at $P_c \gtrsim 10$.

It is possible that adsorbed H₂O was present on the powder grain surfaces at the start of the heating ramp; this would occur in any sample of powder that is stored in air (Martin et al., 1998). Upon heating, we might expect that adsorbed H₂O would diffuse into the particles once high relative temperatures are reached (sufficiently high to allow for efficient diffusion). However, the amounts of adsorbed H₂O are relatively low (Nakashima et al., 2019). And even though that diffusive addition of H₂O would occur at or proximal to the particle surfaces, exactly where the sintering force originates (Wakai et al., 2016; Okuma et al., 2017), we note that most experimental results fall in the $P_c \ll 1$ regime where diffusive equilibration on the particle scale is far more rapid than the sintering rate; therefore, adsorbed H₂O would be lost at the experimental sintering temperatures before it could affect sintering. If adsorbed H₂O were an issue, then the results would not collapse to our universal sintering curve in the way that they do.

c. Equilibrium final porosity, dense non-vesicular obsidian, and nanolites

The VBM as it is given here predicts that the final porosity approaches zero as sintering progresses in its final stage (e.g. **Fig. 7**). By contrast, all of the experimental data presented here (**Fig. 6**) show that there is a residual final porosity at the end of sintering. Indeed, our X-ray computed tomography data for samples that have completed sintering show that on average the final porosity is $\phi_f = 0.01$. This is consistent with most available sintering data which all have a small final porosity remnant at the end of sintering (Jagota et al., 1990; Prado et al., 2001; Lara et al., 2004; Wadsworth et al., 2016, 2019). In experiments where the pore fluid is air – which is largely insoluble in silicate particles such as obsidian – this final porosity is stable because the permeability of that gas phase has dropped to zero at the end of sintering (Wadsworth et al., 2017a; Okuma et al., 2017; Colombier et al., 2020; Wadsworth et al., 2023). Put another way, some final pore space volume gets pinched off and isolated

as sintering goes to completion, and if that gas phase that is then trapped is inert and insoluble, it will transition to rounded bubbles and remain trapped in the final sintered mass. In some experiments where the temperature is increased after this isolation event occurs, it is clear that the equation-of-state expansion of the trapped gas can then ‘puff up’ sintered materials (Song et al., 2014, 2017). From a model perspective, Wadsworth et al. (2016) proposed a way to capture this final porosity by rescaling the normalized porosity. Instead of defining $\bar{\phi} = \phi/\phi_i$, they suggested that $\bar{\phi} = (\phi - \phi_f)/(\phi_i - \phi_f)$ in Eq. 2. This change will force the model to approach $\phi = \phi_f$ as $t \gg \lambda$ instead of $\phi = 0$. However, the final porosity is such a small amount, that we leave this as a small mismatch between model and data at the end of sintering (see Fig. 7). In the natural samples presented in Fig. 1, it is clear that there are examples where there is a remnant porosity that looks very much like it could be explained by a ‘pinch off’ event at the end of sintering (e.g. cusped isolated vesicles; Fig. 9). In other samples where sintering has formed completely dense obsidian with no sign of remnant porosity (Tuffen and Castro, 2009; Wadsworth et al., 2018). The cooling-related resorption of trapped H₂O (McIntosh et al., 2014; Ryan et al., 2015) can readily explain the extinction of end-of-sintering related vesicles and the formation of fully dense non-vesicular obsidian (as discussed in Foster et al. 2024).

There are subtle differences between the experimental samples (Figs 9 & 10) and the natural materials (Fig. 1), mostly associated with the crystals near or at particle rims (presumed to be oxide crystals after Caceres et al. 2020 who examined the same obsidian). We note that in Fig. 1b it is clear that the surface-proximal crystals are nanolites where individual crystals can be identified at a scale less than 1 μm ; but in the experimental samples, it is less clear whether the bright rim-proximal SEM result is a nanolitized rim, or some other phenomenon such as an Fe-enriched rim (Burkhard, 2001). The proximity to clast edges precludes most analytical techniques and therefore we assume that the experimental rim-proximal bright SEM result is attributable to nanolite formation. This is supported by the natural samples, which evidence the propensity for nanolite formation in these particles.

In the natural samples, these form either internal to the particles (Fig. 1e) or apparently some distance in from the particle edges. Foster et al. (2024) showed evidence that the gas vapour pressure $P_{\text{H}_2\text{O}}$ varied as a function of time in the natural case, increasing as the eruption progressed and the conduit clogged. Therefore, there was a ‘regassing’ event. It is reasonable to assume that the nanolites typically form in response to degassing of the particles and that nanolite number density and/or size tracks the gradient of H₂O in the particles (cf Di Genova et al., 2018). Any regassing event due to gas pressurization causes H₂O to diffuse back into the edges of the particles – see dark greyscale rims in Fig. 1, where darker greys represent higher relative H₂O; (Humphreys et al., 2008; McIntosh et al., 2014). However, it does not necessarily follow that resorption of H₂O into the particle edges would reverse the formation of nanolite crystals; more work is needed to understand if that would be the case and the relationship with the glass $f\text{O}_2$. Nevertheless, Fig. 1 shows that in the natural samples, the rims of the particles are apparently nanolite-poor as well as exhibiting darker grey attributed to H₂O resorption; this confluence of texture is not captured in our experiments.

We suggest a few scenarios relevant to both nature and our experiments:

- First, the formation of dense nanolite-free obsidian by sintering is possible if the degassing occurs down to a low H₂O value of 0.1-0.2 wt.% observed in the Hrafninnuhryggur glass (Tuffen and Castro, 2009). The H₂O evolution therefore is depicted in Fig. 12a and the associated textures in Fig. 12b. If the partial pressure of H₂O remains high (i.e. close to the total gas pressure) then nanolite formation seems to be inhibited.
- Second, as the eruption waned and stalled (which is typical of silicic eruption progression (Pallister et al., 2013)) atmospheric air mixed into the shallow conduit and dropped the equilibrium solubility via a drop in partial pressure of H₂O, This allows particles to degas to sufficiently low H₂O to allow precipitation of nanolites. The particles that track this ‘late stage’ sintering with air involved are typically found in fractures in lava and do have the exceptionally low H₂O that would occur in sintering at $P_{\text{H}_2\text{O}} < 1$ bar pressure; very low H₂O has been recorded at Hrafninnuhryggur (Tuffen and Castro, 2009). The subsequent regassing event recorded at Hrafninnuhryggur could potentially then result in nanolite-free rims that are more hydrous than the nanolite-bearing particle interiors (Fig 12c & 12d). The caveat to this step is that it is not clear if nanolite precipitation is reversible simply by H₂O resorption,

even if the nanolite formation in the first place is triggered by H₂O removal (cf Di Genova et al., 2017; Scarani et al., 2022; Pereira et al., 2024).

- Sintering at very low $P_{\text{H}_2\text{O}}$ in the laboratory such as performed here and previously (Wadsworth et al., 2019, 2021; Weaver et al., 2023) would form nanolites only at the particle rims, and would not replicate the regassing event inferred to have occurred in nature (**Figs 12e & 12f**), leaving nanolite oxide-bearing particle rims (**Figs 9 & 10**); see caveat above.
- Finally, if the same laboratory sintering is performed for particles that are large relative to the diffusion distances, which is the case for our largest particles presented here (i.e. at $P_c \geq 10$), then the primary degassing can result in substantial gradients in H₂O internal to the particles at the point when sintering completes (**Figs 12g & 12h**). In this case, further time-dependent degassing into the trapped pore spaces could occur, resulting in higher ϕ_f values – this effect requires further work to understand.

As nanolites or microlites of oxides form at the particle surfaces, it is worth considering if they would impact the sintering rates. The two most likely effects would be (1) via the effect of crystals on particle viscosity (Wadsworth et al., 2022c; Blandon et al., 2023); and (2) the effect of the crystallization on the residual melt viscosity (Zandonà et al., 2023; Cáceres et al., 2024; Pereira et al., 2024).

The first effect is well-predicted by simple rheological models (Mueller et al., 2010), which hold that the crystal-bearing viscosity μ_x is proportional to $\mu_x = \mu(1 - \phi_x/\phi_m)^{-2}$, where ϕ_x is the local crystallinity, and ϕ_m is the maximum packing. Inspection of the SEM images makes it clear that determination of ϕ_x is not possible without much higher magnifications. However, we note that the difference between μ_x and μ is small until $\phi_x/\phi_m \gtrsim 0.35$ (assuming $\phi_m = 0.63$; Mueller et al., 2010). The second effect is harder to determine and would require that we know the nanolite crystal chemistry well; but proximity to the particle surfaces compromise chemical analysis. Nevertheless, this second effect would also impact the viscosity via a change in μ (in addition to the μ_x effect).

Ultimately, it is hard to determine if the particle-bearing particle rim viscosity is a big factor in this analysis. Similarly, it remains unknown how large crystal-bearing rim must be before the boundary layer thickness at the particle edge is sufficient to affect sintering rates. What is clear is that for the two particle populations sieved to <32 and <63 μm are not affected by this (i.e. they collapse to the VBM despite their crystal-bearing rims). Future work should consider rim devitrification and how it could potentially affect sintering rates.

d. Application of sintering dynamics to understand the Hrafninnuhryggur eruption and the effect of temperature

In **Fig. 12i** we show schematically how the eruption model described briefly above can be represented. Pyroclasts are captured at the conduit walls during the explosive phase of the eruption and sinter to form patches or layers of dense melt. The sintering model presented and validated herein allows us to place quantitative constraints on the timescales and feasibility of this process. To do this, we use **Fig. 1** as motivation where incipiently sintered particles are approximately $R \approx 10$ μm . This grain size is consistent with models for sinter-assembly of lava which show that $R \leq 10$ μm is the grain size most likely to explain thoroughly degassed lava (Wadsworth et al., 2020). Taking this as the characteristic lengthscale, we can compute an isothermal sintering timescale $\lambda \approx \mu R/\Gamma$ where we take $\Gamma = 0.3$ $\text{N}\cdot\text{m}^{-1}$ and $\mu(T)$ using **Eq. 4**. In the $\mu(T)$ law we follow Wadsworth et al. (2020) in assuming that at the point of fragmentation the initial H₂O concentration is $w_i = 0.5$ wt.%. This is based on conduit models that suggest that at fragmentation this is how much H₂O is left in the melt after bubble growth has occurred to the degree required for fragmentation. The result of this calculation is a curve $\lambda(T)$ using w_i (**Fig. 13**). As the particles degas, w drops below w_i and approaches w_e , which we take to be the value observed at the surface $w_e \approx 0.1$ wt.% (Tuffen and Castro, 2009). This drop suggests that $\lambda(T)$ transitions from the initial curve (using w_i) to the final curve (using w_e).

In addition to the sintering timescale λ , we can compute the diffusion timescale $\lambda_D = R^2/D$ where we compute $D(T)$ using **Eq. 7** and $w = w_e$ (via **Eq. 6** at 0.1 MPa $P_{\text{H}_2\text{O}}$). In **Fig. 13** the comparison

between λ and λ_D at the temperature range of 750-850 °C (Foster et al. 2024) shows that indeed diffusion is more rapid than sintering for the thorough sintering at Hrafninnuhryggur (**Fig. 13**). This is consistent with the observation that the lavas are all thoroughly degassed and yet densely sintered with exceptionally low porosity.

The curves for λ using either w_i or w_e is the timescale required for thorough sintering (i.e. $t = \lambda$, or equivalently $\bar{t} = 1$, occurs when $\phi \approx 0$; see **Figs 7 & 10**). For some of the materials found at Hrafninnuhryggur, the sintering is only incipient (**Fig. 1**). In the master sintering curve (**Fig. 11**) we can see that sintering onsets around $\bar{t} = 0.01$ or, equivalently, $t = 0.01\lambda$. Therefore, we also plot the $10^{-2}\lambda$ curve(s) on **Fig. 13**. In this case, the sintering timescale $10^{-2}\lambda$ and the diffusion timescale λ_D are reasonably similar, suggesting that both processes are occurring at the same time at the temperature range given above – the particles are beginning to sinter incipiently while diffusion is promoting loss of H₂O. This is again consistent with the qualitative observations in **Fig. 1** that the incipiently sintered particles have grayscale gradients that are likely to represent a captured disequilibrium H₂O profile. With reference to the timescale map, those incipiently welded textures are consistent with a total timescale of around ~ 100 s for incipient sintering to occur with some diffusion onset. We therefore suggest that rapid cooling, possibly associated with adiabatic heat loss in the pyroclast-and-gas mixture expansion up-conduit (Mastin and Ghiorso, 2001) took on the order of ~ 100 s for the incipiently sintered sample (**Fig. 1**). Clearly, however, the thoroughly sintered bulk of the lavas cooled more slowly than that, allowing complete sintering at $t = \lambda$ which could be of order 2-3 hours (**Fig. 13**).

e. Sintering of pumice versus dense obsidian

At Hrafninnuhryggur, most of the sintering textures involve dense obsidian particles (**Fig. 1**). However, Foster et al. (2024) found that the conduit lining comprises pumice lapilli, which progressively grade into dense welded obsidian. This raises the question: are pumice particles also sintering to form dense obsidian? If this were the case, then the sintering dynamics may differ from those explored here. Particles that start life as dense obsidian can vesiculate internally and then diffusely outgas to return to their dense state (Yoshimura and Nakamura, 2008; Weaver et al., 2022). For this process to occur, the starting dense particle has to be sufficiently large to vesiculate internally. We posit that this is likely to only occur for $Pc \gg 1$, and therefore could be the case for our largest particle size used here where $Pc > 10$ and could be a component of the explanation for why that sample behaves differently from the nominally ‘fine grained’ obsidian particles that are at $Pc < 1$. Having said that, the particle size that is typically thought to dominate silicic lava production by sintering is ~ 10 μm or less (Wadsworth et al., 2020; Farquharson et al., 2022) in order to explain the low H₂O by diffusive outgassing during transport and to be consistent with the particle capture dynamics at the conduit wall. Therefore, while the very initial particles seen at the conduit wall are pumiceous lapilli that are larger than 10 μm , this may quickly shift to fine-grained and dense particles. Secondary vesiculation then can produce domains of vesicular obsidian with apparent rims of dense obsidian that demonstrate that late stage vesiculation and progressive diffusive outgassing can occur subsequent to primary capture and sintering (**Fig. 14**; Weaver et al., 2022, 2023).

9. Concluding remarks

We have designed and executed dynamic experiments in which Hrafninnuhryggur obsidian particles of a range of grain sizes and grain size distributions are packed together and sintered at elevated temperatures up to 1200 °C. Those experiments confirm that the dominant process of amalgamation of rhyolite particles by sintering is a non-linear evolution from high porosity to low porosity, ending at an equilibrium porosity that is almost zero, albeit with some remnant trapped pores isolated at process completion. We compare our experimental data with dynamic sintering models that include the diffusion of H₂O out of the particles during sintering; this model matches our data exceptionally well and provides confidence that the sintering timescale is well constrained. Using that timescale, we can place quantitative constraints on the time required to form the textures observed in the natural rhyolite at Hrafninnuhryggur and we conclude that these were formed after particle capture in timescales of

<1 hour to a few hours (the latter being pertinent for wholesale dense lava production and the former being applicable to final-stage incipient sintering within lava fractures).

Journal Pre-proof

Acknowledgments

We thank Kai-Uwe Hess and Ulrich Kueppers for facilitating access to laboratory facilities at the Ludwig-Maximilians-Universität, Munich (Germany) in summer 2022 and Eloïse Bretagne for experimental assistance. Landsvirkjun are thanked for their assistance and hospitality during fieldwork campaigns at Krafla. We are indebted to Yan Lavallée, Jackie Kendrick, Joshua Weaver, Julia Schunke, and Anthony Lamur for discussions relating to vesiculation during sintering and the associated complexities (10.1016/j.epsl.2023.118410) that are not dealt with further here. We are grateful for additional informative discussions with Holly Unwin, David Zhang, and Ed Llewellyn. Holly Unwin and Taylor Witcher provided fieldwork support in Iceland in 2021 and 2017, respectively. Annabelle Foster was funded by a UKRI PhD studentship as part of the IAPETUS Doctoral Training Programme. Support was provided by a NERC-funded Pushing the Frontiers grant (NE/X015440/1). Ed Llewellyn is thanked a second time for stepping in concerning the supervision of Annabelle Foster while Fabian Wadsworth was in hospital in summer 2023 and during his subsequent recovery which is ongoing at the time of writing.

Author contributions

A. Foster performed the experiments and led both the data analysis and manuscript drafting. F.B. Wadsworth and J. Vasseur analyzed the data further. H. Tuffen provided fieldwork support and field/textural context that informed the experiments performed. M. Humphreys, D.B. Dingwell, and K.J. Dobson provided additional analytical support and volcanological background. All authors contributed to the manuscript.

Conflict statement

The authors declare no conflicts of interest.

Reference cited

- Andrews, G.D.M., and Branney, M.J., 2011, Emplacement and rheomorphic deformation of a large, lava-like rhyolitic ignimbrite: Grey's Landing, southern Idaho: *Geological Society of America Bulletin*, v. 123, p. 725–743, doi:10.1130/b30167.1.
- Arzilli, F. et al., 2019, Magma fragmentation in highly explosive basaltic eruptions induced by rapid crystallization: *Nature Geoscience*, v. 12, p. 1023–1028, doi:10.1038/s41561-019-0468-6.
- von Aulock, F.W., Kennedy, B.M.B.M., Maksimenko, A., Wadsworth, F.B., and Lavallée, Y., 2017, Outgassing from open and closed magma foams: *Frontiers in Earth Science*, v. 5, doi:10.3389/feart.2017.00046.
- Blandon, R., Gardner, J.E., Wadsworth, F.B., Llewellyn, E.W., and Vasseur, J., 2023, Experimental sintering of crystal-rich rhyolitic ash at high fluid pressures with implications for degassing of magma: *Bulletin of Volcanology*, v. 85, p. 63, doi:10.1007/s00445-023-01678-5.
- Boccaccini, A.R., and Hamann, B., 1999, Review in situ high-temperature optical microscopy: *Journal of Materials Science*, v. 34, p. 5419–5436.
- Branney, M.J., and Kokelaar, P., 1992, A reappraisal of ignimbrite emplacement: progressive aggradation and changes from particulate to non-particulate flow during emplacement of high-grade ignimbrite: *Bulletin of Volcanology*, v. 54, p. 504–520, doi:10.1007/BF00301396.
- Branney, M.J., and Kokelaar, B.P., 2002, *Pyroclastic density currents and the sedimentation of ignimbrites*: London, The Geological Society of London, pp. 150 p.
- Branney, M.J., Kokelaar, B.P., and McConnell, B., 1992, The Bad Step Tuff: a lava-like rheomorphic ignimbrite in a calc-alkaline piecemeal caldera, English Lake District: *Bulletin of Volcanology*, v. 54, p. 187–199, doi:10.1007/BF00278388.
- Burkhard, D.J.M., 2001, Crystallization and Oxidation of Kilauea Basalt Glass: Processes during Reheating Experiments: *Journal of Petrology*, v. 42, p. 507–527,

doi:10.1093/petrology/42.3.507.

- Cáceres, F., Hess, K.-U., Eitel, M., Döblinger, M., McCartney, K.N., Colombier, M., Gilder, S.A., Scheu, B., Kaliwoda, M., and Dingwell, D.B., 2024, Oxide nanolitisation-induced melt iron extraction causes viscosity jumps and enhanced explosivity in silicic magma: *Nature Communications*, v. 15, p. 604, doi:10.1038/s41467-024-44850-x.
- Cáceres, F., Wadsworth, F.B., Scheu, B., Colombier, M., Madonna, C., Cimarelli, C., Hess, K.U., Kaliwoda, M., Ruthensteiner, B., and Dingwell, D.B., 2020, Can nanolites enhance eruption explosivity? *Geology*, v. 48, p. 997–1001, doi:10.1130/G47317.1.
- Carbillet, L., Heap, M.J., Baud, P., Wadsworth, F.B., and Reuschlé, T., 2021, Mechanical Compaction of Crustal Analogs Made of Sintered Glass Beads: The Influence of Porosity and Grain Size: *Journal of Geophysical Research: Solid Earth*, v. 126, p. e2020JB021321, doi:https://doi.org/10.1029/2020JB021321.
- Carbillet, L., Heap, M.J., Baud, P., Wadsworth, F.B., and Reuschlé, T., 2022, The Influence of Grain Size Distribution on Mechanical Compaction and Compaction Localization in Porous Rocks: *Journal of Geophysical Research: Solid Earth*, v. 127, p. e2022JB025216, doi:https://doi.org/10.1029/2022JB025216.
- Casas, A.S., Wadsworth, F.B., Ayris, P.M., Delmelle, P., Vasseur, J., Cimarelli, C., and Dingwell, D.B., 2019, SO₂ scrubbing during percolation through rhyolitic volcanic domes: *Geochimica et Cosmochimica Acta*, doi:10.1016/j.gca.2019.04.013.
- Castro, J.M., Bindeman, I.N., Tuffen, H., and Ian Schipper, C., 2014, Explosive origin of silicic lava: Textural and $\delta D-H_2O$ evidence for pyroclastic degassing during rhyolite effusion: *Earth and Planetary Science Letters*, v. 405, p. 52–61, doi:https://doi.org/10.1016/j.epsl.2014.08.012.
- Castro, J.M., Cordonnier, B., Tuffen, H., Tobin, M.J., Puskar, L., Martin, M.C., and Bechtel, H.A., 2012, The role of melt-fracture degassing in defusing explosive rhyolite eruptions at volcán Chaitén: *Earth and Planetary Science Letters*, v. 333–334, p. 63–69, doi:https://doi.org/10.1016/j.epsl.2012.04.024.
- Coble, R.L., and Kingery, W.D., 1956, Effect of Porosity on Physical Properties of Sintered Alumina: *Journal of the American Ceramic Society*, v. 39, p. 377–385, doi:https://doi.org/10.1111/j.1151-2916.1956.tb15608.x.
- Colombier, M., Wadsworth, F.F.B., Gurioli, L., Scheu, B., Kueppers, U., Di Muro, A., and Dingwell, D.B., 2017, The evolution of pore connectivity in volcanic rocks: v. 462, doi:10.1016/j.epsl.2017.01.011.
- Colombier, M., Wadsworth, F.B., Scheu, B., Vasseur, J., Dobson, K.J., Cáceres, F., Allabar, A., Marone, F., Schlepütz, C.M., and Dingwell, D.B., 2020, In situ observation of the percolation threshold in multiphase magma analogues: *Bulletin of Volcanology*, v. 82, p. 32, doi:10.1007/s00445-020-1370-1.
- Cordonnier, B., Schmalholz, S.M., Hess, K.U., and Dingwell, D.B., 2012, Viscous heating in silicate melts: An experimental and numerical comparison: *Journal of Geophysical Research: Solid Earth*, v. 117, p. B02203, doi:10.1029/2010JB007982.
- Coumans, J.P., Llewellyn, E.W., Wadsworth, F.B., Humphreys, M.C.S., Mathias, S.A., Yelverton, B.M., and Gardner, J.E., 2020, An experimentally validated numerical model for bubble growth in magma: *Journal of Volcanology and Geothermal Research*, v. 402, p. 107002, doi:https://doi.org/10.1016/j.jvolgeores.2020.107002.
- Degruyter, W., Bachmann, O., Burgisser, A., and Manga, M., 2012, The effects of outgassing on the transition between effusive and explosive silicic eruptions: *Earth and Planetary Science Letters*, v. 349, p. 161–170, doi:10.1016/j.epsl.2012.06.056.
- Eberstein, M., Reinsch, S., Müller, R., Deubener, J., and Schiller, W.A., 2009, Sintering of glass matrix composites with small rigid inclusions: *Journal of the European Ceramic Society*, v. 29, p. 2469–2479.
- Eichheimer, P., Thielmann, M., Fujita, W., Golabek, G.J., Nakamura, M., Okumura, S., Nakatani, T.,

- and Kottwitz, M.O., 2020, Combined numerical and experimental study of microstructure and permeability in porous granular media: *Solid Earth*, v. 11, p. 1079–1095, doi:10.5194/se-11-1079-2020.
- Ellis, B.S., Pimentel, A., Cortes-Calderon, E.A., Moser, Z., Baumann, N., Bachmann, O., and Wadsworth, F.B., 2023, Obsidian clasts as sintered remnants of agglutination processes in volcanic conduits, evidence from the Pepom tephra (Sete Cidades), São Miguel, Azores: *Chemical Geology*, v. 638, p. 121694, doi:<https://doi.org/10.1016/j.chemgeo.2023.121694>.
- Farquharson, J., Tuffen, H., Wadsworth, F., Castro, J., and Schipper, C.I., 2022, In-conduit capture of sub-micron volcanic ash particles via turbophoresis and sintering: *Nature Communications*, doi:10.21203/rs.3.rs-1152244/v1.
- Farquharson, J.I., Wadsworth, F.B., Heap, M.J., and Baud, P., 2017, Time-dependent permeability evolution in compacting volcanic fracture systems and implications for gas overpressure: *Journal of Volcanology and Geothermal Research*, v. 339, p. 81–97, doi:10.1016/j.jvolgeores.2017.04.025.
- Foster, A., Wadsworth, F.B., Tuffen, H., Unwin, H.E., and Humphreys, M.C.S., 2024, Evidence for the formation of silicic lava by pyroclast sintering: *Nature Communications*, v. 15, p. 5347, doi:10.1038/s41467-024-49601-6.
- Frenkel, J., 1945, Viscous flow of crystalline bodies under the action of surface tension: *J. Phys.*, v. 9, p. 385–391.
- Gardner, J.E., Llewellyn, E.W., Watkins, J.M., and Befus, K.S., 2017, Formation of obsidian pyroclasts by sintering of ash particles in the volcanic conduit: *Earth and Planetary Science Letters*, v. 459, p. 252–263, doi:10.1016/J.EPSL.2016.11.037.
- Gardner, J.E., Wadsworth, F.B., Llewellyn, E.W., Watkins, J.M., and Coumans, J.P., 2019, Experimental constraints on the textures and origin of obsidian pyroclasts: *Bulletin of Volcanology*, v. 81, p. 22, doi:10.1007/s00445-019-1283-z.
- Gardner, J.E., Wadsworth, F.B., Llewellyn, E.W., Watkins, J.M., and Coumans, J.P., 2018, Experimental sintering of ash at conduit conditions and implications for the longevity of tuffisites: *Bulletin of Volcanology*, v. 80, p. 23, doi:10.1007/s00445-018-1202-8.
- Di Genova, D., Caracciolo, A., and Kolzenburg, S., 2018, Measuring the degree of “nanotilization” of volcanic glasses: Understanding syn-eruptive processes recorded in melt inclusions: *Lithos*, v. 318–319, p. 209–218, doi:<https://doi.org/10.1016/j.lithos.2018.08.011>.
- Di Genova, D., Sicola, S., Romano, C., Vona, A., Fanara, S., and Spina, L., 2017, Effect of iron and nanolites on Raman spectra of volcanic glasses: A reassessment of existing strategies to estimate the water content: *Chemical Geology*, v. 475, p. 76–86, doi:<https://doi.org/10.1016/j.chemgeo.2017.10.035>.
- Giachetti, T., and Gonnermann, H.M., 2013, Water in volcanic pyroclast: Rehydration or incomplete degassing? *Earth and Planetary Science Letters*, v. 369–370, p. 317–332, doi:<https://doi.org/10.1016/j.epsl.2013.03.041>.
- Giachetti, T., Gonnermann, H.M., Gardner, J.E., Shea, T., and Gouldstone, A., 2015, Discriminating secondary from magmatic water in rhyolitic matrix-glass of volcanic pyroclasts using thermogravimetric analysis: *Geochimica et Cosmochimica Acta*, v. 148, p. 457–476, doi:<https://doi.org/10.1016/j.gca.2014.10.017>.
- Giachetti, T., Trafton, K.R., Wiejaczka, J., Gardner, J.E., Watkins, J.M., Shea, T., and Wright, H.M.N., 2021, The products of primary magma fragmentation finally revealed by pumice agglomerates: *Geology*, v. 49, p. 1307–1311, doi:10.1130/G48902.1.
- Gonnermann, H.M., 2015, Magma Fragmentation: *Annual Review of Earth and Planetary Sciences*, v. 43, p. 431–458, doi:10.1146/annurev-earth-060614-105206.
- Gottsmann, J., Giordano, D., and Dingwell, D.B., 2002, Predicting shear viscosity during volcanic processes at the glass transition: a calorimetric calibration: *Earth and Planetary Science Letters*, v. 198, p. 417–427, doi:[https://doi.org/10.1016/S0012-821X\(02\)00522-8](https://doi.org/10.1016/S0012-821X(02)00522-8).

- Grunder, A.L., Laporte, D., and Druitt, T.H., 2005, Experimental and textural investigation of welding: effects of compaction, sintering, and vapor-phase crystallization in the rhyolitic Rattlesnake Tuff: *Journal of Volcanology and Geothermal Research*, v. 142, p. 89–104, doi:<http://dx.doi.org/10.1016/j.jvolgeores.2004.10.018>.
- Heap, M.J., Tuffen, H., Wadsworth, F.B., Reuschlé, T., Castro, J.M., and Schipper, C.I., 2019, The Permeability Evolution of Tuffisites and Implications for Outgassing Through Dense Rhyolitic Magma: *Journal of Geophysical Research: Solid Earth*, v. 124, p. 8281–8299, doi:[10.1029/2018jb017035](https://doi.org/10.1029/2018jb017035).
- Heiken, G., Wohletz, K., and Eichelberger, J., 1988, Fracture fillings and intrusive pyroclasts, Inyo Domes, California: *Journal of Geophysical Research: Solid Earth*, v. 93, p. 4335–4350, doi:<https://doi.org/10.1029/JB093iB05p04335>.
- Hess, K.-U.U., and Dingwell, D.B., 1996, Viscosities of hydrous leucogranitic melts: A non-Arrhenian model: *American Mineralogist*, v. 81, p. 1297–1300.
- Hjartardóttir, Á.R., Einarsson, P., Bramham, E., and Wright, T.J., 2012, The Krafla fissure swarm, Iceland, and its formation by rifting events: *Bulletin of Volcanology*, v. 74, p. 2139–2153, doi:[10.1007/s00445-012-0659-0](https://doi.org/10.1007/s00445-012-0659-0).
- Humphreys, M.C.S., Menand, T., Blundy, J.D., and Klimm, K., 2008, Magma ascent rates in explosive eruptions: Constraints from H₂O diffusion in melt inclusions: *Earth and Planetary Science Letters*, v. 270, p. 25–40, doi:<https://doi.org/10.1016/j.epsl.2008.02.041>.
- Iacovino, K., and Till, C.B., 2019, DensityX: A program for calculating the densities of magmatic liquids up to 1,627 °C and 30 kbar: *Volcanica*, v. 2, p. 1–10, doi:[10.30909/vol.02.01.0110](https://doi.org/10.30909/vol.02.01.0110).
- Jagota, A., Mikeska, K.R., and Bordia, R.K., 1990, Isotropic Constitutive Model for Sintering Particle Packings: *Journal of the American Ceramic Society*, v. 73, p. 2266–2273, doi:[10.1111/j.1151-2916.1990.tb07587.x](https://doi.org/10.1111/j.1151-2916.1990.tb07587.x).
- Kang, S.-J.L., 2004, *Sintering: densification, grain growth and microstructure*: Butterworth-Heinemann.
- Kendrick, J.E., Lavallée, Y., Varley, N.R., Wadsworth, F.B., Lamb, O.D., and Vasseur, J., 2016, Blowing off steam: Tuffisite formation as a regulator for lava dome eruptions: *Frontiers in Earth Science*, v. 4, doi:[10.3389/feart.2016.00041](https://doi.org/10.3389/feart.2016.00041).
- Kolzenburg, S., Heap, M.J., Lavallée, Y., Russell, J.K., Meredith, P.G., and Dingwell, D.B., 2012, Strength and permeability recovery of tuffisite-bearing andesite: *Solid Earth*, v. 3, p. 191–198, doi:[10.5194/se-3-191-2012](https://doi.org/10.5194/se-3-191-2012).
- Kolzenburg, S., Ryan, A.G., and Russell, J.K., 2019, Permeability evolution during non-isothermal compaction in volcanic conduits and tuffisite veins: Implications for pressure monitoring of volcanic edifices: *Earth and Planetary Science Letters*, v. 527, p. 115783, doi:[10.1016/j.epsl.2019.115783](https://doi.org/10.1016/j.epsl.2019.115783).
- Kueppers, U., Scheu, B., Spieler, O., and Dingwell, D.B., 2006, Fragmentation efficiency of explosive volcanic eruptions: A study of experimentally generated pyroclasts: *Journal of Volcanology and Geothermal Research*, v. 153, p. 125–135, doi:<https://doi.org/10.1016/j.jvolgeores.2005.08.006>.
- Lara, C., Pascual, M.J., Prado, M.O., and Duran, A., 2004, Sintering of glasses in the system RO–Al₂O₃–BaO–SiO₂ (R= Ca, Mg, Zn) studied by hot-stage microscopy: *Solid State Ionics*, v. 170, p. 201–208.
- Lavallée, Y. et al., 2015a, Eruption and emplacement timescales of ignimbrite super-eruptions from thermo-kinetics of glass shards: *Frontiers in Earth Science*, v. 3, p. 2, doi:[10.3389/feart.2015.00002](https://doi.org/10.3389/feart.2015.00002).
- Lavallée, Y. et al., 2015b, Thermal vesiculation during volcanic eruptions: *Nature*, v. 528, p. 544–547, doi:[10.1038/nature16153](https://doi.org/10.1038/nature16153).
- Lavallée, Y., Hirose, T., Kendrick, J.E., De Angelis, S., Petrakova, L., Hornby, A.J., and Dingwell, D.B., 2014, A frictional law for volcanic ash gouge: *Earth and Planetary Science Letters*, v. 400, p. 177–183, doi:<https://doi.org/10.1016/j.epsl.2014.05.023>.

- Liu, Y., Zhang, Y., and Behrens, H., 2005, Solubility of H_2O in rhyolitic melts at low pressures and a new empirical model for mixed H_2O - CO_2 solubility in rhyolitic melts: *Journal of Volcanology and Geothermal Research*, v. 143, p. 219–235.
- Mackenzie, J.K., and Shuttleworth, R., 1949, A phenomenological theory of sintering: *Proceedings of the Physical Society. Section B*, v. 62, p. 833.
- Martin, L.P., Poret, J.C., Danon, A., and Rosen, M., 1998, Effect of adsorbed water on the ultrasonic velocity in alumina powder compacts: *Materials Science and Engineering: A*, v. 252, p. 27–35, doi:[https://doi.org/10.1016/S0921-5093\(98\)00669-8](https://doi.org/10.1016/S0921-5093(98)00669-8).
- Mastin, L.G., 2002, Insights into volcanic conduit flow from an open-source numerical model: *Geochemistry, Geophysics, Geosystems*, v. 3, p. 1–18, doi:[10.1029/2001GC000192](https://doi.org/10.1029/2001GC000192).
- Mastin, L.G., and Ghiorso, M.S., 2001, Adiabatic temperature changes of magma–gas mixtures during ascent and eruption: *Contributions to Mineralogy and Petrology*, v. 141, p. 307–321, doi:[10.1007/s004100000210](https://doi.org/10.1007/s004100000210).
- McIntosh, I.M., Llewellyn, E.W., Humphreys, M.C.S.S., Nichols, A.R.L.L., Burgisser, A., Schipper, C.I., and Larsen, J.F., 2014, Distribution of dissolved water in magmatic glass records growth and resorption of bubbles: *Earth and Planetary Science Letters*, v. 401, p. 1–11, doi:<https://doi.org/10.1016/j.epsl.2014.05.037>.
- Monnereau, L.R., Ellis, B.S., Szymanowski, D., Bachmann, O., and Guillong, M., 2021, Obsidian pyroclasts in the Yellowstone-Snake River Plain ignimbrites are dominantly juvenile in origin: *Bulletin of Volcanology*, v. 83, p. 27, doi:[10.1007/s00445-021-01448-1](https://doi.org/10.1007/s00445-021-01448-1).
- Mueller, S., Llewellyn, E.W., and Mader, H.M., 2010, The rheology of suspensions of solid particles: *Proceedings of the Royal Society A: Mathematical, Physical and Engineering Science*, v. 466, p. 1201–1228.
- Nakashima, Y., Razavi-Khosroshahi, H., Takai, C., and Fuji, M., 2019, Non-firing ceramics: Effect of adsorbed water on surface activation of silica powder via ball milling treatment: *Advanced Powder Technology*, v. 30, p. 1160–1164, doi:<https://doi.org/10.1016/j.apt.2019.03.011>.
- Oberacker, R., 2011, Powder Compaction by Dry Pressing, *in* *Ceramics Science and Technology*, p. 1–37, doi:<https://doi.org/10.1002/9783527631957.ch1>.
- Okuma, G., Kadowaki, D., Hondo, T., Tanaka, S., and Wakai, F., 2017, Interface topology for distinguishing stages of sintering: *Scientific Reports*, v. 7, p. 11106, doi:[10.1038/s41598-017-11667-2](https://doi.org/10.1038/s41598-017-11667-2).
- Pallister, J.S., Diefenbach, A.K., Burton, W.C., Muñoz, J., Griswold, J.P., Lara, L.E., Lowenstern, J.B., and Valenzuela, C.E., 2013, The chaitén Rhyolite lava dome: Eruption sequence, lava dome volumes, rapid effusion rates and source of the Rhyolite magma: *Andean Geology*, v. 40, p. 277–294, doi:[10.5027/andgeoV40n2-a06](https://doi.org/10.5027/andgeoV40n2-a06).
- Pereira, L., Linard, Y., Wadsworth, F.B., Vasseur, J., Hess, K.-U., Moretti, R., Dingwell, D.B., and Neuville, D.R., 2024, The rheological response of magma to nanolitisation: *Journal of Volcanology and Geothermal Research*, p. 108039, doi:<https://doi.org/10.1016/j.jvolgeores.2024.108039>.
- Prado, M., Dutra Zanotto, E., and Müller, R., 2001, Model for sintering polydispersed glass particles: *Journal of non-crystalline solids*, v. 279, p. 169–178.
- Quane, S.L., and Russell, J.K., 2006, Bulk and particle strain analysis in high-temperature deformation experiments: *Journal of Volcanology and Geothermal Research*, v. 154, p. 63–73.
- Quane, S.L., and Russell, J.K., 2005a, Ranking welding intensity in pyroclastic deposits: *Bulletin of Volcanology*, v. 67, p. 129–143, doi:[10.1007/s00445-004-0367-5](https://doi.org/10.1007/s00445-004-0367-5).
- Quane, S.L., and Russell, J.K., 2005b, Welding: insights from high-temperature analogue experiments: *Journal of Volcanology and Geothermal Research*, v. 142, p. 67–87, doi:[http://dx.doi.org/10.1016/j.jvolgeores.2004.10.014](https://doi.org/10.1016/j.jvolgeores.2004.10.014).

- Quane, S.L., Russell, J.K., and Friedlander, E.A., 2009, Time scales of compaction in volcanic systems: *Geology*, v. 37, p. 471–474.
- Reis, R.M.C.V., Barbosa, A.J., Ghussn, L., Ferreira, E.B., Prado, M.O., and Zanotto, E.D., 2018, Sintering and rounding kinetics of irregular glass particles: *Journal of the American Ceramic Society*, v. 102, doi:10.1111/jace.15997.
- Ryan, A.G., Russell, J.K., Heap, M.J., Zimmerman, M.E., and Wadsworth, F.B., 2020, Timescales of porosity and permeability loss by solid-state sintering: *Earth and Planetary Science Letters*, v. 549, p. 116533, doi:https://doi.org/10.1016/j.epsl.2020.116533.
- Ryan, A.G., Russell, J.K., Nichols, A.R.L., Hess, K.-U., and Porritt, L.A., 2015, Experiments and models on H₂O retrograde solubility in volcanic systems: *American Mineralogist*, v. 100, p. 774–786, doi:10.2138/AM-2015-5030.
- Saubin, E., Tuffen, H., Gurioli, L., Owen, J., Castro, J.M., Berlo, K., McGowan, E.M., Schipper, C.I., and Wehbe, K., 2016, Conduit Dynamics in Transitional Rhyolitic Activity Recorded by Tuffisite Vein Textures from the 2008–2009 Chaitén Eruption : *Frontiers in Earth Science* , v. 4, p. 59, https://www.frontiersin.org/article/10.3389/feart.2016.00059.
- Scarani, A. et al., 2022, A chemical threshold controls nanocrystallization and degassing behaviour in basalt magmas: *Communications Earth & Environment*, v. 3, p. 284, doi:10.1038/s43247-022-00615-2.
- Scherer, G.W., 1986, Viscous sintering under a uniaxial load: *Journal of the American Ceramic Society*, v. 69, p. C-206–C-207.
- Scheu, B., and Dingwell, D.B., 2022, Magma Fragmentation: *Reviews in Mineralogy and Geochemistry*, v. 87, p. 767–800, doi:10.2138/rmg.2021.87.16.
- Schipper, C.I. et al., 2021, Silicic conduits as supersized tuffisites: Clastogenic influences on shifting eruption styles at Cordón Caulle volcano (Chile): *Bulletin of Volcanology*, v. 83, p. 11, doi:10.1007/s00445-020-01432-1.
- Schipper, C.I., Castro, J.M., Tuffen, H., James, M.R., and How, P., 2013, Shallow vent architecture during hybrid explosive–effusive activity at Cordón Caulle (Chile, 2011–12): Evidence from direct observations and pyroclast textures: *Journal of Volcanology and Geothermal Research*, v. 262, p. 25–37, doi:https://doi.org/10.1016/j.jvolgeores.2013.06.005.
- Seropian, G. et al., 2022, Vesiculation of rhyolitic melts under oscillatory pressure: *Frontiers in Earth Science*, p. 219, doi:10.3389/FEART.2022.812311.
- Sheikh, J.M., Sheth, H., Naik, A., and Keluskar, T., 2020, Widespread rheomorphic and lava-like silicic ignimbrites overlying flood basalts in the northwestern and northern Deccan Traps: *Bulletin of Volcanology*, v. 82, p. 41, doi:10.1007/s00445-020-01381-9.
- Song, W., Hess, K.K.-U., Damby, D.E.D.E., Wadsworth, F.B., Lavallée, Y., Cimarelli, C., and Dingwell, D.B.D.B., 2014, Fusion characteristics of volcanic ash relevant to aviation hazards: *Geophysical Research Letters*, v. 41, p. 2326–2333, doi:10.1002/2013GL059182.
- Song, W., Lavallée, Y., Wadsworth, F.B., Hess, K.-U., and Dingwell, D.B., 2017, Wetting and Spreading of Molten Volcanic Ash in Jet Engines: *Journal of Physical Chemistry Letters*, v. 8, doi:10.1021/acs.jpcclett.7b00417.
- Sparks, R.S.J., Self, S., and Walker, G.P.L., 1973, Products of Ignimbrite Eruptions: *Geology*, v. 1, p. 115–118, doi:10.1130/0091-7613(1973)1<115:POIE>2.0.CO;2.
- Sparks, R.S.J., Tait, S.R., and Yanev, Y., 1999, Dense welding caused by volatile resorption: *Journal of the Geological Society*, v. 156, p. 217–225, doi:10.1144/gsjgs.156.2.0217.
- Stasiuk, M. V., Barclay, J., Carroll, M.R., Jaupart, C., Ratté, J.C., Sparks, R.S.J., and Tait, S.R., 1996, Degassing during magma ascent in the Mule Creek vent (USA): *Bulletin of Volcanology*, v. 58, p. 117–130.
- Streck, M.J., and Grunder, A.L., 1995, Crystallization and welding variations in a widespread ignimbrite sheet; the Rattlesnake Tuff, eastern Oregon, USA: *Bulletin of Volcanology*, v. 57, p.

151–169, doi:10.1007/BF00265035.

- Torquato, S., 2013, Random heterogeneous materials: microstructure and macroscopic properties: Springer Science & Business Media, v. 16, 701 p.
- Trafton, K.R., and Giachetti, T., 2022, The pivotal role of Vulcanian activity in ending the explosive phase of rhyolitic eruptions: the case of the Big Obsidian Flow eruption (Newberry Volcano, USA): *Bulletin of Volcanology*, v. 84, p. 104, doi:10.1007/s00445-022-01610-3.
- Tuffen, H., and Castro, J.M., 2009, The emplacement of an obsidian dyke through thin ice: Hrafninnuhryggur, Krafla Iceland: *Journal of Volcanology and Geothermal Research*, v. 185, p. 352–366.
- Tuffen, H., and Dingwell, D.B., 2005, Fault textures in volcanic conduits: evidence for seismic trigger mechanisms during silicic eruptions: *Bulletin of Volcanology*, v. 67, p. 370–387, doi:10.1007/s00445-004-0383-5.
- Tuffen, H., Dingwell, D.B., and Pinkerton, H., 2003, Repeated fracture and healing of silicic magma generate flow banding and earthquakes? *Geology*, v. 31, p. 1089–1092, doi:10.1130/g19777.1.
- Tuffen, H., Farquharson, J.I., Wadsworth, F.B., Webb, C., Owen, J., Castro, J.M., Berlo, K., Schipper, C.I., and Wehbe, K., 2022, Mid-loaf crisis: Internal breadcrust surfaces in rhyolitic pyroclasts reveal dehydration quenching: *Geology*, v. 50, p. 1058–1062, doi:10.1130/G49959.1.
- Unwin, H.E., Tuffen, H., Phillips, E., Wadsworth, F.B., and James, M.R., 2021, Pressure-Driven Opening and Filling of a Volcanic Hydrofracture Recorded by Tuffisite at Húsafell, Iceland: A Potential Seismic Source : *Frontiers in Earth Science* , v. 9, p. 347, <https://www.frontiersin.org/article/10.3389/feart.2021.668058>.
- Unwin, H.E., Tuffen, H., Wadsworth, F.B., Phillips, E.R., James, M.R., Foster, A., Kolzenburg, S., Castro, J.M., and Porritt, L.A., 2023, The exposed Mule Creek vent deposits record the structure of a volcanic conduit during a hybrid explosive–effusive eruption: *Bulletin of Volcanology*, v. 85, p. 28, doi:10.1007/s00445-023-01638-z.
- Vasseur, J., Wadsworth, F.B., Lavallée, Y., and Dingwell, D.B., 2023, Dehydration-driven mass loss from packs of sintering hydrous silicate glass particles: *Journal of the American Ceramic Society*, v. 106, p. 4643–4653, doi:<https://doi.org/10.1111/jace.19120>.
- Vasseur, J., Wadsworth, F.B., Lavallée, Y., and Dingwell, D.B., 2016, Dynamic elastic moduli during isotropic densification of initially granular media: *Geophysical Journal International*, v. 204, p. 1721–1728, doi:10.1093/gji/ggv550.
- Vasseur, J., Wadsworth, F.B., Lavallée, Y., Hess, K.U., and Dingwell, D.B., 2013, Volcanic sintering: Timescales of viscous densification and strength recovery: *Geophysical Research Letters*, v. 40, p. 5658–5664, doi:10.1002/2013GL058105.
- Wadsworth, F.B. et al., 2019, A general model for welding of ash particles in volcanic systems validated using in situ X-ray tomography: *Earth and Planetary Science Letters*, v. 525, p. 115726, doi:<https://doi.org/10.1016/j.epsl.2019.115726>.
- Wadsworth, F.B. et al., 2021, A model for permeability evolution during volcanic welding: *Journal of Volcanology and Geothermal Research*, v. 409, p. 107118, doi:<https://doi.org/10.1016/j.jvolgeores.2020.107118>.
- Wadsworth, F.B. et al., 2022a, A reappraisal of explosive–effusive silicic eruption dynamics: syn-eruptive assembly of lava from the products of cryptic fragmentation: *Journal of Volcanology and Geothermal Research*, p. 107672, doi:<https://doi.org/10.1016/j.jvolgeores.2022.107672>.
- Wadsworth, F.B. et al., 2017a, Topological inversions in coalescing granular media control fluid-flow regimes: *Physical Review E*, v. 96, p. 033113, doi:10.1103/PhysRevE.96.033113.
- Wadsworth, F. Ben et al., 2022b, Using obsidian in glass art practice: *Volcanica*, v. 5, p. 183–207, doi:10.30909/vol.05.01.183207.
- Wadsworth, F.B., Llewellyn, E.W., Vasseur, J., Gardner, J.E., and Tuffen, H., 2020, Explosive-effusive volcanic eruption transitions caused by sintering: *Science Advances*, v. 6, p. eaba7940,

doi:10.1126/sciadv.aba7940.

- Wadsworth, F.B., and Tuffen, H., 2016, Into the volcano: Geoscientist, <https://www.geolsoc.org.uk/Geoscientist/Archive/February-2016/Into-the-Volcano>.
- Wadsworth, F.B., Vasseur, J., Aulock, F.W., Hess, K., Scheu, B., Lavallée, Y., and Dingwell, D.B., 2014, Nonisothermal viscous sintering of volcanic ash: *Journal of Geophysical Research: Solid Earth*, v. 119, p. 8792–8804.
- Wadsworth, F.B., Vasseur, J., Heap, M.J., Carbillet, L., Dingwell, D.B., Reuschlé, T., and Baud, P., 2023, A universal model for the permeability of sintered materials: *Acta Materialia*, v. 250, p. 118859, doi:<https://doi.org/10.1016/j.actamat.2023.118859>.
- Wadsworth, F.B., Vasseur, J., Llewellyn, E.W., and Dingwell, D.B., 2022c, Hot Sintering of Melts, Glasses and Magmas: *Reviews in Mineralogy and Geochemistry*, v. 87, p. 801–840, doi:10.2138/RMG.2022.87.17.
- Wadsworth, F.B., Vasseur, J., Llewellyn, E.W., and Dingwell, D.B., 2017b, Sintering of polydisperse viscous droplets: *Physical Review E*, v. 95, p. 033114, doi:10.1103/PhysRevE.95.033114.
- Wadsworth, F.B., Vasseur, J., Llewellyn, E.W., Schaubert, J., Dobson, K.J., Scheu, B., and Dingwell, D.B., 2016, Sintering of viscous droplets under surface tension: *Proceedings of the Royal Society A: Mathematical, Physical and Engineering Sciences*, v. 472, p. 20150780, doi:10.1098/rspa.2015.0780.
- Wadsworth, F.B., Witcher, T., Vossen, C.E.J., Hess, K.U., Unwin, H.E., Scheu, B., Castro, J.M., and Dingwell, D.B., 2018, Combined effusive-explosive silicic volcanism straddles the multiphase viscous-to-brittle transition: *Nature Communications*, v. 9, p. 1–8, doi:10.1038/s41467-018-07187-w.
- Wakai, F., Katsura, K., Kanchika, S., Shinoda, Y., Akatsu, T., and Shinagawa, K., 2016, Sintering force behind the viscous sintering of two particles: *Acta Materialia*, v. 109, p. 292–299.
- Wang, Y., Gardner, J.E., and Hoblitt, R.P., 2021, Formation of dense pyroclasts by sintering of ash particles during the preclimactic eruptions of Mt. Pinatubo in 1991: *Bulletin of Volcanology*, v. 83, p. 6, doi:10.1007/s00445-020-01427-y.
- Weaver, J., Lamur, A., Lea, T.D., Wadsworth, F.B., Kendrick, J.E., Schaubert, J., and Lavallée, Y., 2023, Sintering of vesiculating pyroclasts: *Earth and Planetary Science Letters*, v. 623, p. 118410, doi:<https://doi.org/10.1016/j.epsl.2023.118410>.
- Weaver, J., Lavallée, Y., Ashraf, M., Kendrick, J.E., Lamur, A., Schaubert, J., and Wadsworth, F.B., 2022, Vesiculation and densification of pyroclasts: A clast-size dependent competition between bubble growth and diffusive outgassing: *Journal of Volcanology and Geothermal Research*, p. 107550, doi:<https://doi.org/10.1016/j.jvolgeores.2022.107550>.
- Yoshimura, S., and Nakamura, M., 2008, Diffusive dehydration and bubble resorption during open-system degassing of rhyolitic melts: *Journal of Volcanology and Geothermal Research*, v. 178, p. 72–80, doi:<https://doi.org/10.1016/j.jvolgeores.2008.01.017>.
- Zandonà, A., Scarani, A., Löschmann, J., Cicconi, M.R., Di Fiore, F., de Ligny, D., Deubener, J., Vona, A., Allix, M., and Di Genova, D., 2023, Non-stoichiometric crystal nucleation in a spodumene glass containing TiO₂ as seed former: Effects on the viscosity of the residual melt: *Journal of Non-Crystalline Solids*, v. 619, p. 122563, doi:<https://doi.org/10.1016/j.jnoncrysol.2023.122563>.
- Zhang, Y., and Ni, H., 2010, Diffusion of H, C, and O components in silicate melts: *Reviews in Mineralogy and Geochemistry*, v. 72, p. 171–225, doi:10.2138/rmg.2010.72.5.
- Zierenberg, R.A. et al., 2013, Composition and origin of rhyolite melt intersected by drilling in the Krafla geothermal field, Iceland: *Contributions to Mineralogy and Petrology*, v. 165, p. 327–347, doi:10.1007/s00410-012-0811-z.

Table 1. Glass composition of obsidian particles

Sample name	Electron Microprobe					X-ray fluorescence (whole rock)											
	S11b*	N9a*	S37c*	HHO_1	HHO_2	GTA 168	AO	RED W	HH Pumice	HH2- 1	K-08- C	K-08- A					
Locality**	E	P	AO	AO	G												
n	110	136	100	24	45	1	1	1	1	1	1	1					
	Mean	St dev	Mean	St dev	Mean	St dev	Mean	St dev	Mean	St dev							
SiO2	75.23	1.05	75.01	0.75	75.17	0.41	75.11	1.00	75.42	0.91	75.43	75.2	75.39	71.93	74.28	74.34	75.38
TiO2	0.23	0.02	0.22	0.02	0.22	0.02	0.21	0.02	0.23	0.02	0.25	0.25	0.24	0.26	0.25	0.24	0.24
Al2O3	12.00	0.24	12.01	0.19	12.02	0.16	12.00	0.15	11.91	0.14	12.06	12.05	11.98	12.10	11.98	11.82	11.97
FeOT	3.28	1.34	3.23	0.92	3.13	0.18	3.29	1.02	3.31	0.91	3.66	3.73	3.69	3.65	3.72	3.68	3.66
MnO	0.11	0.04	0.11	0.04	0.11	0.04	0.11	0.03	0.11	0.02	0.10	0.10	0.10	0.10	0.10	0.10	0.10
MgO	0.10	0.02	0.1	0.02	0.01	0.02	0.09	0.02	0.10	0.02	0.23	0.25	0.23	0.27	0.17	0.22	0.22
CaO	1.66	0.16	1.68	0.13	1.66	0.1	1.69	0.11	1.66	0.14	1.73	1.71	1.74	1.72	1.74	1.73	1.71
Na2O	4.15	0.23	4.19	0.17	4.58	0.09	4.51	0.15	4.55	0.09	4.42	4.45	4.37	3.67	4.42	4.43	4.41
K2O	2.75	0.01	2.75	0.1	2.88	0.11	2.76	0.10	2.65	0.10	2.76	2.72	2.79	2.80	2.75	2.78	2.77
P2O5											0.02	0.02	0.02	0.02	0.02	0.02	0.02
Total	99.51	3.11	99.30	2.34	99.78	1.13	99.77	0.70	99.94	0.55	100.66	100.4 8	100.5 5	96.52	99.43	99.36	100.4 8

*Sample analyses reproduced from Tuffen & Castro (2009)

**Sample localities refer to the nomenclature given by Tuffen & Castro (2009); see their Figure 2. See Section 4a for XRF analytical methods.

Table 2 Experimental conditions summary

Sample number	Mean particle radius	Polydispersivity	Heating rate	Isothermal sample temperature*	Dwell time at isotherm	X-ray CT scan?
	$\langle R \rangle$	S	q			
	μm		$^{\circ}\text{C. min}^{-1}$	$^{\circ}\text{C}$	minutes	
M2207191334	13.2	0.58	10.7	no isotherm		
M2207181156	13.2	0.58	10.6	no isotherm		
M2207181415	13.2	0.58	10.4	no isotherm		
M2207181611	13.2	0.58	10.3	1200	10	
M2207181818	13.2	0.58	10.8	1200	15	Yes
M2207151707	17.1	0.61	10.6	no isotherm		
M2207161948	17.1	0.61	10.5	no isotherm		
M2207171824	17.1	0.61	10.7	no isotherm		
M2207121009	17.1	0.61	10.3	no isotherm		
M2207171041	17.1	0.61	10.8	1200	5	
M2207171309	17.1	0.61	10.5	1200	10	
M2207171520	17.1	0.61	10.3	1200	15	
M2207121409	17.1	0.61	10.4	1200	180	Yes
M2207191549	64.3	0.88	10.4	1200	20	Yes

*Note that where it appears that repeat measurements were performed (e.g. compare the conditions for M2207151707 with M2207161948), these were different experiments stopped at different times in order to collect microtextural information. Nevertheless, we document all experiments here in this table.

Table 3 Physical properties and regime calculations

Sample		"<32 microns"	"<63 microns"	">90 microns"
Mean particle radius	$\langle R \rangle$ μm	13.2	17.1	64.3
Variance of the particle distribution	$\langle R^2 \rangle$ μm^2	240.5	396.9	4461.6
Skewness of the particle distribution	$\langle R^3 \rangle$ μm^3	5433.9	11134.8	327901.8
Calculated mean pore size*	$\langle a \rangle$ μm	2.8	3.5	9.2
Calculated variance of pore sizes*	$\langle a^2 \rangle$ μm^2	15.9	24.4	137.0
Calculated skewness of pore sizes*	$\langle a^3 \rangle$ μm^3	139.2	256.2	2687.0
Peak temperature	T $^{\circ}\text{C}$	1200	1200	1200
Viscosity at peak temperature**	μ_e Pa.s	4.11×10^5	4.11×10^5	4.11×10^5
Surface tension	Γ N.m^{-1}	0.3	0.3	0.3
Initial H2O concentration	C_i wt. %	0.11	0.11	0.11
H2O diffusivity***	D_e m^2s^{-1}	2.09×10^{-12}	2.09×10^{-12}	2.09×10^{-12}
Capillary Peclet number [#]	Pc -	4.6	6.0	22.1

*Uncorrected pore sizes (see Wadsworth et al. 2017b)

** Calculated using Hess & Dingwell (1996) and at 1200 °C

*** Calculated using Zhang & Ni (2010) and at 1200 °C

[#]Calculated using $Pc = \Gamma\langle R \rangle / (\mu_e D_e)$ and not $Pc = \Gamma\langle R \rangle^2 / (\langle a \rangle \mu(T) D(T))$; see text for details

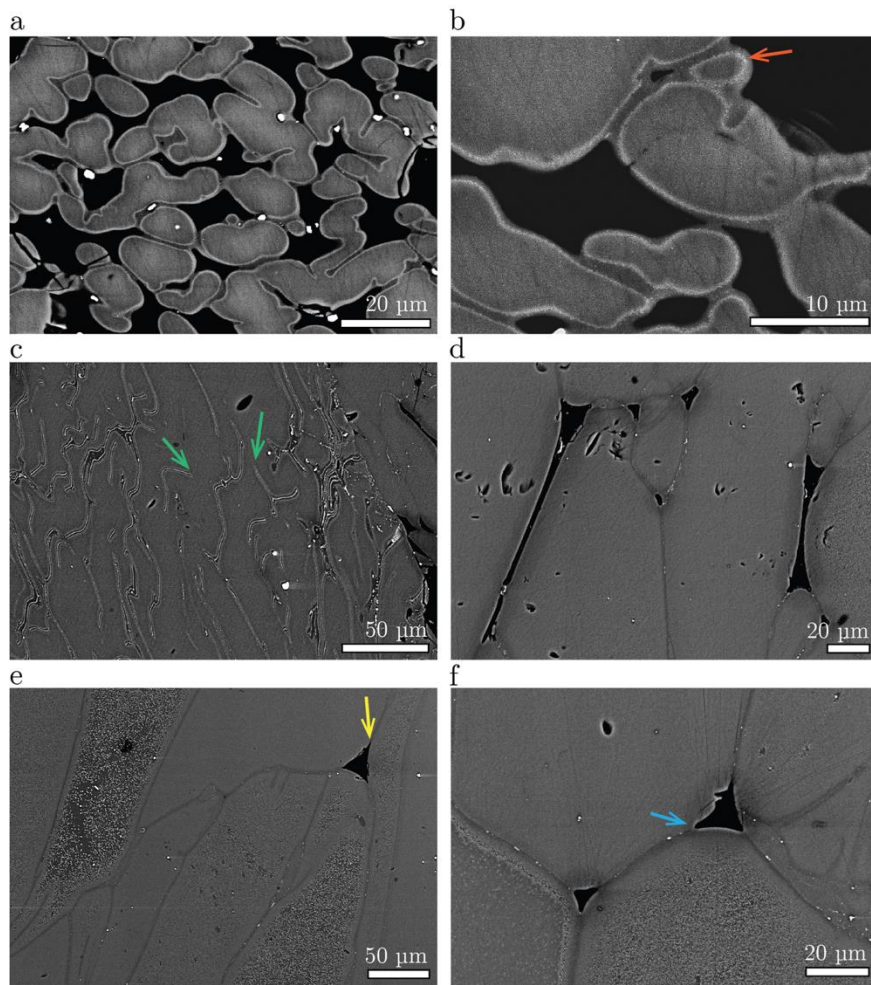


Figure 1. Examples of subaerial lava textures from Hrafninnuhryggur, Krafla (Iceland), captured in backscattered electron microscopy (BSE). (a) A BSE image of fracture-hosted (fracture edges not imaged) small, sub-rounded-to-rounded obsidian particles (grey) with interstitial porosity (black). Necks have formed between adjacent particles that share a contact point. (b) Detail of the particles in (a) showing the dark grey rim and a bright rim just inward from the edge (the bright rim is picked out by nanolite oxide crystals (see red arrow)). (c) Bright suture lines in dense obsidian, which can terminate abruptly in glass (see green arrows). (d) Elongate pores between obsidian clasts pick out clast-clast boundaries. (e) Pores with cusped triple corners (yellow arrow). In (e) there are also particles with evidence for internal nanolite oxide crystallization juxtaposed with particles that do not have that same evidence, showing that particles can experience different histories and then be sintered in contact with one another. (f) The same cusped triple-cornered pores as in (e) but with evidence for rounding of the pore tips. The pores in (d) and (f) show dark greyscale haloes (see blue arrow).

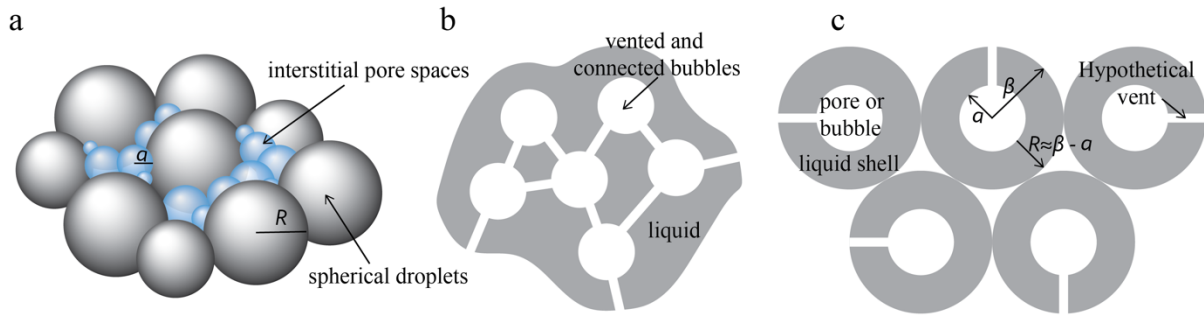


Figure 2. Schematic diagrams to show the developed of the VBM showing particles of radius R and pores of radius a . (a) The spherical approximation to the particles with hypothetically spherical pore spaces. (b) A 2D representation of the arrangement of ‘vented’ bubbles in a liquid. (c) Single cell unit used in the VBM. Sketch adapted from Wadsworth et al., (2016). From (a) to (b) to (c) represents steps of progressive abstraction of the natural system to render it amenable to analysis.

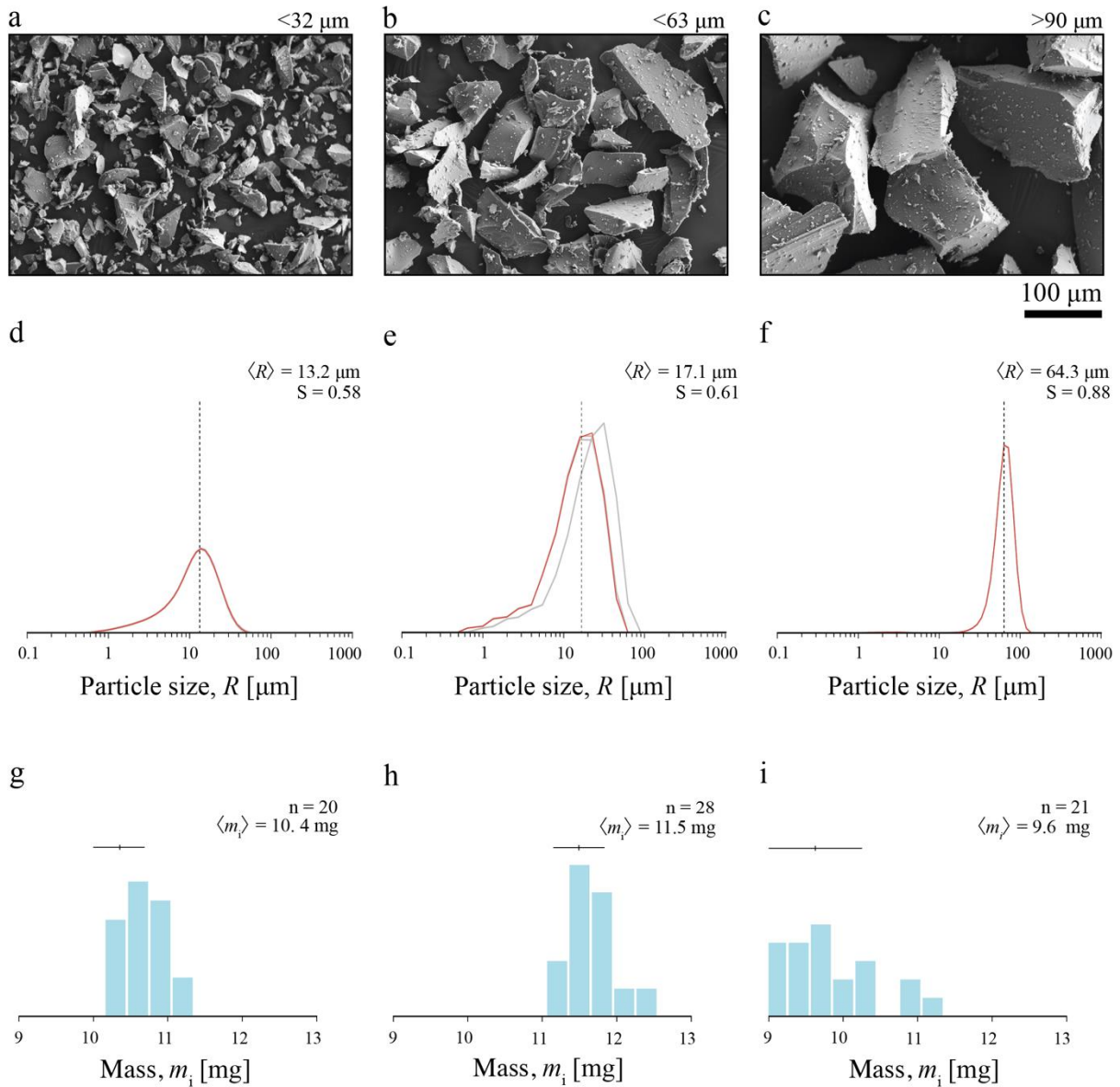


Figure 3. The results of sample characterization. (a-c) Scanning electron microscopy images of sieved obsidian powder to (a) $<32 \mu\text{m}$, (b) $32-63 \mu\text{m}$, and (c) $>90 \mu\text{m}$, using secondary emission mode. (d-f) Particle size distributions used here showing that (d) the $<32 \mu\text{m}$ has a mean $\langle R \rangle = 13.2 \mu\text{m}$, (e) the $32-63 \mu\text{m}$ has a mean $\langle R \rangle = 17.1 \mu\text{m}$, and (f) the $>90 \mu\text{m}$ has a mean $\langle R \rangle = 64.3 \mu\text{m}$. In (e) one of the ten repeat measurements is slightly different from the 9 others and is shifted to slightly higher particle sizes (grey curve), which can be taken to be a measure of the uncertainty on these measurements. We also report the polydispersity S (see text for calculation). (g-i) Histograms of the mass for small cylindrical samples made for use with the optical dilatometer. The mean sample mass $\langle m_i \rangle$ and the number of sample measurements for each histogram n are both reported.

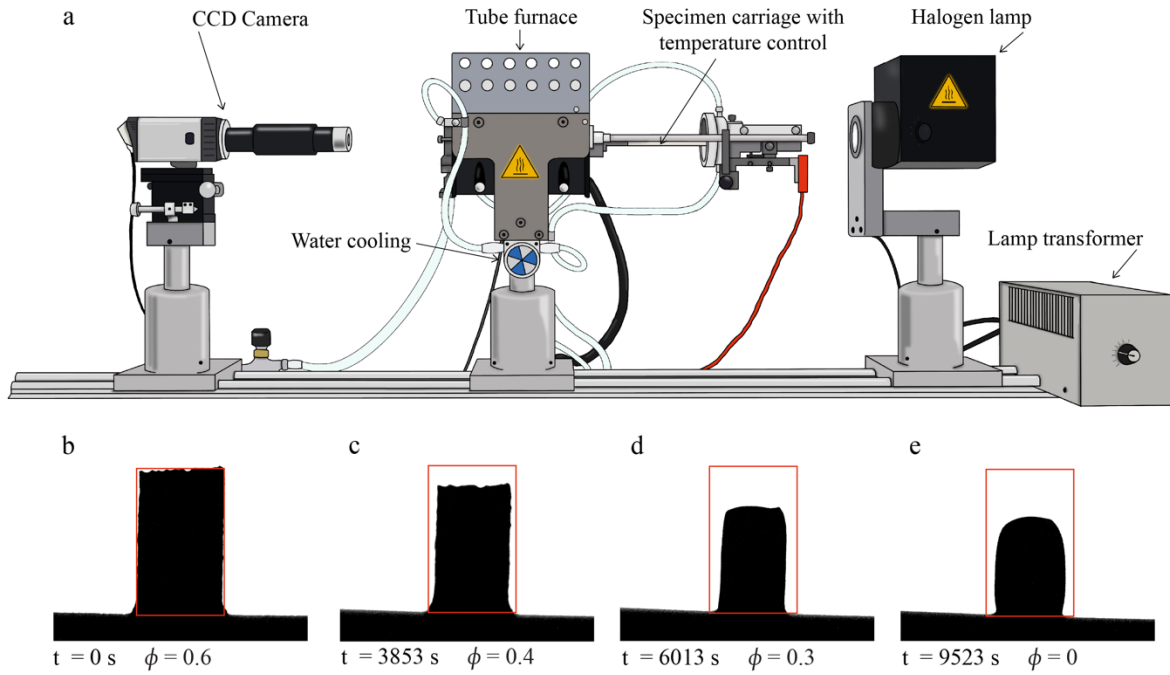


Figure 4. The experimental apparatus operation. (a) Schematic drawing of an optical dilatometer used here with the main components labelled. (b) Typical views of a sample cylinder as seen by the CCD camera with the principal output metrics indicated: sample height, sample width, base length of contact with the bottom plate, 2D area of the silhouette view, and sample perimeter length. In (b)-(e), the red rectangle has a base width of 3 mm.

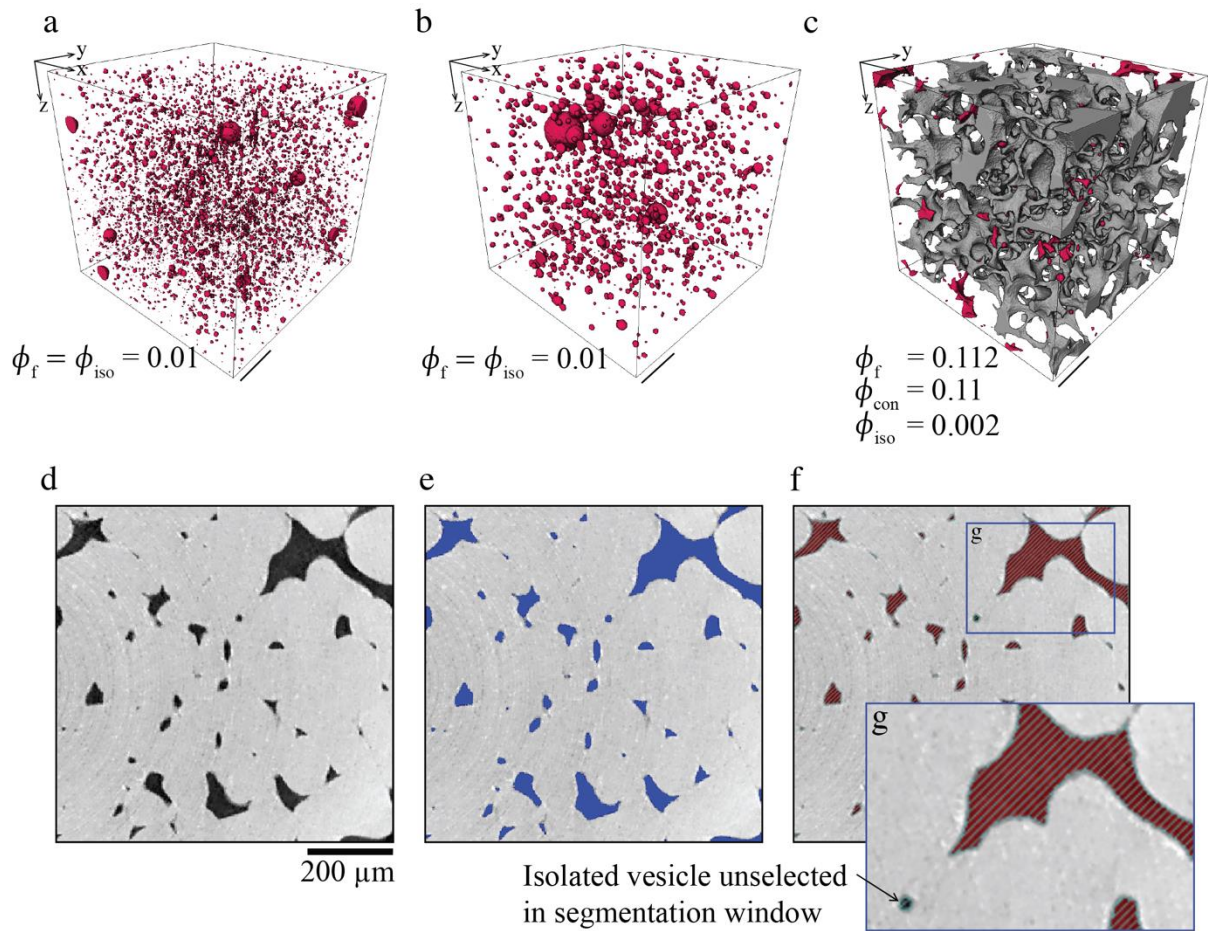


Figure 5. X-ray computed tomography results on post-experimental samples. (a-c) 3D renders of the pore phase (the solid glass phase is made invisible here) in three samples. In the case of (a) and (b), the samples are at volume equilibrium meaning that the sintering has completed. In the case of (c) the sintering has not completed and was halted part way through, showing the pre-completion convolute pore phase. In all cases, the final measured porosity ϕ_f value is labelled. In (a) and (b) the final porosity is equal to the isolated porosity (shaded red) such that $\phi_f = \phi_{iso}$, whereas in (c), the final porosity is distributed in connected ϕ_{con} (grey) and isolated ϕ_{iso} porosity (red). (d-g) Some pre-processing steps showing (d) a raw reconstructed 2D slice showing pores in black and glass particles in shades of grey. (e) A processed version of (d) where the pores are segmented in blue. (f) A connectivity selection showing how isolated pores are purposefully deselected. (g) A zoom-in of an area in (f) showing connected selection (red hashing) and isolated pores which are segmented as pore-space but not selected.

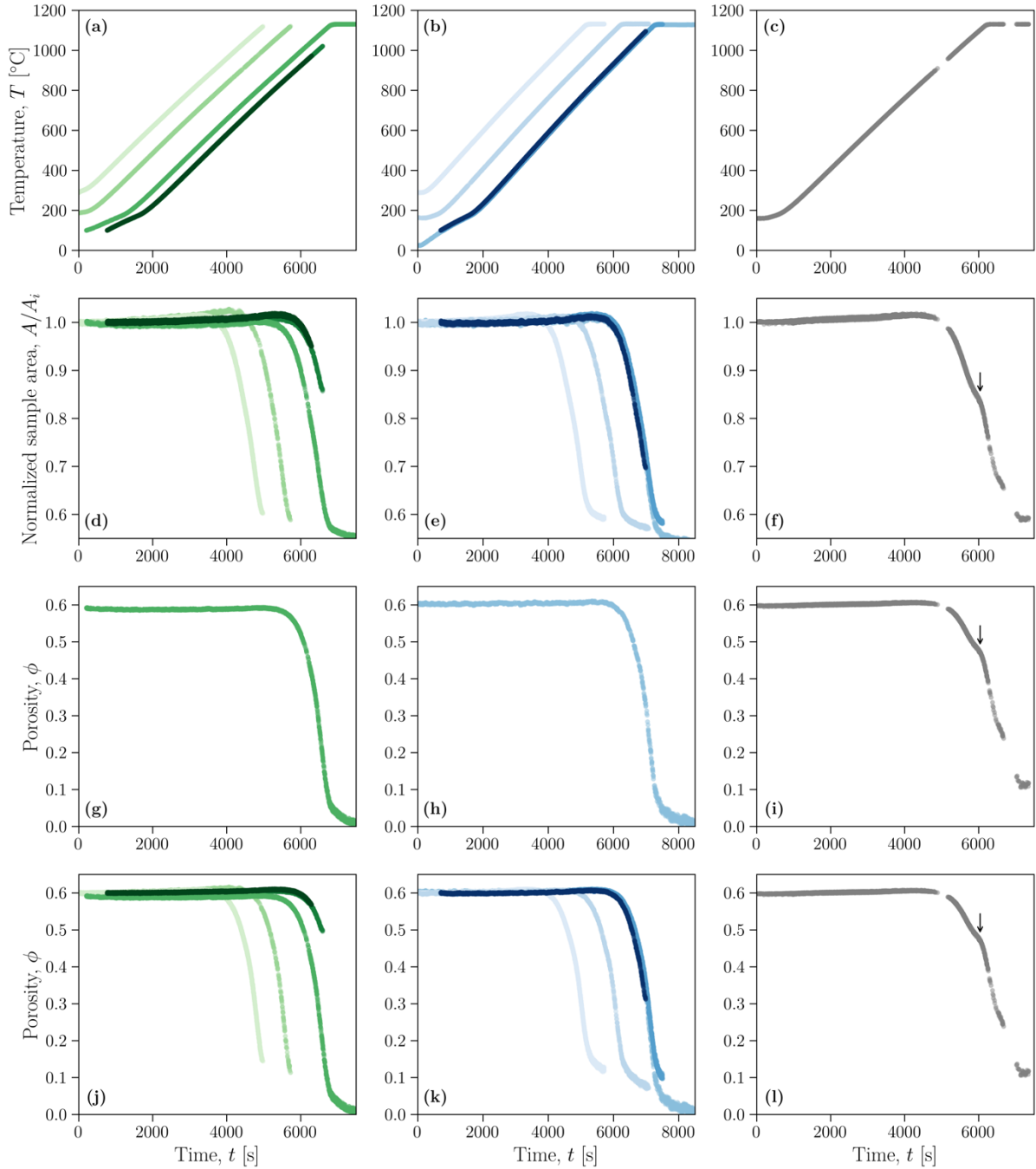


Figure 6. Raw data collected from the optical dilatometer and initial processing steps. (a-c) The temperature-time pathways that the samples of each grain size $\langle R \rangle$ was exposed to. Note that the offsets in time are due to differences in the start time at which the data collection was begun. (d-f) The raw data from the optical dilatometer showing the cross-sectional rectangular area $A(t)$ normalized by the initial area A_i (giving A/A_i) with time for each $\langle R \rangle$. (g-i) The post-processing raw porosity with time $\phi(t)$ calibrated using the X-ray computed tomography (Fig. 5). (j-l) All processed $\phi(t)$ data including the data reported in panels g, h and i, but where the initial value of $\phi_i = 0.6$ is used for all data for which X-ray computed tomography was not performed. Note that in this figure the first column (panels a, d, g, and j) refer to the particle population $\langle R \rangle = 13.2 \mu\text{m}$, the second column (panels b, e, h, and k) refer to the particle population $\langle R \rangle = 17.1 \mu\text{m}$, and the third column (panels c, f, i, and l) refer to the particle population $\langle R \rangle = 64.3 \mu\text{m}$. In panels (f), (i), and (l), the ‘kink’ in the data is indicated with an arrow; this kink is not present in the other datasets.

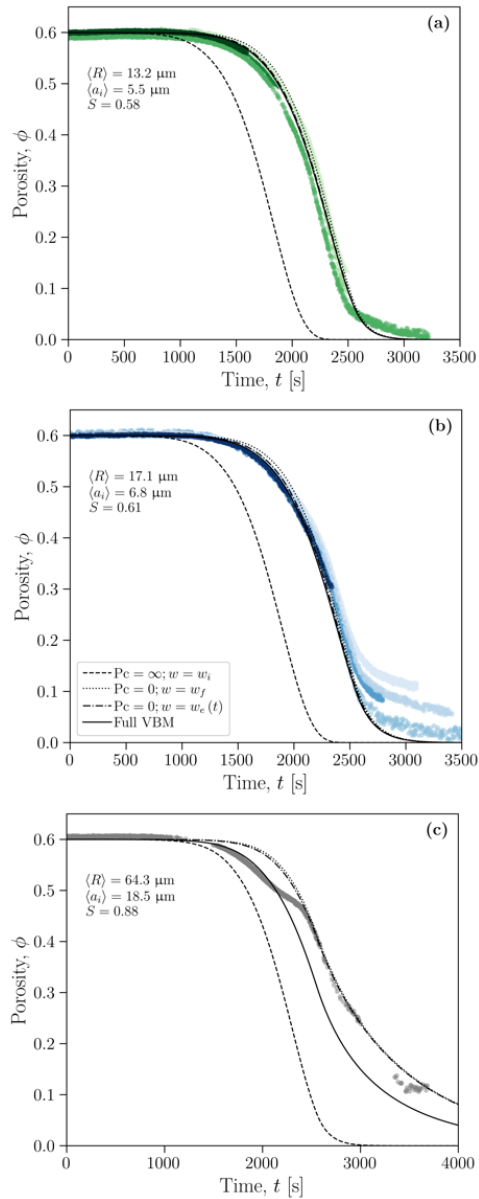


Figure 7. Comparing the datasets with the vented bubble model for sintering dynamics. The evolution of porosity $\phi(t)$ showing the decay toward a final equilibrium value ϕ_f as $t \rightarrow \infty$ for (a) $\langle R \rangle = 13.2 \mu\text{m}$, (b) $\langle R \rangle = 17.1 \mu\text{m}$, and (c) $\langle R \rangle = 64.3 \mu\text{m}$ where $t = t_{\text{exp}} - t_{\text{ref}}$ with t_{ref} equal to the time when the glass transition is crossed (see text for details). Also shown are model predictions assuming (1) the full VBM model with diffusive degassing of H_2O accounted for (Wadsworth et al., 2019), (2) the solution assuming that no degassing occurs (i.e. $\text{Pc} = \infty$ and $w = w_i$ for all t), (3) the solution when degassing is more rapid than sintering (i.e. $\text{Pc} = 0$ and $w = w_e$ for all t), or (4) the solution when degassing is more rapid than sintering and a reference ‘final’ H_2O concentration is assumed (i.e. $\text{Pc} = 0$ and $w = w_f$ for all t). Here we assume that w_f is the value of w_e at $1200 \text{ }^\circ\text{C}$, giving $w_f = 0.036 \text{ wt.}\%$. The difference between (3) and (4) is simply in the way viscosity μ is calculated for each temperature, and therefore for each time.

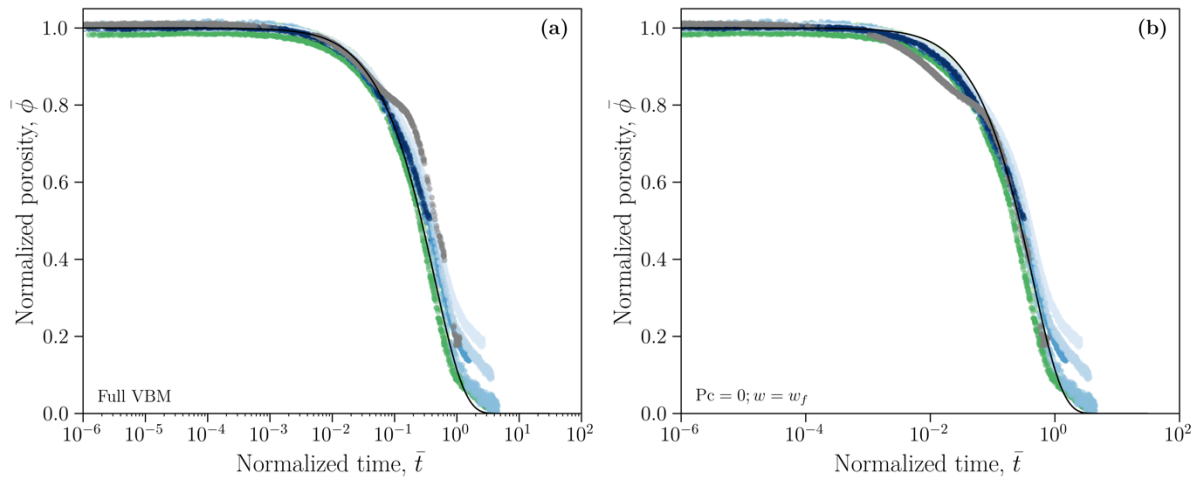


Figure 8. The universal capillary sintering curves. Here we have converted $\phi(t)$ to $\bar{\phi}(\bar{t})$ and have used \bar{t} , which is computed either using (a) the full VBM in Eq. 3, or (b) the $Pc = 0$ and $w = w_f$ model in Eq. 3. The similarity between these two approaches reflects the similar effectiveness of these models found in Fig. 7.

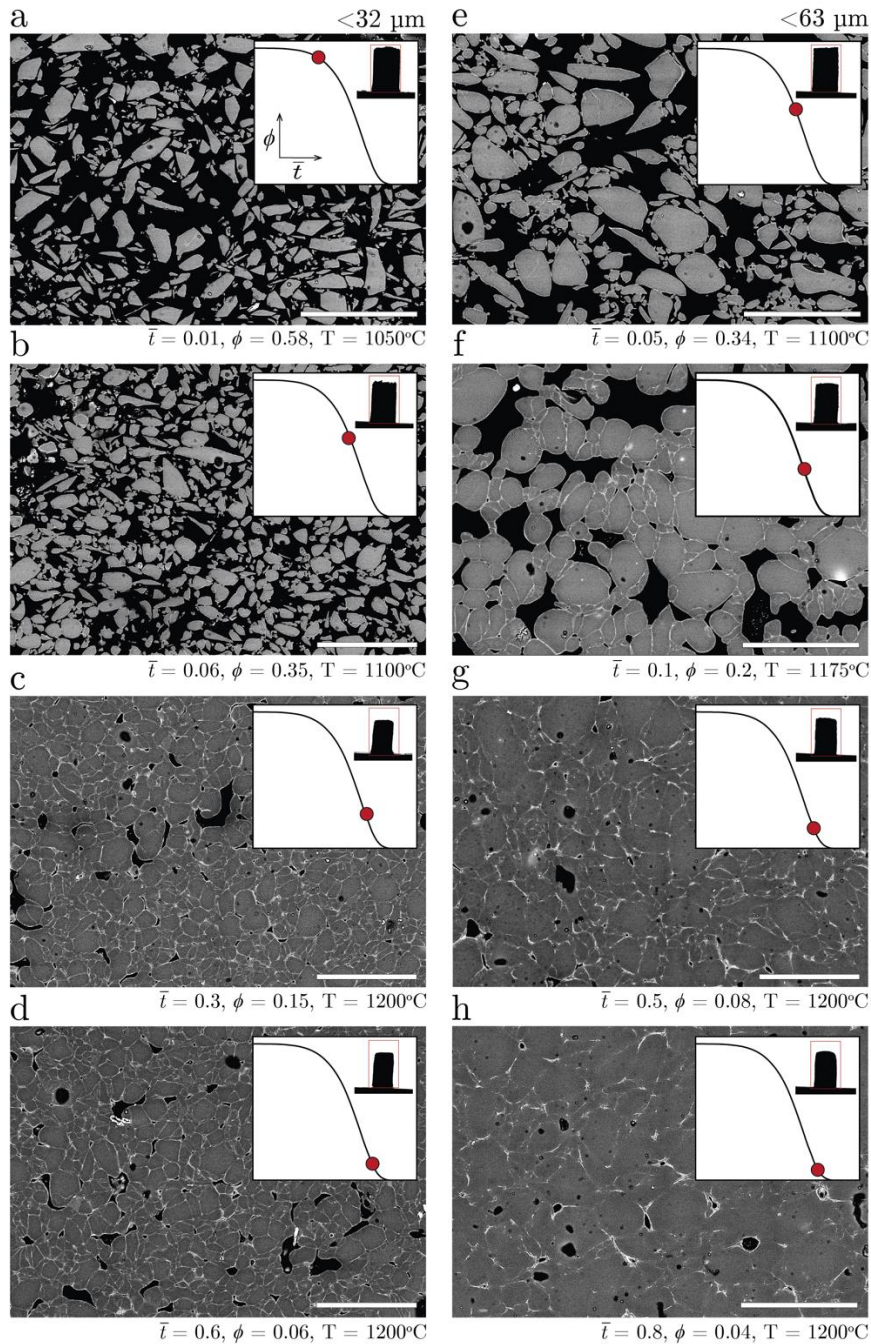


Figure 9. The evolution of the microtexture during sintering of obsidian particles. The evolution of microtexture obtained via scanning electron microscopy on resin-mounts for (a-d) the $<R> = 13.2 \mu\text{m}$ sieve size ($\langle R \rangle = 13.2 \mu\text{m}$), and (e-h) the $<R> = 17.1 \mu\text{m}$ sieve size ($\langle R \rangle = 17.1 \mu\text{m}$). In all cases, the maximum temperature reached, T , is given, as well as the observed ϕ (calculated from the 2D area; **Fig. 6**) and the calculated dimensionless time \bar{t} (where $\bar{t} = 1$ would be an approximate metric for complete sintering). In general, these images show an evolution from particle geometries with interstitial pore space, e.g. (a) and (e), to pores with interstitial glassy groundmass, e.g. (d) and (h), which is typical of sintering. All scale bars are $100 \mu\text{m}$. *Insets*: a schematic of the $\phi(\bar{t})$ model curve showing where along the dimensionless sintering pathway each sample was quenched (red dot), and the 2D sample silhouette relative to the initial sample geometry given by the red box (i.e. the smaller the silhouette, the more progressed sintering densification is). Note that samples (c), (d), (g), and (h) all are marked $T = 1200^\circ\text{C}$, but whereas (c) and (g) were quenched when 1200°C was reached, (d) and (h) were held at 1200°C for 10 minutes before being quenched.

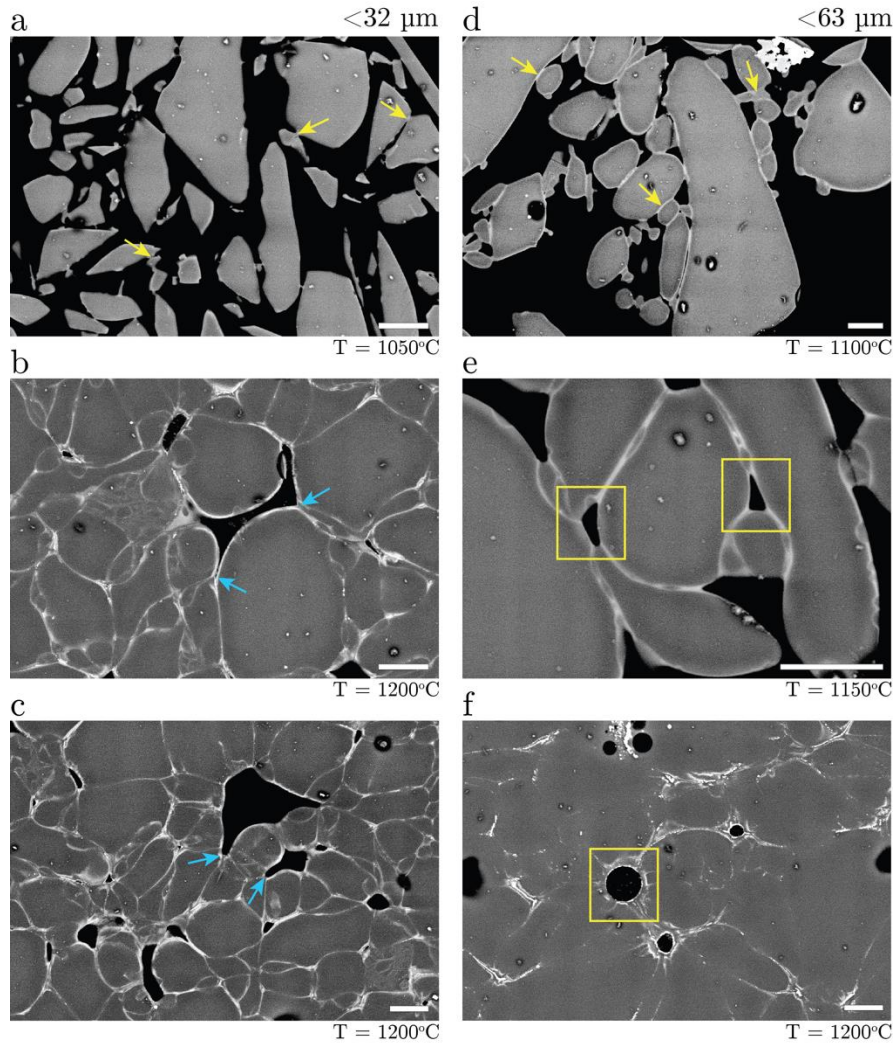


Figure 10. Details associated with microstructure changes during sintering. Scanning electron microscope images are for (a-c) the $< 32 \mu\text{m}$ sieve size ($\langle R \rangle = 13.2 \mu\text{m}$), and (d-f) the $< 63 \mu\text{m}$ sieve size ($\langle R \rangle = 17.1 \mu\text{m}$). In all cases the peak temperature reached is labelled. (a) Sub-angular particles have developed narrow necks (yellow arrows) at the incipient sintering stage. (b) Particles have rounded and sintering has progressed at the expense of pore space; the remnant pore space forms cusped geometries with pointed tips (blue arrows). (c) When held at peak temperature for some time, the pore space pointed tips round off (blue arrows). (d) Particles have transitioned from angular to sub-rounded with broad necks (yellow arrows). (e) Sub-rounded vesicles become progressively more isolated between sintering particles (yellow boxes). (f) Once isolated, vesicles round toward spherical (yellow box). All scale bars are $10 \mu\text{m}$. Minor oxide crystallization is shown by bright rims in (b-f), reproducing the nanolite rims shown in **Fig. 1**.

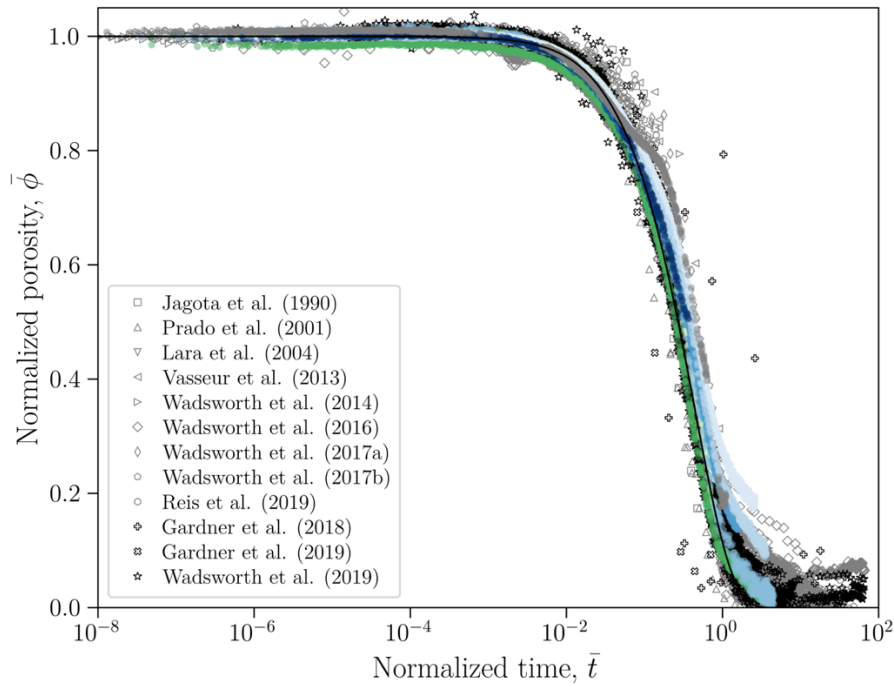


Figure 11. The universal capillary sintering curve (as shown in Fig. 8a) compared with all available sintering data. Here, our data (see Figure 7 for colour and symbol use) are compared with available capillary sintering data including sintering of synthetic glass particles (Jagota et al., 1990; Prado et al., 2001; Lara et al., 2004; Vasseur et al., 2013; Wadsworth et al., 2014; Vasseur et al., 2016; Wadsworth et al., 2016, 2017a, 2017b; Reis et al., 2018), sintering of Hrafninnuhryggur obsidian (Wadsworth et al., 2019, 2021), and sintering of obsidian from the Mono Craters (Gardner et al., 2018, 2019). The Mono Craters experiments (Gardner et al., 2018, 2019) were performed at elevated gas pressures allowing for elevated H_2O concentrations relative to the ambient pressure experiments in this study. These datasets include tests of grain polydispersivity, grain angularity, heating rates, H_2O gas pressure (which affects H_2O solubility), and temperature for grains of diverse composition, showing that the vented bubble model (VBM) is an effective universal sintering model across all of these parameters. The VBM is the solid black curve. The colored symbols are the data from this study (see Fig. 6 for the color code for each experiment).

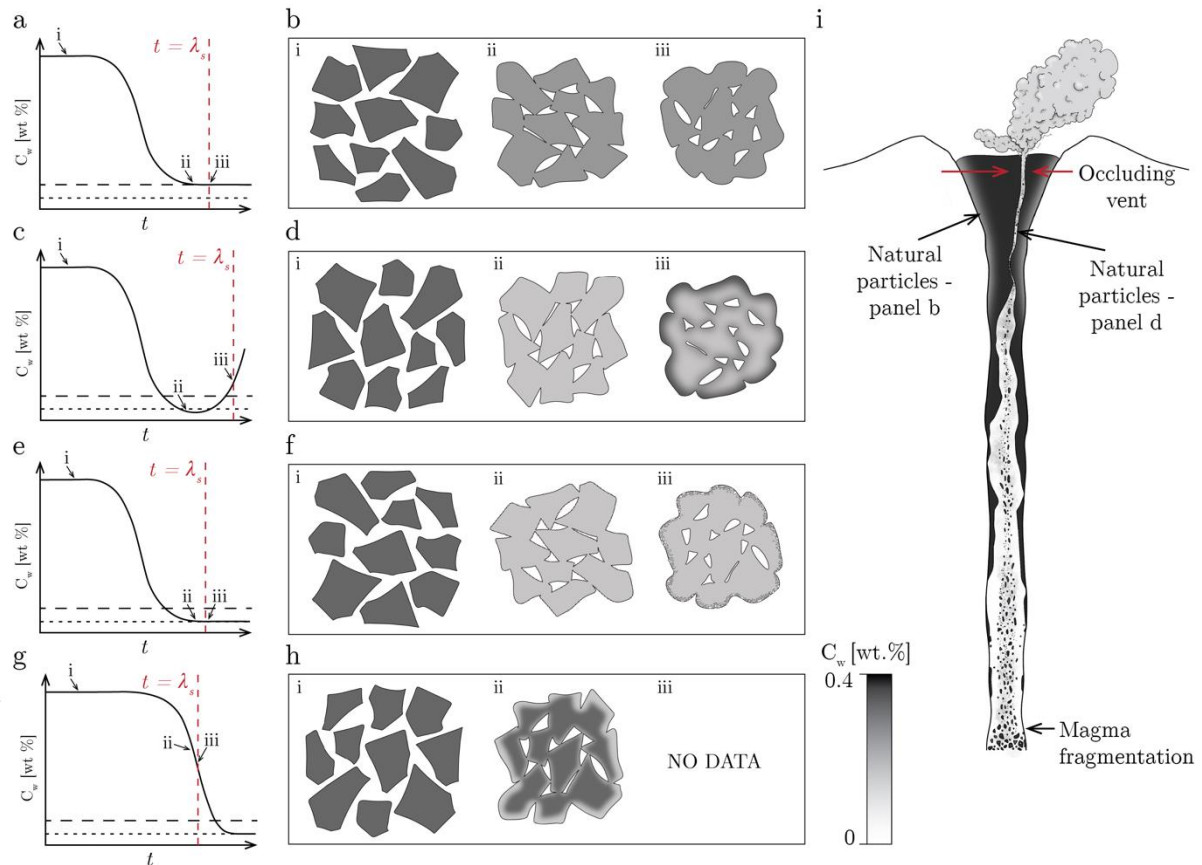


Figure 12. Schematic interpretations of the sintering dynamics discussed here. (a) The evolution of C_w with time t for ‘normal’ low C_i obsidian such as the Hrafninnuhryggur obsidian. (b) The schematic microstructure of sintering during C_w -loss associated with (a), where (i), (ii), and (iii) show time steps involving particle diffusive degassing (see change in greyscale value from (i) to (ii)), and sintering (see the formation of inter-particle necks from (i) to (ii) and the bulk occlusion of pore space from (ii) to (iii)). The interpretation of greyscale variations in SEM samples is from Humphreys et al., (2008). The interpretation is that (a) & (b) explain the bulk of the dense obsidian and rhyolite lava production at Hrafninnuhryggur. (c) The schematic view of the loss of H_2O followed by ‘regassing’ as conduit occlusion causes the increase in water vapor pressure in the conduit (see Foster et al 2024); (d) shows the associated textural and greyscale evolution where we note the late-stage rehydration of the particle rinds (see also Figs 1a & 1b). (e) & (g) show the loss of H_2O from samples in the laboratory where the final equilibrium H_2O is lower, due to the low partial pressure of H_2O in laboratory furnaces (note the difference between (e) and (g) is that (e) refers to the $Pc \ll 1$ case (i.e. the $< 32 \mu m$ and $< 63 \mu m$ samples herein; Table 3), whereas (g) refers to the $Pc > 1$ case (i.e. the $> 90 \mu m$ sample herein; Table 3). (f) & (h) refer to the microtextural evolutions found here that relate to (e) and (g), respectively. Note that in (f), we show that nanolites formed on the exterior boundaries of the degassing and sintering particles. (i) An eruption snapshot adapted from Wadsworth et al. (2020) showing where sintering is occurring in the volcanic conduit during ongoing explosive or hybrid activity.

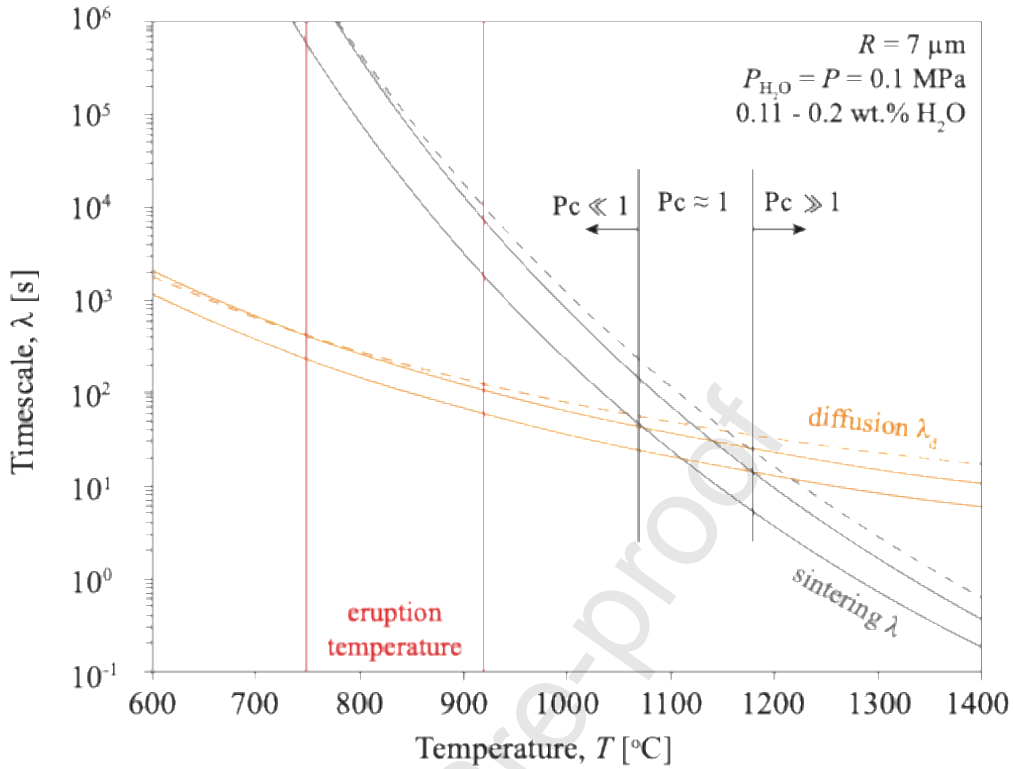


Figure 13. A quantitative sintering timescale map used to apply the sintering theory validated herein to the Hrafninnuhryggur eruption for $R \approx 7 \mu\text{m}$ (Fig. 1a). The orange curves represent the diffusion timescale $\lambda_D = R^2/D$ and the black curves represent the sintering timescale $\lambda = \mu R/\Gamma$. In both cases, the H_2O concentration affects the solution (with C_w impacting D in λ_D via Eq. 7 and μ in λ via Eq. 4). Therefore the solid curves represent the solutions to λ_D and λ with a constant C_w (0.1 wt.% and 0.2 wt.% for the lower and upper solid curves, respectively) capturing the range measured in the subaerial obsidian lavas (Tuffen and Castro, 2009). The dashed curves represent the solution using the temperature-dependent solubility of H_2O given by Eq. 6 and with the assumption of 1 bar pressure. The vertical red curves represent a lower and an upper estimate for the eruption temperatures (Zierenberg et al., 2013; Foster et al., 2024). At these temperatures, it is clear that the diffusion timescales are shorter (lower values) than the sintering timescales and therefore degassing or regassing can be extremely effective before sintering occurs to close-up the pore spaces and change the diffusion process (cf Vasseur et al., 2023). The associated regime transition is marked using the dimensionless group Pc (see Eq. 5).

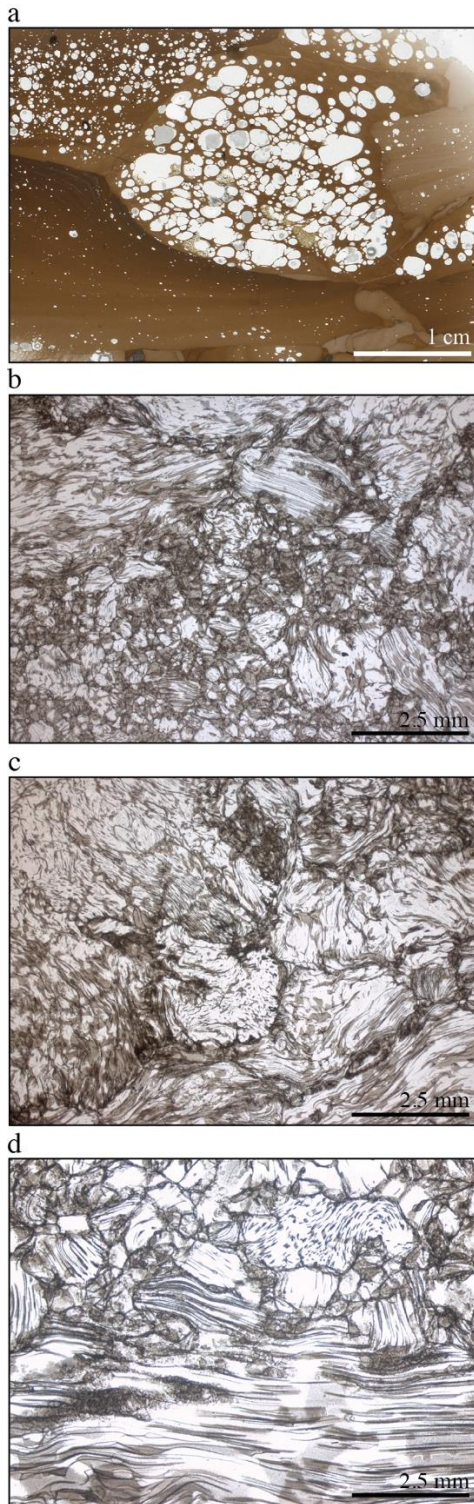


Figure 14. Textural evidence for vesicularity and its role in sintering dynamics at Hrafninnuhryggur. (a) Evidence for secondary vesiculation including the clast-marginal vesicle-free region (termed the ‘skin’), which suggests there was diffusive outgassing during vesiculation and prior to quenching (Yoshimura and Nakamura, 2008; von Aulock et al., 2017; Weaver et al., 2022, 2023). The sample shown in (a) is from the AO site given in Tuffen & Castro (2009). (b)-(d) Evidence for ash and lapilli-sized pumice clasts involved in sintering, where there is direct evidence that the

pumice clasts have variable collapsed to some extent. The samples shown in panels (b), (c), and (d) are from the S site given in Tuffen & Castro (2009).

Journal Pre-proof

Author statement

Annabelle Foster: Conceptualization, methodology, formal analysis, investigation, writing original-draft, writing review & editing. **Fabian Wadsworth:** Conceptualization, methodology, writing original-draft, writing review & editing. **Jeremie Vasseur:** Formal analysis, visualization, writing review & editing. **Madeleine Humphreys:** Writing review & editing. **Hugh Tuffen:** methodology, writing review & editing. **Donald Dingwell:** Writing review & editing, funding acquisition. **Katherine Dobson:** Methodology, formal analysis, writing review & editing.

Journal Pre-proof

Declaration of interests

The authors declare that they have no known competing financial interests or personal relationships that could have appeared to influence the work reported in this paper.

The authors declare the following financial interests/personal relationships which may be considered as potential competing interests:

Journal Pre-proof

Highlights

- Sintering dynamics of viscous silicic particles can be influenced by diffusive degassing of volatile H₂O.
- At eruptive temperatures, very fine-grained viscous sintering occurs in H₂O equilibrium.
- Continuous sintering data reveal that particles larger than c. 50 microns will degas during sintering.
Viscous sintering of fine ash-sized particles can replicate textures in obsidian-dominated lavas.

Journal Pre-proof

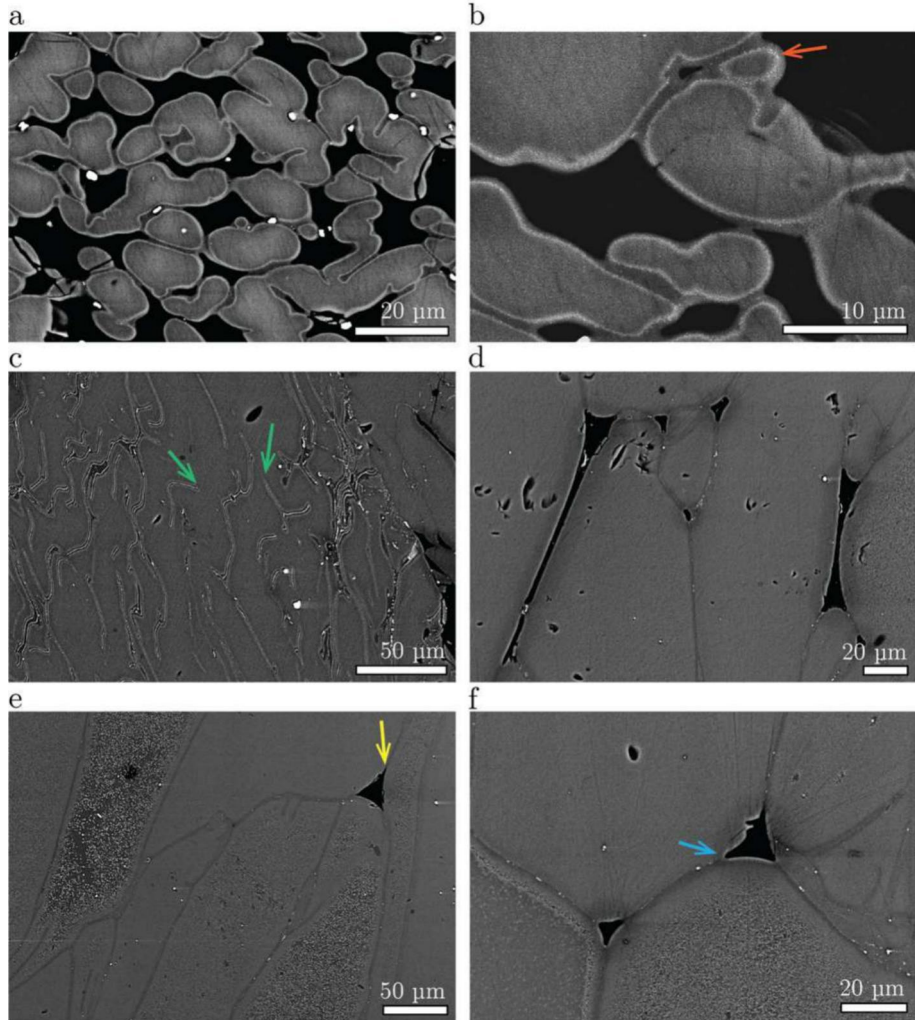
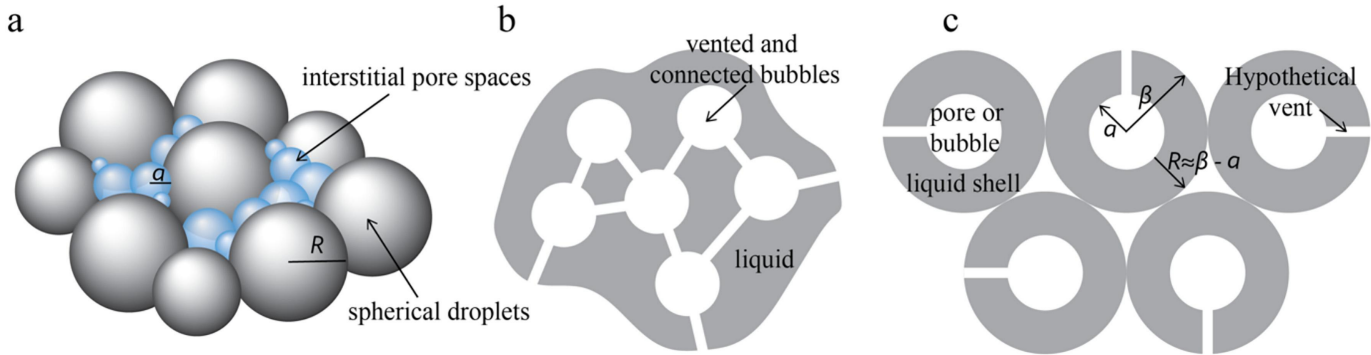


Figure 1



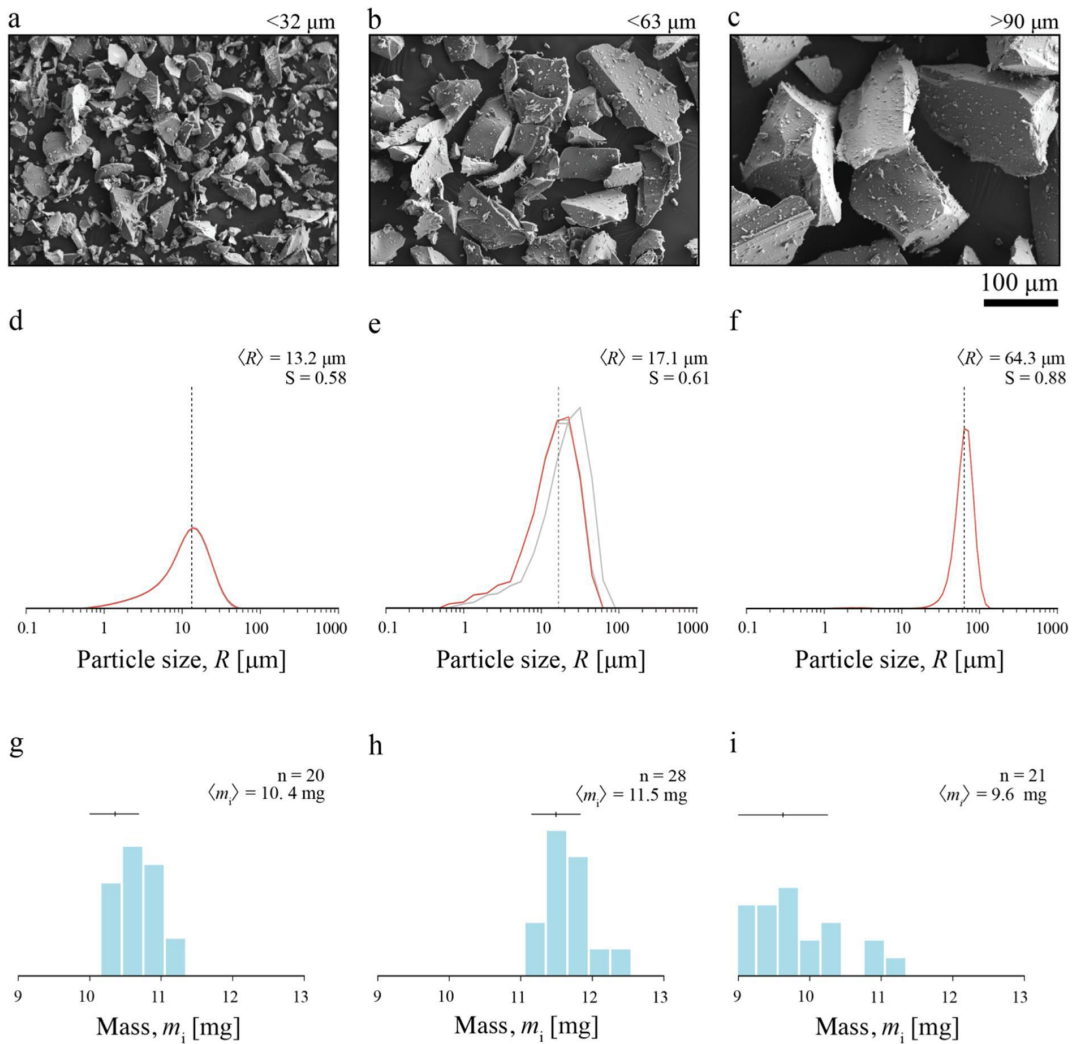


Figure 3

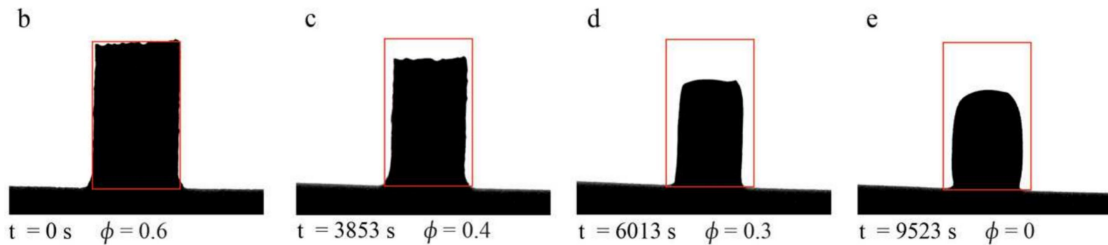
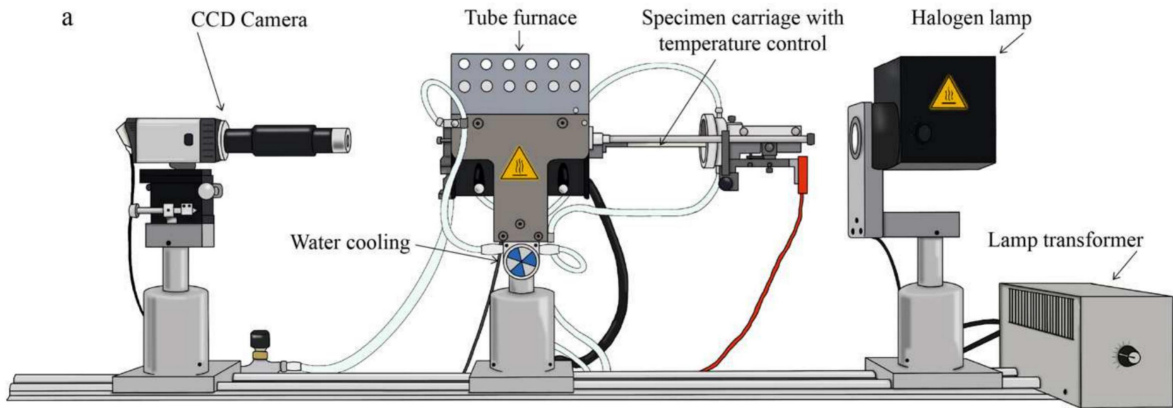


Figure 4

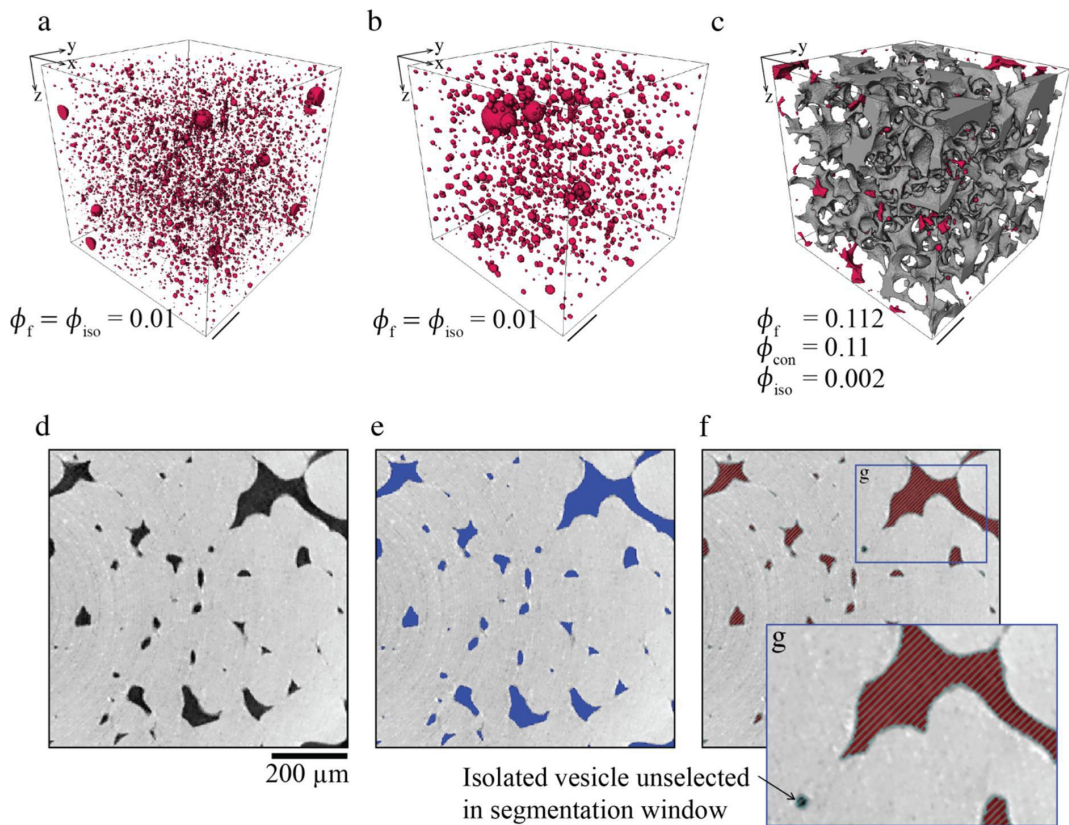


Figure 5

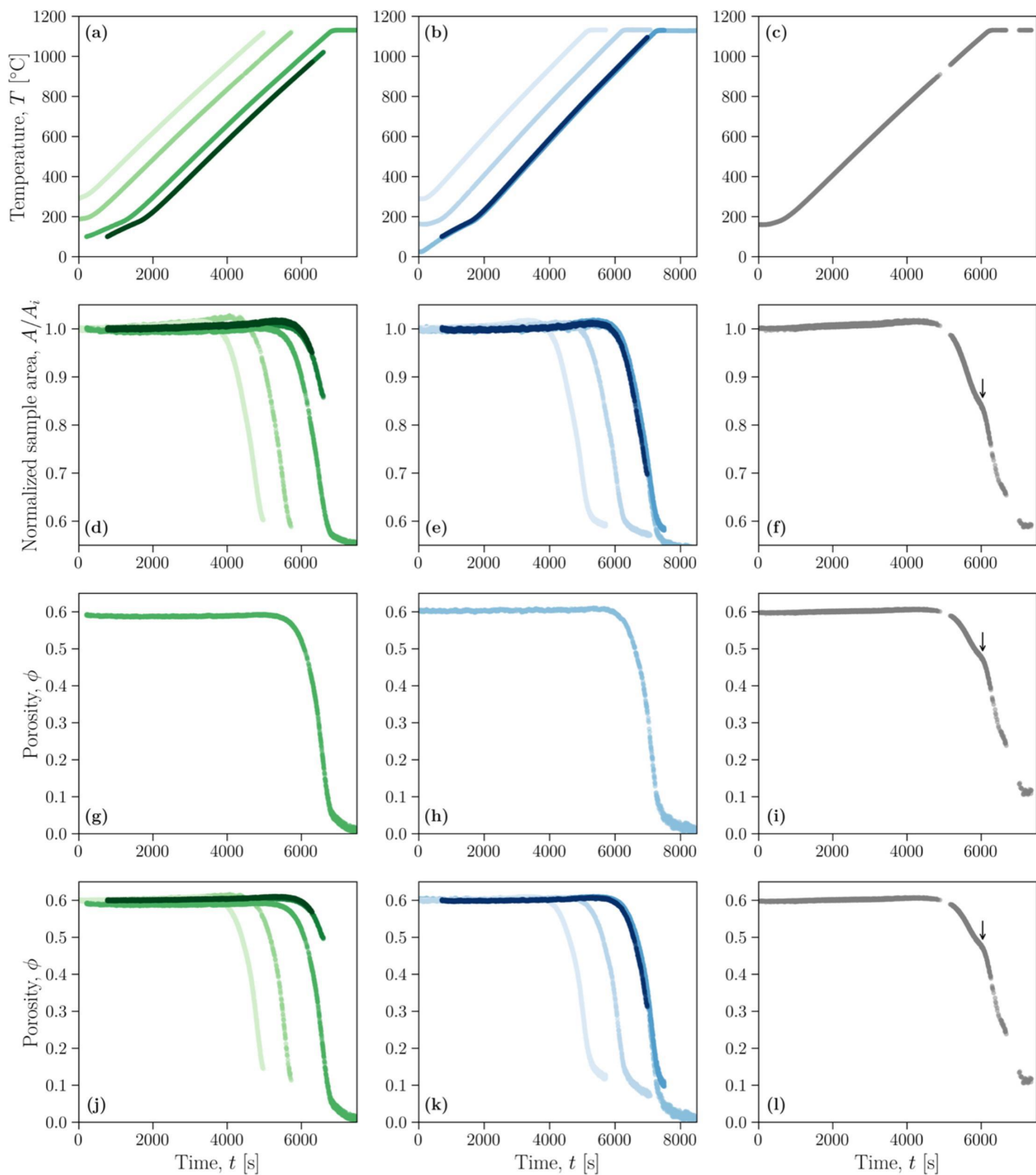


Figure 6

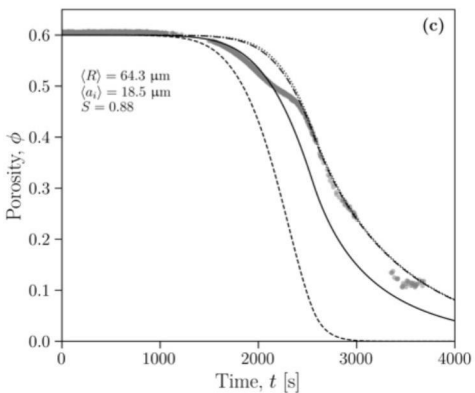
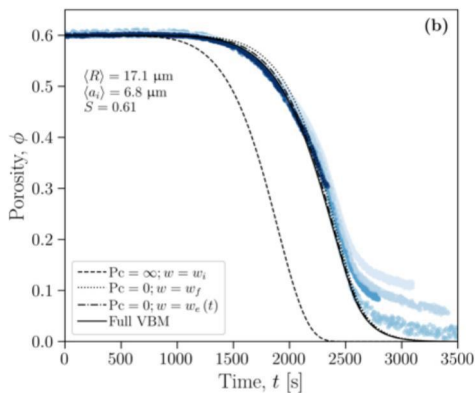
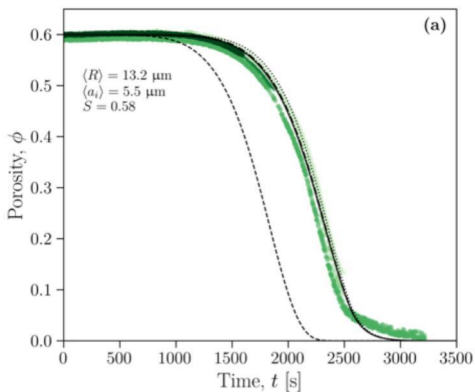


Figure 7

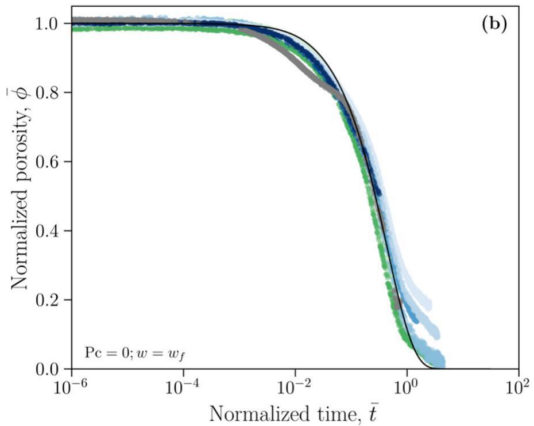
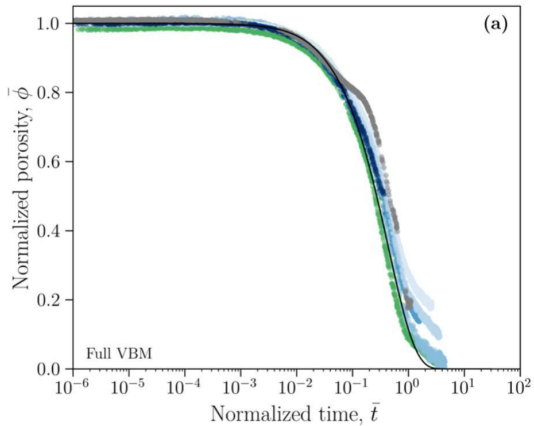


Figure 8

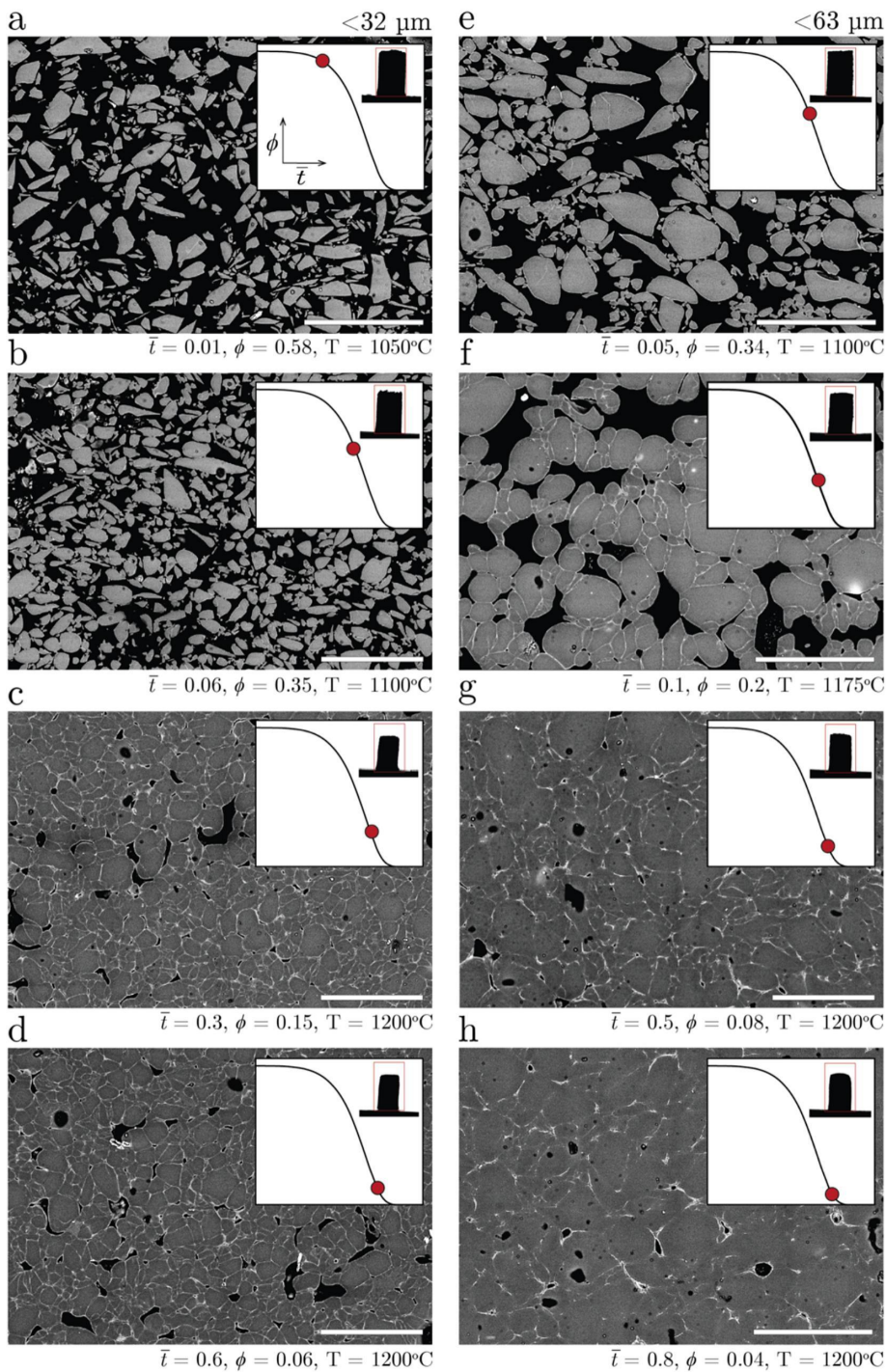


Figure 9

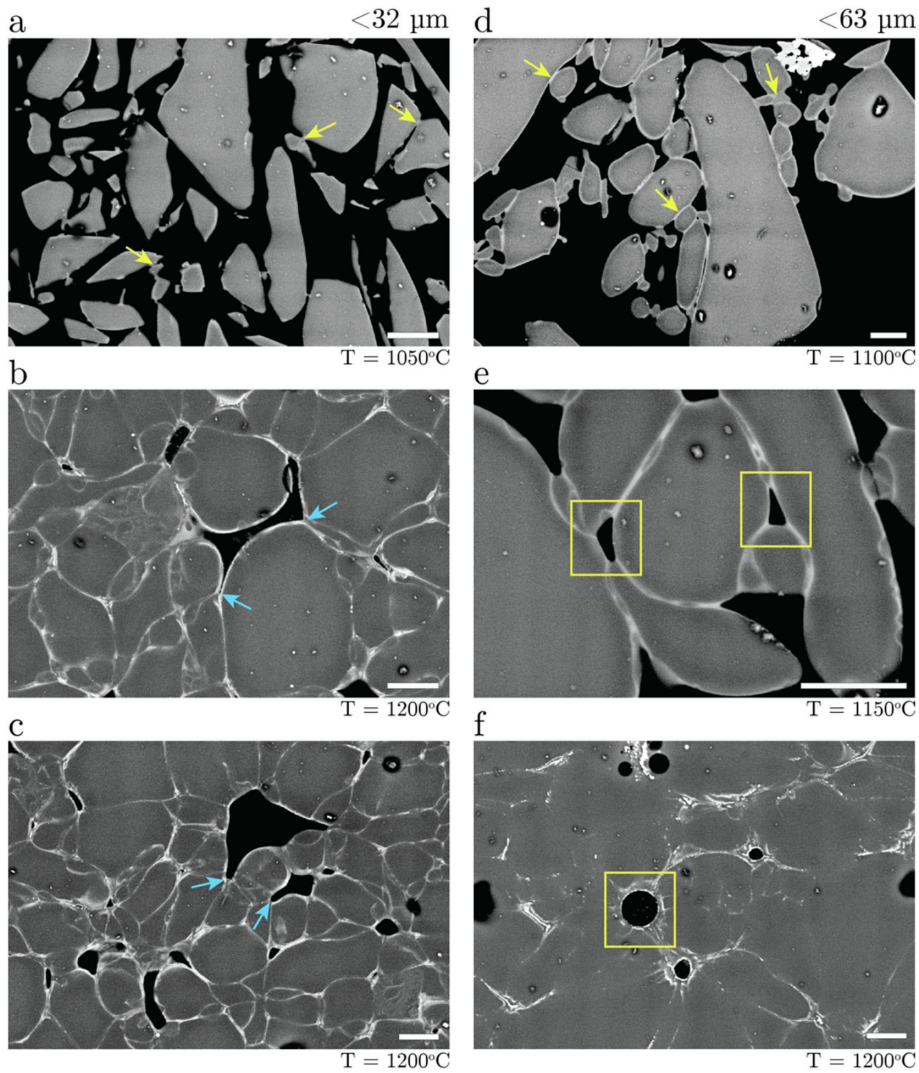


Figure 10

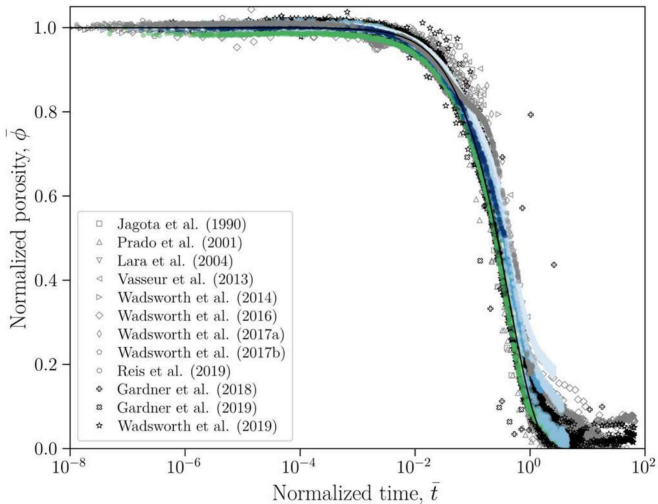


Figure 11

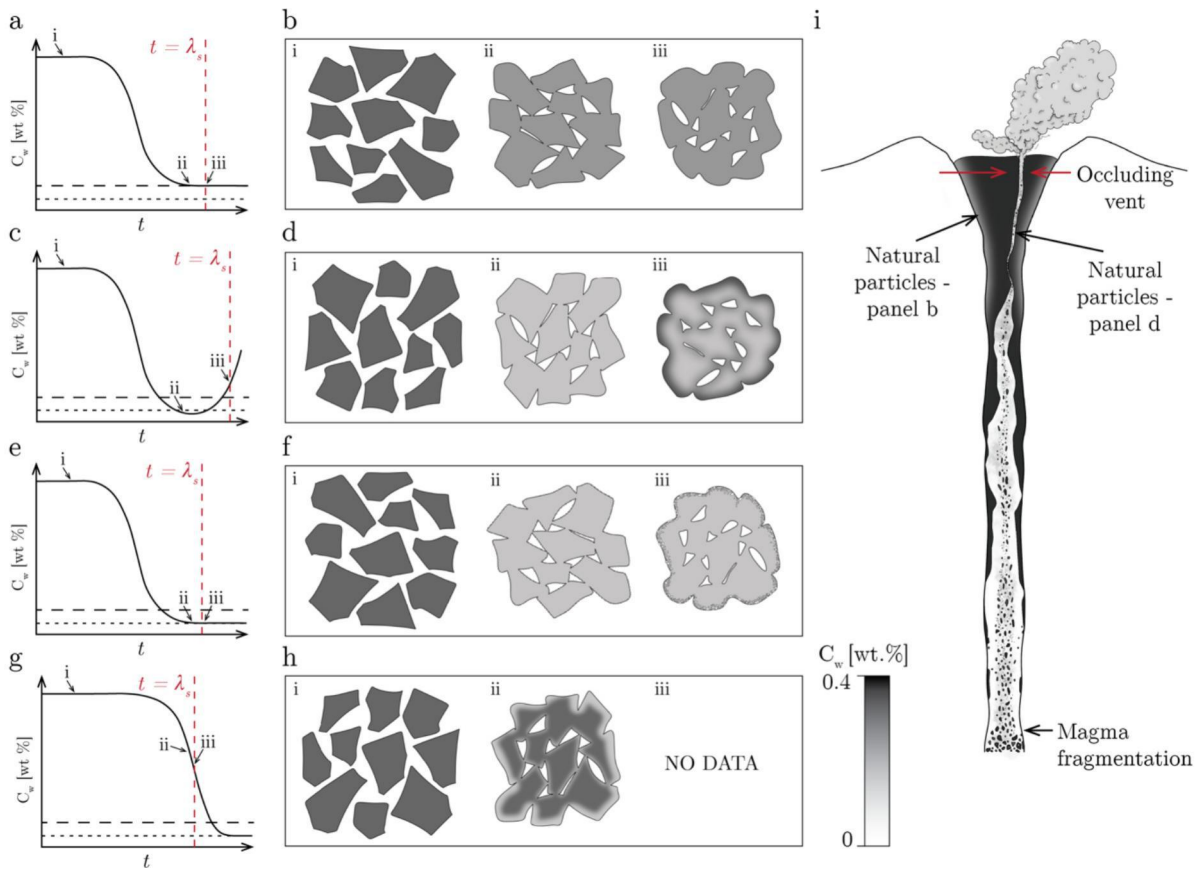


Figure 12

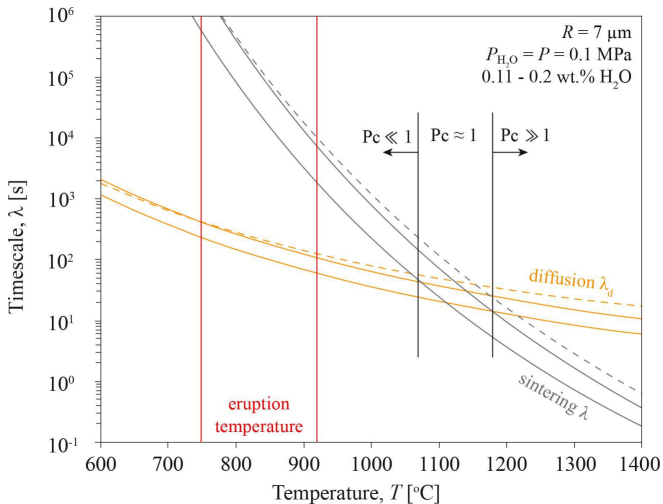


Figure 13

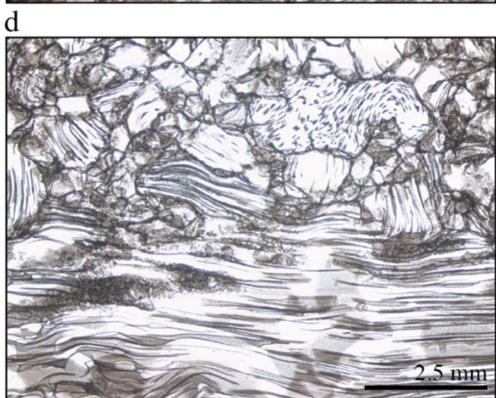
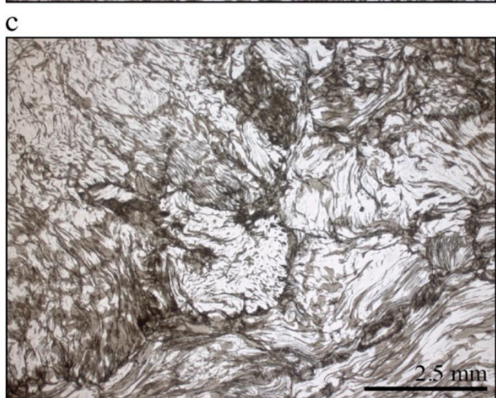
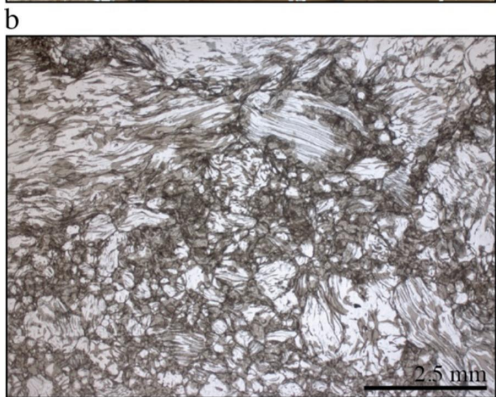
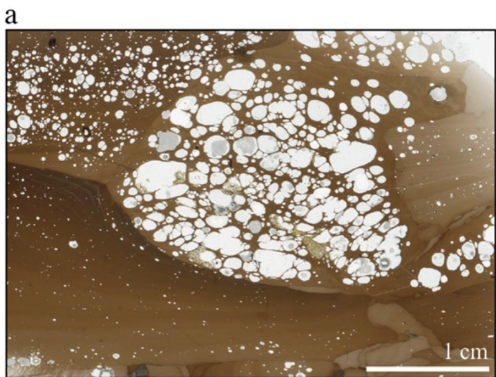


Figure 14